DISSERTATION

REAL-TIME 2D AND 3D ELECTRICAL IMPEDANCE TOMOGRAPHY AND APPLICATIONS

Submitted by

Nilton Barbosa da Rosa Junior

School of Biomedical Engineering

In partial fulfillment of the requirements

For the Degree of Doctor of Philosophy

Colorado State University

Fort Collins, Colorado

Spring 2025

Doctoral Committee:

Advisor: Jennifer Mueller

Jesse Wilson
Pedro Boscan
Steve Simske

ABSTRACT

REAL-TIME 2D AND 3D ELECTRICAL IMPEDANCE TOMOGRAPHY AND APPLICATIONS

Electrical impedance tomography (EIT) is a non-invasive and non-ionizing real-time bedside imaging modality for functional pulmonary imaging. The EIT systems produce images of impedance distributions within the body by injecting electric currents and measuring voltages on electrodes applied to the skin. Regional EIT images of ventilation and pulsatile perfusion have the potential to provide information about the lung structure and function of patients with pulmonary diseases.

The Adaptive Current Tomograph 5 (ACT5) system is a novel EIT system that can provide 2D and 3D EIT measurements from ventilation and pulsatile perfusion sequences, and simultaneously monitor heart activity by measuring and recording the electrocardiogram (ECG) at all active electrodes while measuring EIT data. This dissertation describes all the components present in the software side of the ACT5 system, which include 2D and 3D EIT reconstruction algorithms, digital filters, a graphical user interface, and the EIT reconstructions on healthy controls and patients with cardiac and pulmonary diseases.

To evaluate the potential of EIT on reconstructing pulmonary ventilation and pulsatile perfusion images, EIT reconstructions were performed from data collected on premature babies and patients with cystic fibrosis, acute respiratory distress syndrome, pulmonary vein stenosis, and healthy control subjects. The EIT reconstructions from patients show different ventilation and perfusion distributions when compared to healthy subjects. Lung regions affected by cardiopulmonary diseases can also be identified in the EIT reconstructions.

ACKNOWLEDGEMENTS

I would like to thank God, my family members, my girlfriend, and my friends for all the support over the years. I want to thank my advisor, Professor Jennifer Mueller, for all the guidance and support. It would not be possible to achieve my research goals without her exceptional expertise. I would like to thank the team at University at Albany, especially Professor Gary Saulnier and Dr. Omid Rajabi Shishvan for all the help and collaboration related to the development of the ACT5 system. I want to thank the team at Rensselaer Polytechnic Institute, especially Dr. Isaacson and Dr. Newell, for all the insights and knowledge provided. I would like to thank all the team members at the University of Colorado Anschutz Medical Campus and Children's Hospital Colorado, especially Allison Keck, Katie Enzer, and Catalina Vargas Acevedo for all the help during data collection. I want to thank Dr. Jesse Wilson, Dr. Pedro Boscan, and Dr. Steve Simske for accepting to be part of my doctoral committee and for always being willing to help.

TABLE OF CONTENTS

LIST OF TABLES

LIST OF FIGURES

Chapter 1

Introduction

1.1 Electrical Impedance Tomography (EIT)

Electrical impedance tomography (EIT) is a noninvasive, non-ionizing functional imaging technique that can be used in several medical applications such as monitoring the brain and heart activity [1, 2, 3], pulmonary ventilation [4, 5], and cancer detection [6, 7]. EIT systems can generate dynamic real-time images of the electrical conductivity in a region of interest using voltage measurements that arise from the application of low-amplitude, low-frequency AC currents. Several factors can influence the estimated conductivity in different regions of the body which include water and fat content, condition of the tissues, and bone structures - Table 1.1 shows the average conductivity values for different tissues [1, 8].

Table 1.1: Typical conductivity of several tissues.

Tissue	Conductivity $(\mathrm{mS/m})$
Blood	500-600
Lungs - end inspiration	42
Lungs - end expiration	138
Muscle	200-400
Fat	50
Bone	6

Most EIT applications are related to functional monitoring of the lungs [9, 10, 11]. EIT systems offer several advantages over other imaging modalities such as X-rays, Computed Tomography (CT), and Magnetic Resonance Imaging (MRI). EIT has high temporal resolution, is radiation-free, portable, and can be used at the bedside for continuous monitoring, which is not possible to achieve with CT and MRI systems, since patients have to be transferred to the radiology sector.

Although some X-ray machines can be used at the bedside, the application is more selective to Intensive Care Unit (ICU) [12], and due to ionizing exposure, X-ray exams are not used for long periods of time and not frequently.

The main disadvantage of EIT is that the inverse problem is severely ill-posed, which means that it is very sensitive to modeling errors and measurement noise. EIT also suffers from artifacts caused by out-of-reconstruction-plane currents and low spatial resolution due to the limited amount of electrodes that can be applied to the body, along with the ill-posedness of the EIT inverse problem. Moreover, EIT highly depends on good electrode attachment to the body.

EIT is an emerging imaging technique with high potential for cardiac and lung function monitoring. Thus, in the last few decades, EIT systems have been commercialized, making the EIT technology more well-known worldwide, as well as increasing the need for more accurate and sensitive EIT systems.

1.2 EIT Systems

PulmoVista 500 is an EIT system commercialized by Dräger-Germany which runs real-time EIT reconstructions by solving the inverse problem using a Newton-Raphson reconstruction algorithm and forward problem based on the Finite Element Method (FEM) at $20\,\mathrm{frames/sec}$ with adjustable options between 10-$50\,\mathrm{frames/sec}$ on a single row of 16 electrodes placed around the chest wall and ground electrode placed on the abdomen [13]. PulmoVista 500 applies pairwise patterns with maximum amplitude $9\,\mathrm{mA}$ with frequency between 80-$130\,\mathrm{kHz}$ to adjacent electrodes and measures the resulting voltages on the remaining 14 electrodes [13, 14].

Sentec-Switzerland commercializes the LuMon EIT system. LuMon runs real-time EIT reconstructions at $50\,\mathrm{frames/sec}$ or greater on a single row of 32 electrodes placed around the chest wall by applying pairwise-current patterns with maximum amplitude $3.7\,\mathrm{mA}$ at frequency $200\,\mathrm{kHz}$ to adjacent electrodes and measures the resulting voltages on the remaining 14 electrodes [15, 14].

Another commercial EIT system is ENLIGHT 2100 by Timpel-Brazil which runs real-time EIT reconstructions at $50\,\text{frames/sec}$ on a single row of 32 electrodes placed around the chest wall [16] by applying pairwise-current patterns at frequency $125\,\text{kHz}$ [14].

Adaptive Current Tomograph (ACT3) was a research EIT System developed at Rensselaer Polytechnic Institute (RPI) in 1994 that collects data at $18.5\,\text{frames/sec}$ on 32 electrodes that can be arranged in 2D or 3D configuration [17]. ACT3 had a parallel current drive and can apply current patterns and measure the resulting real and reactive voltages on all electrode configurations. The maximum current amplitude is $0.5\,\text{mA}$ with operation frequency at $28\,\text{kHz}$ [17, 14].

Based on the ACT3 model, General Electric (GE) developed in collaboration with the team at RPI a high-precision parallel current drive prototype EIT system called GE GENESIS that can simultaneously drive 32 independent current sources and measure 32 resulting voltages [18]. The GE GENESIS system applies maximum current amplitude of $0.120\,\text{mA}$ at $10\,\text{kHz}$ excitation frequency for both 2D and 3D electrode arrangements [18].

1.3 EIT Reconstruction Algorithms

One of the first 2D EIT reconstruction algorithms was a filtered backprojection algorithm introduced by Barber and Brown in 1984 [19]. Filtered backprojection algorithms are efficient with low computational cost, but due to the nonlinearity and ill-posedness of the EIT inverse problem, the reconstructed image resolution is poor [19], and there is no way to remove corrupted data, and no flexibility regarding the sequence of current injections and voltage measurements [1].

The most common 2D EIT reconstruction algorithms use iterative methods such as the one-step Newton-Raphson and one-step Gauss-Newton methods to solve a linearized EIT inverse problem and use FEM approximations to solve the forward problem, which can be applied to any domain of interest [20]. Another well-known 2D EIT reconstruction algorithm is Newton One-Step Error Reconstructor (NOSER), which is a linearized algorithm that takes one step in a Newton's method reconstruction with a constant admittivity initial guess that is the best constant admittivity fit to the measured data. [21]. The iterative EIT reconstruction algorithms are fast and can be implemented for real-time reconstruction display, but since they solve a linearized EIT inverse problem, it is more sensitive to noise and regularization strategies, and static images are very difficult to be obtained from human subject data.

Machine learning-based techniques have also been applied to EIT reconstruction algorithms. End-to-end algorithms use neural networks to train a network to produce images directly from the set of measured data [22]. Machine learning has also been used to improve the EIT spatial resolution through training sets derived from CT scans [23]. However, large studies are still needed to ensure that pathologies are accurately represented since the training sets are database-depended and may cause biased results [23].

Statistical inversion methods are also applied to the EIT reconstruction algorithms by using the Bayesian method to model the EIT inverse problem in the form of statistical inference from the distribution of the unknown parameters [24]. This method allows the incorporation of prior information in a controlled way into the calculations, and to obtain the full statistical description of the prior information and the measurements [24, 25]. However, the Bayesian methods highly depend on the prior, and are computationally expensive [26].

More complex direct (non-iterative) EIT algorithms that fully solve the non-linear EIT inverse problem have been developed. Calderón and D-bar methods [27, 28] use Complex Geometrical Optics (CGO) solutions and nonlinear Fourier transforms to solve the inverse problem [28].

While the state-of-the-art for commercial EIT systems is 2D tomographic imaging, it is well-known that 3D reconstruction algorithms increase accuracy and decrease artifacts caused by features above or below the plane of electrodes projected into the reconstructed slice.

2D EIT reconstructions are highly sensitive to objects that are above or below the electrode plane, and it was demonstrated on data collected in a cylindrical tank that by adding an additional electrode belt and using 3D current patterns, the artifacts from an out-of-plane target was reduced from 35% to 10% of the target value [8]. Moreover, using multiple rows of electrodes for 3D EIT imaging also provides more information about the region of interest since there are more reconstructed tomographic slices.

Three-Dimensional Linearized Reconstructor (ToDLeR) reconstruction algorithm was introduced by Goble in 1990, and Blue in 1997, which uses a linearization approach to solve the 3D forward problem considering a constant initial guess and the inverse 3D EIT problem [29, 8]. ToDLeR has been used to reconstruct images collected using the GE GENESIS system from patients with spinal muscular atrophy type I [30] and mechanically ventilated patients with acute respiratory distress syndrome (ARDS) [31], providing more information about ventilation and perfusion using the same total number of 32 electrodes as in the 2D reconstruction algorithms.

1.4 Adaptive Current Tomograph 5 (ACT5) System

The Electrical Impedance Tomography (EIT) Lab at Colorado State University (CSU) in collaboration with University at Albany (UAlbany) developed the new Adaptive Current Tomograph 5 System (ACT5) [14]. The team at UAlbany designed the hardware and the firmware for the Field Programmable Gate Array (FPGA) boards while the EIT lab implemented the software component that runs the ACT5 system.

The ACT5 system is a portable device that uses a laptop computer for full functionality. The design of the ACT5 system allows a flexible configuration that makes it possible to use different numbers of active electrodes and the application of any desired current patterns [32]. Moreover, the ACT5 system is also able to simultaneously measure electrocardiogram (ECG) signals on all active electrodes, which is not provided by any commercial system.

This dissertation describes all the components present in the software side of the ACT5 system, which include 2D and 3D EIT reconstruction algorithms, digital filters, a graphical user interface, and the preliminary data collection and EIT reconstructions on healthy controls and patients with cardiac or pulmonary diseases.

Since ACT5 is designed to monitor the thoracic region through the measurements of ventilation and pulsatile perfusion signals, a user-friendly clinical interface was developed to fully control the ACT5 system so that it can be used for human data collection at hospitals.

Both NOSER and ToDLeR algorithms were real-time implemented to produce real-time 2D and 3D reconstructions, respectively, from ACT5 data. Data collected on 2D and 3D tanks were used to test and optimize the reconstruction algorithms. Moreover, digital filters were designed to separate the ECG signal from the EIT signal.

1.5 EIT Applications

As part of this dissertation, 2D and 3D EIT data collection on human subjects were performed on healthy controls and patients at the University of Colorado Anschutz Medical Campus, Children's Hospital of Colorado, and in the EIT lab at CSU. The ACT5 system was used to image Cystic Fibrosis (CF) and Pulmonary Vein Stenosis (PVS) patients, and premature babies with Bronchopulmonary Dysplasia (BPD). Before the ACT5 system was built, the GE GENESIS system was used to image mechanically ventilated ARDS patients in collaboration with the GE Healthcare.

Patients with CF have a genetic condition that affects several organs including the lungs by causing long-term inflammation, which may lead to damage of lung tissues and respiratory failure [33]. Premature babies may develop different grades of BPD, which increases in severity due to the lungs not fully developing during gestation [34]. Patients with BPD usually receive respiratory therapy through non-invasive and invasive mechanical ventilation to help lung development. PVS is also one of the complications related to BPD. This disease causes one or more pulmonary veins to get narrower or be completely occluded, which increases the pulmonary pressure but also reduces the amount of blood circulating in the lungs [35]. ARDS causes fluid buildup which keeps the lungs from filling with enough air, leading to difficult breathing and eventually severe lung injuries. Patients with ARDS are mechanically ventilated, and one of the main challenges is to reduce ventilator-induced lung injury due to prolonged exposure or injurious ventilator settings.

We hypothesize that EIT can provide sensitive measures of changes in lung structure and function in patients of all ages, including the reversible conditions of air trapping and consolidation. Moreover, due to the high signal-to-noise ratio (SNR) and sensitivity of the ACT5 system [14], we hypothesize that patients with cardiac diseases that affect their lung perfusion will be captured by the pulsatile perfusion EIT image.

In this dissertation, EIT reconstructions of patients are compared to EIT reconstructions of healthy control subjects to assess the differences in lung structures during tidal breathing and pulsatile perfusion in both 2D and 3D EIT imaging. Longitudinal and statistical analysis were also performed to quantify the EIT-derived measures and how they correlate with the patient's clinical conditions.

Chapter 2

Background

2.1 Acute Respiratory Distress Syndrome (ARDS)

Acute Respiratory Distress Syndrome (ARDS) is a clinical syndrome caused by lung injury and inflammation which appears as hypoxaemia (low level of oxygen in the blood), pulmonary oedema, and reduced lung compliance [36] [37]. Despite the advances in the management of patients with ARDS that occurred in the last decades, ARDS continues to have a high mortality rate of 34.9%, 40.3%, and 46.1% in mild, moderate, and severe ARDS cases, respectively [38].

Since there are no drugs or therapies to treat ARDS, mechanical ventilation support is still the best practice for the management of patients with ARDS. The ventilator settings for lung protective ventilation in ARDS include low tidal volume ventilation to prevent tidal hyperinflation and the application of positive end-expiratory pressure (PEEP) to improve hypoxemia and limit cyclic atelectasis [39]. However, prolonged exposure to mechanical ventilation can also lead to Ventilator-Induced Lung Injury (VILI). Thus, determining when to begin the weaning process remains a daily challenge for ICU clinicians.

For patients in recovery, the decision to wean the patient from the ventilator is most often based on the clinical judgment of the physician [40]. This process takes into account personal experience and bedside observation of the evolution of parameters, usually blood gases, oxygen needs, and ventilator settings during a spontaneous breathing trial (SBT). Partially supported breathing modes may improve gas exchange, hemodynamics, and non-pulmonary organ perfusion and function, which is also associated with reduced sedation and prevention of disuse and loss of peripheral muscle and diaphragm function [41].

Patients who pass the SBT can attempt ventilator weaning and endotracheal tube removal. However, some patients develop respiratory failure after weaning and there is also evidence that indicates that the SBT may also cause or worsen acute lung injury [41] [42]. Thus, having more information about the patient's condition during an SBT along with the ventilator parameters may increase successful extubation.

Real-time EIT images of ventilation and pulmonary perfusion distribution during SBT could provide an objective measure to aid the physician in making a more informed determination regarding the likelihood of successful extubation, which could decrease the patient's overall days on the ventilator, as well as diminish the likelihood of re-intubation.

2.2 Cystic Fibrosis (CF)

Cystic fibrosis (CF) is the most common fatal genetic disease in the United States, and respiratory failure is the primary cause of mortality [33]. Recent studies show that lung disease commences very early in life in CF patients and is often initially silent [43][44][45].

Patients with CF are likely to experience acute Pulmonary Exacerbations (PEx), which are associated with lung function decline, leading to poor quality of life, increased hospitalizations, and decreased survival [46]. CF PEx rates increase with age and disease progression. Cystic Fibrosis Foundation registry data documented 27% of children with CF and 44% of adults with CF suffered an acute PE in 2013 [47].

Disease management and PE treatment decisions are often based on lung function information obtained either symptomatically or from pulmonary function tests (PFT's). However, most children under age 6 are unable to reliably perform the spirometry maneuvers in PFT's. Furthermore, this single index of lung function does not provide any regional or structural pulmonary information. Moreover, significant abnormalities are often visible in CT scans in children with CF whose PFT's fall in the normal range [45], indicating a lack of sensitivity in the PFT's to structural pulmonary changes. Thus, for better disease management, CF patients must be evaluated on functional and structural changes [45].

Computed tomography (CT) is the gold standard for assessing structural lung injury, but there is great concern about the long-term risks of CT due to ionizing radiation exposure [48], particularly for pediatric patients [49] and CF patients [50]. MRI techniques such as hyperpolarized helium [51] [52] [53], oxygen-enhanced MRI [54], and contrast-enhanced MR perfusion [55] have been demonstrated as techniques for assessing functional lung impairment in CF patients. These techniques are also safe and non-ionizing but are also still experimental. In addition, ventilation MRI has been shown to be sensitive to lung function abnormalities before changes are evident in spirometry [56] [57] [58]. However, regions of air trapping are not typically visible in ventilation MRI due to the low signal of normal lung parenchyma, which is not significantly decreased through an increase in air volume [59].

Because of the lack of a non-radiating alternative and since MRI techniques have the high cost of the hyperpolarizer and gases, and this technology is not widely available, the standard of care is for CF patients to have CT scans performed approximately every three years, and sometimes more often if clinically indicated. The reversible conditions of air trapping and consolidation can be seen in the CT scans, but due to radiation concerns, CT scans are not typically used to assess the success of antibiotic treatment for a PE. Thus, there is a need for an imaging technique to fill this clinical gap.

EIT has been demonstrated to be sensitive to peripheral airway changes [60] [61], and therefore it is expected that it can detect pulmonary inhomogeneities in very young patients, which is particularly useful since these patients cannot perform PFT's and are less likely to undergo a CT scan due to their age. Thus, EIT has strong potential as a monitoring tool for structural pulmonary changes that indicate disease progression and for assessing patient response to the treatment of PEx's, facilitating clinical decision-making about air clearance therapies and medications to treat reversible conditions and prevent further structural damage.

2.3 Bronchopulmonary Dysplasia (BPD)

Prematurity is defined as being born before 37 weeks of gestation. Risks of mortality and morbidity increase according to the degree of prematurity, with subcategories based on gestational age such as extremely preterm (less than 28 weeks), very preterm (28 to less than 32 weeks), and moderate to late preterm (32 to 37 weeks) [62].

Around 13.4 million preterm births occurred in 2020 worldwide, which accounts for about 10% of births in that year [62], and approximately 17% of children younger than 5 years who had been born preterm died due to preterm birth complications in 2019 [63]. In 2020, about 366,200 preterm births occurred in the USA alone, with a preterm birth rate of about 10% [62].

Premature babies have substantially higher risks of adverse outcomes with Bronchopulmonary dysplasia (BPD) being the most common and severe chronic respiratory illness among preterm-born infants [64]. Despite advances in neonatal care with conditions related to prematurity, leading to improved survival rates, there has been no decrease in the incidence of BPD among premature babies [65].

BPD is caused by abnormal lung development during gestation or not fully developing after being born prematurely, which results in ineffective gas exchange and leads to the need for respiratory support [34]. The current definitions of BPD based on the need for supplemental oxygen at 36 weeks post-menstrual age (PMA) divides BPD into low-flow nasal cannula (Grade 1), noninvasive positive pressure (Grade 2), and invasive positive pressure (Grade 3) [66].

BPD can lead to many cardio-respiratory and cognitive problems such as increased susceptibility to pulmonary infections, pulmonary hypertension, pulmonary vein stenosis, impaired executive functioning, delays in language development, and an increased risk of growth failure [67]. Currently, babies with BPD have been treated with bronchodilators, which cause the opening of the bronchi [66]. The treatment strategies have focused on reducing exposure to ventilation using an endotracheal tube, to avoid or minimize long-term lung damage in preterm infants [68].

EIT has the potential to monitor babies with BPD due to its capacity to show heterogeneity in ventilation and pulsatile perfusion images. There are no current studies using EIT to evaluate BPD effects in the respiratory system using ventilation and perfusion images to assess the patient's response to bronchodilators.

2.4 Pulmonary Vein Stenosis (PVS)

Pulmonary Vein Stenosis (PVS) is a complex and rare condition that can be seen in infants and children with congenital heart disease and also acquired in those patients after repair of Total Anomalous Pulmonary Venous Return (TAPVR) [69]. Moreover, despite being a rare disease, PVS is an increasing complication related to BPD due to premature birth, accounting for about 40% of all infants and children with PVS [70].

Because few centers have extensive experience in treating PVS, the characterization and understanding of the disease are still being established, with estimates of mortality ranging from 30% to 80% [69]. In PVS, pulmonary hypertension is more common, and patients may have diffuse or more localized evidence of pulmonary edema, based on the number of pulmonary veins involved. In addition, hemoptysis, coughing up blood, may occur more often in older patients [35].

Catheterization and echocardiography are the most common exams used to diagnose and monitor PVS patients [69, 71]. Catheterization provides anatomic detail and important hemodynamic information, but it is often used in patients with a high probability of requiring an intervention since it is an invasive exam and uses radiation [71] while echocardiography is radiation-free, non-invasive, and has a high diagnostic accuracy for detection of PVS and allows also the assessment of hemodynamics [72]. However, echocardiography fails to provide information about the lung conditions.

Computed tomography angiography (CTA) and magnetic resonance angiography (MR angiography) are also used to provide important hemodynamic data and anatomical information about pulmonary veins [71]. The downside of CT is the radiation exposure, which makes it infeasible for frequent monitoring and evaluation. Although MR angiography is non-ionizing, it has lower spatial resolution compared to CTA, it cannot be performed in patients with implanted non-compatible metal devices, and it requires a longer scanning time [72].

EIT has never been used to monitor and evaluate patients with PVS. Since it is a non-invasive, and non-ionizing image technique, EIT could provide spatial information about lung perfusion.

Moreover, EIT can be performed pre- and post- cardiac catheterization intervention to assess lung perfusion changes due to the intervention.

Chapter 3

Methods

3.1 Governing Equation

The governing equation of EIT is derived from Maxwell's equations. The magnetic field, $H(p,\omega)$ and electric field, $E(p,\omega)$, at an angular frequency, ω, at a point $\vec{p}$ within a domain B can be written as

$$\nabla \times H = (\sigma + i\omega\varepsilon)E, \tag{3.1}$$

$$\nabla \times E = -i\omega\mu H, \tag{3.2}$$

where $\sigma(\vec{p},\omega)$ is the electrical conductivity, $\varepsilon(\vec{p},\omega)$ is the electrical permittivity, and $\mu(\vec{p},\omega)$ is the magnetic permeability.

Since μ is small in the human body, one can take the approximation ($\mu = 0$) so that the electric field is described as $\nabla \times E = 0$. Moreover, the electric field can be expressed as the gradient of the electrical potential, u, given by

$$E = -\nabla u. \tag{3.3}$$

Using the property that the divergence of a curl is zero, and the magnetic field in eq. 3.1, we have that $\nabla \cdot ((\sigma + i\omega\varepsilon)E) = 0$. Thus, plugging in eq. 3.3 leads to the generalized Laplace equation

$$\nabla \cdot ((\sigma + i\omega\varepsilon)\nabla u) = 0, \tag{3.4}$$

which governs both the forward and inverse problems in EIT. In addition, since currents are applied to the body surface S, a Neumann boundary condition holds

$$\sigma(\vec{p},\omega)\frac{\partial u(\vec{p},\omega)}{\partial v} = j(\vec{p},\omega), \quad \text{for } \vec{p} \text{ on } S \tag{3.5}$$

where v denotes the outward unit normal to the body, and j is the current density. Since the amount of current entering and leaving the body must be the same due to the conservation of charge, we have

$$\int_S jdS = 0. \tag{3.6}$$

The applied currents on the body surface generate voltages, V, which corresponds to the Dirichlet boundary condition given by

$$u(\vec{p}, \omega) = V(\vec{p}, \omega), \quad \text{for } \vec{p} \text{ on } S \tag{3.7}$$

since equations 3.5 - 3.7 consider a continuous current density and voltage distribution, which is known as the EIT continuous model [21]. For convention and easy understanding in the following sections, the measured voltages from EIT systems are denoted V and the predicted voltages from solving the Laplace equation in 3.4 are called U.

3.1.1 Electrode Models

Gap Model: The Gap Model is a more realistic electrode model for EIT, which considers that the current can only be applied to the discrete electrodes and assumes that the voltages can only be measured at the center of these electrodes. Thus, equations 3.5 - 3.7 are modified to account for the gaps between the electrodes, and assumes that the current density is constant over the surface of each electrode, which leads to the following Neumann boundary condition

$$\sigma(\vec{p}, \omega)\frac{\partial u(\vec{p}, \omega)}{\partial v} = \begin{cases} \frac{I_l}{A_l} & \text{for } \vec{p} \in e_l, \quad l = 1, 2, ..., L \\ 0 & \text{for } \vec{p} \notin \bigcup\limits_{i=1}^{L} e_l \end{cases} \tag{3.8}$$

where L denotes the total number of electrodes on the surface S, e_l the lth electrode, I_l the applied current to the lth electrode, and A_l the area of the lth electrode. Also, the sum of the current applied to each electrode must be zero due to the conservation of charge

$$\sum_{1}^{L} I_l \; = \; 0, \tag{3.9}$$

and the measured voltages at the center of each electrode are expressed as

$$u(\text{center of } e_l) \; = \; V_l. \tag{3.10}$$

while sum of the voltages from each electrode

$$\sum_{1}^{L} V_l \; = \; 0, \tag{3.11}$$

must be zero for uniqueness of a solution to the forward problem.

If the impedance of the body B is known, the solution of the Laplace equation 3.4 for the gap model predicts voltages at the center of each electrode given by

$$U(\text{center of } e_l) \; = \; U_l. \tag{3.12}$$

where U is the solution of the Laplace equation for a known body impedance.

Ave-Gap Model: The Ave-Gap Model is an improvement over the Gap Model since instead of considering the voltages to be predicted only at the center of each electrode (eq. 3.12), this model accounts for the area of the electrode, predicting the resulting average voltages, $U_l^{ave-gap}$, at each electrode to be expressed as

$$U_l^{ave-gap} = \frac{1}{A_l} \int_{e_l} U_l(x,y) dxdy, \tag{3.13}$$

replacing the voltages in eq. 3.12.

3.2 Mesh

We can only have a finite number of electrodes L attached to the body, which leads to at most $K = L-1$ number of linearly independent current patterns that can be applied due to Kirchhoff's law, resulting in at most $K \times L$ number of measured voltages. Therefore, the conductivity is reconstructed using a piecewise constant on each element of a mesh expressed as [21]

$$\sigma(\vec{p}) = \sum_{n=1}^{N} \sigma_n \chi_n(\vec{p}), \tag{3.14}$$

where N is the total number of mesh elements, and $\chi_n(\vec{p})$ is the characteristic function that is 1 for $\vec{p}$ inside the nth mesh, or zero otherwise.

Since the relationship between applied current patterns $\vec{I}$ and measured voltages $\vec{V}$ is linear, this leads to at most $L(L-1)/2$ independent equations because there are only $L-1$ independent current patterns that can be applied when using trigonometric current patterns [73]. Therefore, the recommended number of mesh elements (N) to be used is [73]

$$N \leq \frac{L(L-1)}{2} \tag{3.15}$$

Figure 3.1 shows the Joshua tree mesh that is used in both NOSER and ToDLeR reconstruction algorithms. All elements in this mesh have the same area, and the positions of the elements are represented in polar coordinates instead of Cartesian coordinates. The elements are in polar coordinates because there are analytical solutions for both 2D and 3D forward problems of the Laplace equation using the separation of variables and Fourier expansions on the circle or on a cylinder, which are used in NOSER and ToDLeR.

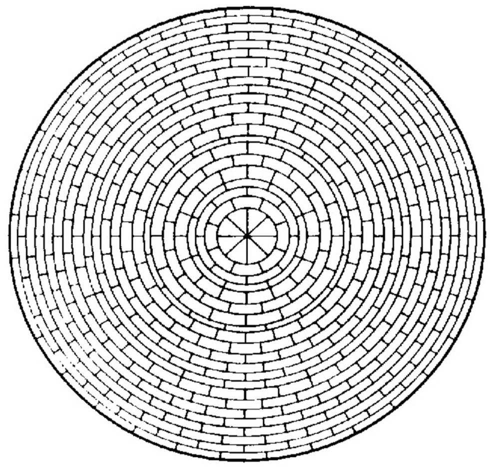

Figure 3.1: 496 elements Joshua tree mesh.

3.3 Geometry and Trigonometric Current Patterns

Both NOSER and ToDLeR reconstruction algorithms use the circular geometry approximations to solve the Generalized Laplace equation shown in eq. 3.4. Figure 3.2 shows a 2D circular phantom with electrodes evenly spaced around the surface with θ_l the angle to the center of each electrode from a reference angle $\theta = 0$, r_0 the circle's radius, θ_e the angular span of each electrode, e_w the electrode width, and e_h the electrode height in three dimensions. Current patterns $I^k = [I_1^k, I_2^k, ..., I_l^k]$, with $k = 1, 2, ..., K$ are applied to each electrode, e_l, while measuring the respective resulting voltages $V^k = [V_1^k, V_2^k, ..., V_l^k]$. The quantity I_l^k is the current amplitude and V_l^k is the measured voltage for the kth pattern applied to the lth electrode, where $K = L - 1$ is the total number of applied current patterns.

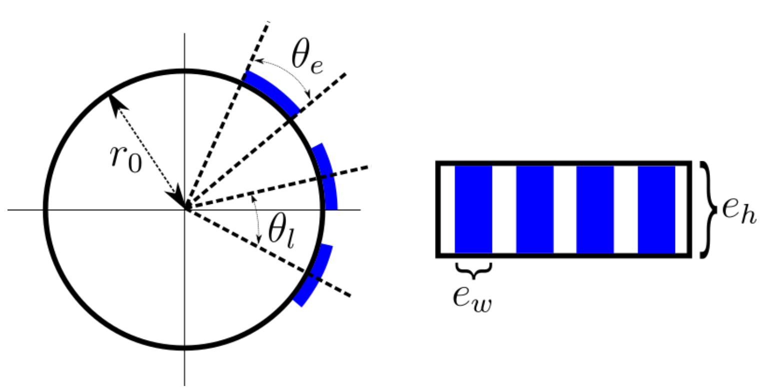

Figure 3.2: Top and side view of 2D phantom.

Trigonometric current patterns (I_l^k) give the best distinguishability for a circular inclusion in the center of a circular tank [74], which can be expressed as

$$I_l^k = \begin{cases} M\cos(k\theta_l) & k = 1,\ldots,L/2 \\ M\sin((k-L/2)\theta_l) & k = L/2,\ldots,L-1 \end{cases} \tag{3.16}$$

where $\theta_l = \frac{2\pi l}{L}$ for the 2D phantom, and the angular span of each electrode is defined as

$$\theta_e = \frac{e_w}{r_0}. \quad \text{[rad]} \tag{3.17}$$

Although these conditions are not true in the human body, the trigonometric current patterns may still give rise to measured voltages with a higher signal-to-noise ratio than those generated by pair-drive current patterns.

Figure 3.3 shows a 3D cylindrical phantom with two rows of electrodes used as a model for 3D EIT reconstructions. The rows of electrodes are separated by a vertical gap, V_{GAP}, with e_w being the electrode width and e_h the electrode height. In addition, h is the height of the cylinder, and Z_l is the distance from the bottom of the cylinder to the center of the lth row of electrodes.

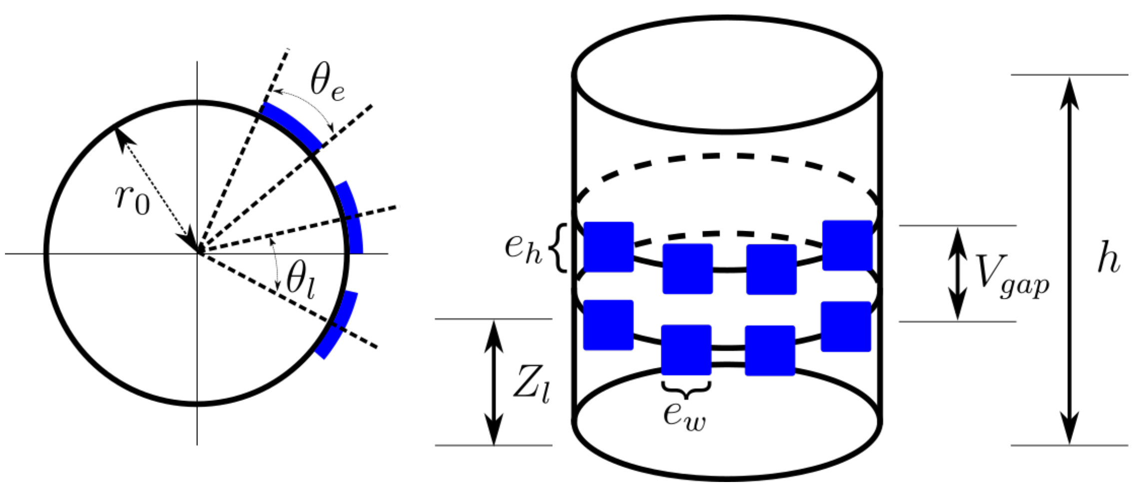

Figure 3.3: Top and side view of 3D cylindrical phantom.

For the 3D cylindrical phantom problem, the trigonometric current patterns also depend on the z component axis and the number of rows of electrodes. Thus, the optimal current patterns to be used on two of electrodes on a 3D cylinder tank are a combination of trigonometric functions in θ and z axes [29, 8] defined as

$$I_l^k = \begin{cases} M\cos(k\theta_l) & k = 1, ..., L/4 \\ M(-1)^{Z_0+1}\cos((k-L/4)\theta_l) & k = L/4+1, ..., L/2 \\ M(-1)^{Z_0+1} & k = L/2+1 \\ M\sin((k-L/2+1)\theta_l) & k = L/2+2, ..., 3L/4 \\ M(-1)^{Z_0+1}\sin((k-3L/4+1)\theta_l) & k = 3L/4+1, ..., L-1 \end{cases} \tag{3.18}$$

where

$$Z_0 = \begin{cases} 1 & \text{if } l = 1, \ldots, L/2 \\ 2 & \text{if } l = L/2+1, \ldots, L-1 \end{cases}$$
$$\theta_l = \begin{cases} \frac{4\pi l}{L} & \text{if } l = 1, \ldots, L/2 \\ \frac{4\pi(l-L/2)}{L} & \text{if } l = L/2+1, \ldots, L-1 \end{cases} \tag{3.19}$$

for the 3D phantom. Moreover, the gap boundary condition shown in eq. 3.8 is modified so that at the bottom or top of the cylinder the current is zero

$$\sigma([r,\theta,0],\omega)\frac{\partial u([r,\theta,z],\omega)}{\partial z} = \sigma([r,\theta,h],\omega)\frac{\partial u([r,\theta,z],\omega)}{\partial z} = 0$$

$$\sigma([r,\theta,z],\omega)\frac{\partial u([r,\theta,z],\omega)}{\partial r} = \begin{cases} \frac{I_l}{A_l} & \text{for } [r,\theta,z] \in e_l, \quad l = 1, 2, ..., L \\ 0 & \text{for } [r,\theta,z] \notin \bigcup_{i=1}^{L} e_l \end{cases} \tag{3.20}$$

3.4 NOSER Algorithm

The NOSER algorithm uses the same idea as the Newton-Raphson Method by guessing an initial constant distribution of conductivity $\vec{\sigma}$. However, in the NOSER solution, the resistivity, $\vec{\rho}$, is used instead of $\vec{\sigma}$, where $\vec{\rho}$ is its reciprocal resistivity for each element, ρ_n, given by

$$\rho(\vec{p}) = \sum_{n=1}^{N} \rho_n \chi_n(\vec{p}). \tag{3.21}$$

The NOSER algorithm seeks to minimize the sum of the squares of the differences between the measured and predicted voltages generated from known applied current patterns

$$E(\vec{p}) = \sum_{k=1}^{L-1} \left\| V^k - U^k(\vec{\rho_0}) \right\|_2^2 = \sum_{k=1}^{L-1} \sum_{l=1}^{L} (V_l^k - U_l^k(\vec{\rho_0}))^2 \tag{3.22}$$

where $E(\vec{p})$ is the error function, $U_l^k(\vec{\rho_0})$ is the predicted voltage for the kth pattern applied to the lth electrode with $\vec{\rho_0}$ as the initial guess. Thus, the minimization of $E(\vec{p})$ is the same as when finding the zero points of the derivative $\frac{\partial E(\vec{p})}{\partial \rho_n} = 0$, which is a necessary condition that leads to

$$F_n(\vec{p}) = \frac{\partial E(\vec{p})}{\partial \rho_n} = -2 \sum_{k=1}^{L-1} \sum_{l=1}^{L} (V_l^k - U_l^k(\vec{\rho_0})) \frac{\partial U_l^k(\vec{\rho_0})}{\partial \rho_n}. \tag{3.23}$$

To find $F_n(\vec{p}) = 0$, NOSER uses the one-step iteration of the Newton Raphson Method expressed as

$$\vec{\rho}_{NOSER} = \vec{\rho}_{old} - J_F^{-1}(\vec{\rho_0}) F_n(\vec{\rho_0}) \tag{3.24}$$

where $\vec{\rho}_{NOSER}$ is the reconstructed resistivity, and $J_F^{-1}(\vec{\rho}_0)$ is the regularized Jacobian matrix. The following steps show how to implement the NOSER algorithm [21].

Step 1: *Compute* $U_l^k(\vec{\rho}_0)$

For a constant $\vec{\rho}_0$, $U_l^k(\vec{\rho}_0)$ is the analytical solution of the Laplace equation using the Ave-gap boundary conditions, which predicts voltages on the electrodes to be as [75]

$$U_l^k(\vec{\rho}_0) = \frac{2r_0^2 e_h \rho_0}{\pi A_l} \sum_{n=1}^{\infty} [\frac{1-\cos(n\theta_e)}{n^3} \sum_{l^*=1}^{L} I_l^k \cos(n(\theta_l - \theta_{l^*}))] \tag{3.25}$$

where I_l^k is the kth 2D trigonometric current pattern applied to the lth electrode, and n is the number of harmonics.

Step 2: *How to pick* $\vec{\rho}_{old}$

Choose $\vec{\rho}_{old} = c\vec{1}$ where $\vec{1} = (1, \ldots, 1)$, and c is the best constant resistivity that minimizes eq. 3.22 when $\vec{\rho}_0 = \vec{1}$ which is

$$c = \frac{\sum_{k=1}^{L-1} \sum_{l=1}^{L} V_l^k U_l^k(\vec{1})}{\sum_{k=1}^{L-1} \sum_{l=1}^{L} (U_l^k(\vec{1}))^2} \tag{3.26}$$

Step 3: *Compute* $\frac{\partial U_l^k(\vec{\rho_0})}{\partial \rho_n}$

The derivative $\frac{\partial U_l^k(\vec{\rho_0})}{\partial \rho_n}$ can be computed by expanding it in the trigonometric basis using the inner products and the trigonometric current patterns $\vec{I}$

$$\frac{\partial U_l^k(\vec{\rho_0})}{\partial \rho_n} = \frac{\left\langle \vec{I}^s, \frac{\partial U_l^k(\vec{\rho_0})}{\partial \rho_n} \right\rangle}{\left\langle \vec{I}^s, \vec{I}^s \right\rangle}. \tag{3.27}$$

where $s = 1, \ldots, L-1$. The inner products in the denominator are normalization factors given by

$$\left\langle \vec{I}^s, \vec{I}^s \right\rangle = \begin{cases} \text{L/2} & s = 1, 2, \ldots, (L/2)-1, (L/2)+1, \ldots, L-1 \\ \text{L} & s = L/2 \end{cases} \tag{3.28}$$

and the numerator can be approximated as

$$Y^n_{s,k} = \left\langle \vec{I}^s, \frac{\partial U^k_l(\vec{\rho_0})}{\partial \rho_n} \right\rangle \approx \frac{1}{\rho_n^2} \int_{M_n} \nabla u^k \nabla u^s \tag{3.29}$$

where M_n is the nth mesh element, and u is the analytic forward solution of the Laplace equation considering the continuous electrode model and trigonometric current patterns given by

$$u^k(r,\theta) = \frac{M}{A_l} r_0 \begin{cases} \frac{\cos(k\theta)}{k}(\frac{r}{r_0})^k & k = 1,\ldots,L/2 \\ \frac{\sin((k-L/2)\theta)}{k-L/2}(\frac{r}{r_0})^{k-L/2} & k = L/2+1,\ldots,L-1 \end{cases} \tag{3.30}$$

Thus, solving eq. 3.29 results in the following equations [76]

Case 1: $k \le L/2, s \le L/2$

$$Y^n_{s,k} = (\frac{M}{A_l \rho_n})^2 \begin{cases} (\frac{1}{r_0})^{k+s-2} \frac{r_{n+1}^{k+s} - r_n^{k+s}}{k+s} \frac{\sin((k-s)\theta_{n+1}) - \sin((k-s)\theta_n)}{k-s}, & k \ne s \\ (\frac{1}{r_0})^{k+s-2} \frac{r_{n+1}^{k+s} - r_n^{k+s}}{k+s} (\theta_{n+1} - \theta_n), & k = s \end{cases} \tag{3.31}$$

Case 2: $k \le L/2, s \ge L/2+1$

$$Y^n_{s,k} = (\frac{M}{A_l \rho_n})^2 \begin{cases} (\frac{1}{r_0})^{k+s-\frac{L}{2}-2} \frac{r_{n+1}^{k+s-\frac{L}{2}} - r_n^{k+s-\frac{L}{2}}}{k+s-\frac{L}{2}} \frac{\cos((k-s-\frac{L}{2})\theta_n) - \cos((k-s-\frac{L}{2})\theta_{n+1})}{s-k-\frac{L}{2}}, & s-k \ne L/2 \\ 0, & s-k = L/2 \end{cases} \tag{3.32}$$

Case 3: $k \ge L/2+1, s \le L/2$

$$Y^n_{s,k} = (\frac{M}{A_l \rho_n})^2 \begin{cases} (\frac{1}{r_0})^{k+s-\frac{L}{2}-2} \frac{r_{n+1}^{k+s-\frac{L}{2}} - r_n^{k+s-\frac{L}{2}}}{k+s-\frac{L}{2}} \frac{\cos((k-s-\frac{L}{2})\theta_n) - \cos((k-s-\frac{L}{2})\theta_{n+1})}{k-s-\frac{L}{2}}, & k-s \ne L/2 \\ 0, & k-s = L/2 \end{cases} \tag{3.33}$$

Case 4: $k \geq L/2+1, s \geq L/2+1$

$$Y^n_{s,k} = (\frac{M}{A_l \rho_n})^2 \begin{cases} (\frac{1}{r_0})^{k+s-L-2} \frac{r_{n+1}^{k+s-L} - r_n^{k+s-L}}{k+s-L} \frac{\sin((k-s)\theta_{n+1}) - \sin((k-s)\theta_n)}{k-s}, & k \neq s \\ (\frac{1}{r_0})^{k+s-L-2} \frac{r_{n+1}^{k+s-L} - r_n^{k+s-L}}{k+s-L} (\theta_{n+1} - \theta_n), & k = s \end{cases} \tag{3.34}$$

where r_n is the radius from nth element in the mesh and θ_n the angle from nth element in the mesh.

Step 4: *Compute* $F_n(\vec{\rho_0})$ using eq. 3.23.

Step 5: *Compute the* ***A*** *matrix with entries* $A_{n,m}$

The entries $A_{n,m}$ are defined as

$$A_{n,m} = 2 \sum_{k=1}^{L-1} \sum_{l=1}^{L} \frac{\partial U_l^k(\vec{\rho_0})}{\partial \rho_n} \frac{\partial U_l^k(\vec{\rho_0})}{\partial \rho_m}. \tag{3.35}$$

Step 6: *Compute the Jacobian matrix* $J_F(\vec{\rho_0})$

The Jacobian matrix $J_F(\vec{\rho_0})$ is computed by regularizing the $A_{n,m}$ matrix

$$J_F(\vec{\rho_0})_{m,n} = A_{n,m} + \alpha A_{n,m} \delta_{m,n} \tag{3.36}$$

where $\delta_{m,n}$ is a delta function, which equals one if $n = m$, and zero otherwise, and α is the regularization parameter.

Step 7: *Compute* ρ_{NOSER} *using eq. 3.24, and then the resulting conductivity reconstruction by*

$$\sigma_{NOSER} = \frac{1}{\rho_{NOSER}} \tag{3.37}$$

3.5 ToDLeR Algorithm

The ToDLeR algorithm also solves the EIT inverse problem considering that the $\sigma_{ToDLeR}(\vec{p})$ conductivity distribution is a small perturbation, $\eta(\vec{p})$, from a constant conductivity, $\vec{\sigma_0}$, given by

$$\sigma_{ToDLeR}(\vec{p}) = \vec{\sigma_0} + \eta(\vec{p}), \quad \frac{\eta(\vec{p})}{\vec{\sigma_0}} \lll 1. \tag{3.38}$$

Considering a constant uniform conductivity distribution in the Laplace equation allows the linearization of the problem to be expressed as [77]

$$\int_B \eta(\vec{p}) \nabla u_0^{k1}(\vec{p}) \nabla u_0^{k2}(\vec{p}) d\vec{p} = \sum_{l=1}^{L} (I_l^{k2} V_l^{k2} - I_l^{k1} U_l^{k1}(\vec{\sigma_0})). \tag{3.39}$$

where $u_0^{k1}(\vec{p})$ is the solution of the Laplace equation at the point $\vec{p}$ when the $k1$th pattern is applied, V_l^{k2} is the measured voltages of $k2$th pattern applied to the lth electrode, $U_l^{k1}(\vec{\sigma_0})$ is the predicted voltage of $k1$th pattern applied to the lth electrode with $\vec{\sigma_0}$ as initial guess. Thus, after discretizing the above equation in terms of volume, it can be written as

$$\sum_{n=1}^{N} A_n^{k1,k2} \eta_n = \sum_{l=1}^{L} (I_l^{k2} V_l^{k2} - I_l^{k1} U_l^{k1}(\vec{\sigma_0})). \tag{3.40}$$

where n is the nth element, N is the total number of elements, η_n is the perturbation in the nth element, and

$$A_n^{k1,k2} = \int_{r_i}^{r_{i+1}} \int_{\theta_i}^{\theta_{i+1}} \int_{z_i}^{z_{i+1}} \nabla u_0^{k1} \nabla u_0^{k2} r dr d\theta dz. \tag{3.41}$$

Thus, eq. 3.40 can be written in a vector-matrix form as

$$\mathbf{A}\eta = \mathbf{d} \tag{3.42}$$

where

$$\mathbf{d} = \sum_{l=1}^{L} (I_l^{k2} V_l^{k2} - I_l^{k1} U_l^{k1}(\vec{\sigma_0})) \tag{3.43}$$

is the data term, $\mathbf{A}$ is the Jacobian of the forward model with respect to a small perturbation in conductivity, and η is the perturbation vector with size equals to the number of mesh elements N. Therefore, solving eq. 3.42 for η, we have that

$$\eta = \mathbf{J_F d} \tag{3.44}$$

where J_F is the regularized Jacobian matrix. Thus, using the best constant conductivity σ_{old} in eq. 3.38, the reconstructed ToDLeR conductivity is given by

$$\sigma_{ToDLeR} = \sigma_{old} + \eta. \tag{3.45}$$

The following steps show how to implement the ToDLeR algorithm [77].

Step 1: *Compute* $U_l^k(\vec{\sigma}_0)$

$U_l^k(\vec{\rho}_0)$ is the analytical solution of the Laplace equation using the Gap boundary conditions, which predicts voltages on the electrodes to be as [77]

$$U_l^k(\vec{\sigma}_0) = \sum_{n_F=1}^{\infty} r_0^{n_F}[a_{n_F}^k \cos(n_F\theta_l) + b_{n_F}^k \sin(n_F\theta_l)] +$$
$$\sum_{m_F=1}^{\infty}\sum_{n_F=0}^{\infty} B_{n_F}(\frac{m_F\pi r_0}{h})\cos(\frac{m_F\pi r_0}{h})[c_{n_F,m_F}^k \cos(n_F\theta_l) + d_{n_F,m_F}^k \sin(n_F\theta_l)] \tag{3.46}$$

where

$$a_{n_F}^k = \frac{2e_h\frac{\sin(n_F\theta_e)}{2}}{A_l\sigma_0\pi n_F{}^2 h r_0^{n_F-1}}\sum_{l=1}^{L} I_l^k\cos(n_F\theta_l), \tag{3.47}$$

$$c_{0,m_F}^k = \frac{2h\theta_e\sin(\frac{m_F\pi e_h}{2h})}{A_l\sigma_0\pi^3 m_F{}^2 B_0^{‘}(\frac{m_F\pi r_0}{h})}\sum_{l=1}^{L} I_l^k\cos(\frac{m_F\pi Z_l}{h}), \tag{3.48}$$

$$c_{n_F,m_F}^k = \frac{8h\sin(\frac{n_F\theta_e}{2})\sin(\frac{m_F\pi e_h}{2h})}{A_l\sigma_0\pi^3 m_F{}^2 n_F B_{n_F}^{‘}(\frac{m_F\pi r_0}{h})}\sum_{l=1}^{L} I_l^k\cos(\frac{m_F\pi Z_l}{h})\cos(n_F\theta_l), \tag{3.49}$$

$$b_{n_F}^k = \frac{2e_h\frac{\sin(n_F\theta_e)}{2}}{A_l\sigma_0\pi n_F{}^2 h r_0^{n_F-1}}\sum_{l=1}^{L} I_l^k\sin(n_F\theta_l), \tag{3.50}$$

$$d_{0,m_F}^k = 0, \tag{3.51}$$

$$d_{n_F,m_F}^k = \frac{8h\sin(\frac{n_F\theta_e}{2})\sin(\frac{m_F\pi e_h}{2h})}{A_l\sigma_0\pi^3 m_F{}^2 n_F B_{n_F}^{‘}(\frac{m_F\pi r_0}{h})}\sum_{l=1}^{L} I_l^k\cos(\frac{m_F\pi Z_l}{h})\sin(n_F\theta_l), \tag{3.52}$$

and $B^{`}_{n_F}(x)$ is the first derivative of the modified Bessel function

$$B_{n_F}(x) = \sum_{m_F}^{\infty} \frac{1}{m_F!(m_F+n_F)!}(\frac{x}{2})^{2m_F+n_F} \tag{3.53}$$

with n_F and m_F being the number of harmonics in the Fourier Series.

Step 2: *How to pick σ_{old}*

Choose $\vec{\sigma}_{old} = c\vec{1}$ where $\vec{1} = (1, \ldots, 1)$, and c is the best constant conductivity given by

$$c = \frac{\sum_{k=1}^{L-1}\sum_{l=1}^{L}(U_l^k(\vec{1}))^2}{\sum_{k=1}^{L-1}\sum_{l=1}^{L}V_l^k U_l^k(\vec{1})} \tag{3.54}$$

Step 3: *How to compute $A_n^{k1,k2}$*

The integrals in eq. 3.40 can be solved as [77]

$$\begin{aligned} A_n^{k1,k2} = &\sum_{n_F=1}^{N_F}\sum_{n_F=1^{`}}^{N_F}[FR_{11}FZ_{11}(F\Theta_{11}+F\Theta_{21})]+ \\ &\sum_{n_F=1}^{N_F}\sum_{m^{`}_F=1}^{N_F}\sum_{n^{`}_F=0}^{N_F}[FR_{121}FZ_{12}F\Theta_{12}+FR_{122}FZ_{12}(F\Theta_{12}+F\Theta_{22})]+ \\ &\sum_{n^{`}_F=1}^{N_F}\sum_{m_F=1}^{N_F}\sum_{n_F=0}^{N_F}[FR_{131}FZ_{13}F\Theta_{13}+FR_{132}FZ_{13}(F\Theta_{13}+F\Theta_{23})]+ \\ &\sum_{m_F=1}^{N_F}\sum_{n_F=0}^{N_F}\sum_{m^{`}_F=1}^{N_F}\sum_{n^{`}_F=0}^{N_F}[FR_{14}FZ_{14}F\Theta_{14}+FR_{144}FZ_{14}F\Theta_{24}+FR_3FZ_3F\Theta_{14}] \end{aligned} \tag{3.55}$$

where the definition of the parameters can be found in Appendix A.

Step 4: *Compute **d** using eq. 3.43*

Step 5: *Compute the J_F matrix*

The Jacobian matrix J_F is computed by regularizing the A matrix

$$J_F = [A^TA + \alpha_1 A^TA\delta + \alpha_2 max(A^TA)\delta]^{-1}A^T \tag{3.56}$$

where δ is a delta function, and α_1, α_2 are the regularization parameters.

Step 6: *Compute* η *using eq. 3.44*

Step 7: *Compute* σ_{ToDLeR} *using eq. 3.45*

3.5.1 2D ToDLeR Solution

The NOSER algorithm does not take into account the out-of-plane currents that are projected onto the plane of electrodes since NOSER solves the 2D EIT inverse problem. The ToDLeR algorithm solves the inverse problem using a cylinder model, which accounts for the height of the body h.

To compare the effects of out-of-plane currents on the EIT reconstructions when using NOSER, ToDLeR was solved considering only a single row of electrodes. The steps to solve the 2D ToDLeR algorithm are the same as the one presented in this section, with the only difference being that $Z_l = \frac{h}{2}$, $\theta_l = 2\pi l/L$, and the 2D trigonometric patterns are applied.

3.6 Regularization

Due to the ill-conditioning of the EIT inverse problem, the EIT reconstructions are influenced by the size, number, and position of the mesh elements [21]. An ill-posed problem is a problem whose solution is not unique or does not depend continuously on the data. Thus, when solving a linearized EIT inverse problem, which can be approximated as [27]

$$Af + \varepsilon = m \tag{3.57}$$

where A is the coefficient matrix resulted from the forward problem, f is the quantity of interest, ε is the noise, and m is the measurement data term, the coefficient matrix A is very ill-conditioned or singular. Therefore, regularization techniques are used to better condition the A matrix.

3.6.1 NOSER type Regularization

The NOSER type regularization is a simple diagonal weighting for the A matrix given by [21]

$$J_F = A + \alpha A \delta \tag{3.58}$$

where J_F is the regularized coefficient A matrix, α is the constant regularization parameter, and δ is the Kronecker delta function. Small values of α lead to better contrast and definition but can make the reconstructed images noisier if it is too small. Conversely, large values of α cause more smoothing and blurring effects [8].

3.6.2 Tikhonov Regularization

Tikhonov Regularization uses a constant positive diagonal matrix that adds positive elements to the diagonal of the A matrix, penalizing large perturbations and making it better conditioned, but large values of α decrease the contrast in the reconstructed images [8]

$$J_F = A + \alpha \delta \tag{3.59}$$

3.6.3 Mixed Regularization

NOSER type and Tikhonov regularizations cause different effects on the reconstructed images. By combining these two methods, we can get better target definition and contrast in 3D reconstructed images [8]. Therefore, the mixed regularized matrix can be expressed as

$$J_F = A + \alpha_1 A \delta + \alpha_2 \delta \tag{3.60}$$

3.7 Conformal Map for Display

NOSER and ToDLeR are reconstruction algorithms that use circular and cylindrical domains to solve both the forward and inverse problem. One of the main advantages over other iterative reconstruction algorithms that require successive solutions of the forward problem using a numerical solver such as the FEM is the fast computation of the Jacobian matrix.

Despite being a good approximation, the human chest shape is not circular or cylindrical, which brings the need for a chest shaped reconstruction display for NOSER and ToDLeR. This can be obtained by using the conformal mapping technique, which is a function on the complex plane that maps a given curve to another plane preserving each angle of that curve.

Since the human chest shape can vary by age, gender, muscular structure, and other factors, there is no defined equation that maps a circle to a chest shaped domain. Thus, the approach we use to conformally map a circle to a chest shaped domain is that any point on a circle can be mapped to a chest shape domain by multiplying the radius, r^{circle}, by a factor, $T(\theta)$, where θ is the angle of a point on the circle curve and chest shape curve, and T is the factor that multiplies the radius of the circle as shown in Figure 3.4(a). Therefore, after discretizing the circle, the conformally mapped radius, r_n^{chest}, can be expressed as

$$r_n^{chest}(\theta_n) = T(\theta_n) r_n^{circle} e^{i\theta_n} \tag{3.61}$$

where n is the nth element in the mesh. In a real application, we obtain an approximation to both $r_n^{chest}(\theta_n)$ by using CT images or 3D scans, and $r_n^{circle} e^{i\theta_n}$ from the measured chest circumference. To find $T(\theta_n)$, we first need to center the circle and the arbitrary chest shape at $(0, i0)$, and then compute $T(\theta_n) = r_n^{chest}(\theta_n)/r_n^{circle} e^{i\theta_n}$ starting at the outermost mesh radius from the Joshua tree mesh. After finding $T(\theta_n)$, the inner Joshua tree mesh radii can be used to calculate the inner conformal map chest shape radii using $T(\theta_n)$ as illustrated by the red and blue dashed lines in Figure 3.4(b). In addition, since we are only using the conformal map for display and not for solving the forward and inverse problems, we do not need to make sure that the conformally mapped circumference matches the length of the measured chest shape circumference.

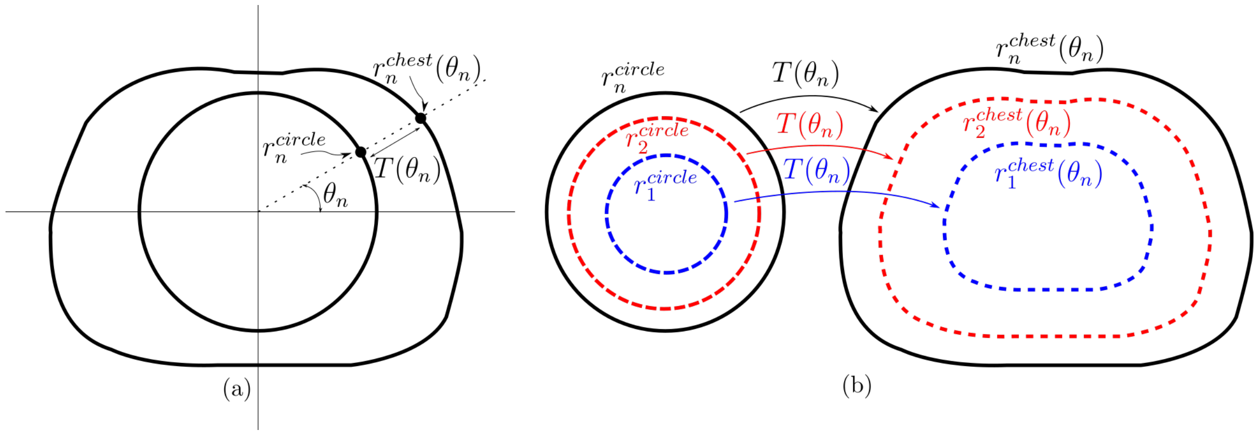

Figure 3.4: Conformal Map schematic. (a) Determining $T(\theta_n)$, and (b) computing the inner $r_n^{chest}(\theta_n)$.

3.7.1 Matrix Display

To display the reconstructed conductivity at each mesh element, the Joshua tree mesh, which is in the polar coordinate system, has to be mapped onto the Cartesian coordinate system. This can be done by creating a matrix, m, with size $M \times M$ where each element index of the matrix is represented as (x, iy) complex coordinate. Thus, since the elements, e_n, in the Joshua tree mesh are expressed as $e_n(r_n, r_{n+1}; \theta_n, \theta_{n+1})$, by looping through all the matrix m element indices, we can have that

$$m(x, y) = n, \quad \text{if } (x, iy) \in e_n(r_n, r_{n+1}; \theta_n, \theta_{n+1}) \tag{3.62}$$

where $n = 1, \ldots, N$ is the nth element, N is the total number of mesh elements.

Figure 3.5 illustrates a Joshua tree element represented in the Cartesian coordinate system. We can see that the mapping depends on the size of the matrix m, where the more elements it has the better the resolution when mapping the Joshua tree element in the Cartesian coordinate system. Moreover, to make sure there are no empty spaces in the matrix m, a tolerance is added when checking if $(x, iy) \in e_n(r_n, r_{n+1}; \theta_n, \theta_{n+1})$ so that it fills the empty spaces with neighboring elements. The same approach is also used when mapping the conformal chest shape into the Cartesian coordinate system.

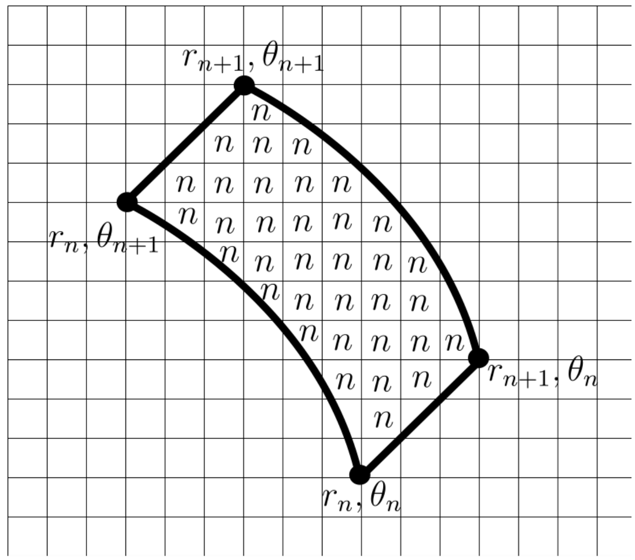

Figure 3.5: Joshua tree element mapped in the Cartesian coordinate system.

3.8 GENESIS EIT System

The GENESIS prototype EIT system from GE Research is a 32-channel simultaneous multiple current source EIT system that collects data and displays real-time images at $18\,\mathrm{frames/sec}$ [18]. This system can apply trigonometric current patterns and measure complex voltages using National Instruments devices with SNR$>100\,\mathrm{dB}$ and current amplitude up to $0.120\,\mathrm{mA}$ peak-to-peak at $10\,\mathrm{kHz}$ excitation frequency [18].

An engineering GUI displays the 3D EIT reconstructions on a circular shape using the ToDLeR algorithm in real-time as well as heart and lung conductivity traces. It also allows the operator to include annotations during the data collection. Since the GENESIS system is a prototype, the main disadvantage is that it can collect data while some electrodes are not attached to the subject's body without halting data collection. This can lead to poor data quality since no message is shown regarding the electrode connections during the data collections, and it also requires the operators to have skills to identify poor electrode connections by looking at the reconstructed images.

Figure 3.6: GENESIS EIT System.

3.9 Adaptive Current Tomograph 5 (ACT5) System

The ACT5 System was developed in collaboration with the team at University at Albany. Figure 3.7 shows the ACT5 System hardware including the laptop that runs the clinical user interface. It is a portable device fitted in a box of size $54\,\mathrm{cm} \times 32\,\mathrm{cm} \times 23\,\mathrm{cm}$ and weighs approximately $22.5\,\mathrm{kg}$. The system interfaces with an external laptop through a USB connection, making it a standalone portable unit [14].

Figure 3.7: ACT5 System.

The ACT5 system can apply any complex current pattern with both the amplitude and phase of each current source being individually controllable [14]. This provides the ability to apply either 2D or 3D trigonometric current patterns as well as optimal current patterns for a given target, making the ACT5 system more flexible to be used in different applications.

The main application of the ACT5 system is to monitor the respiratory system by providing real-time ventilation and pulsatile perfusion EIT reconstructions in both 2D and 3D electrode configurations using up to 32 electrode leads using a Clinical User Interface. Moreover, the ACT5 System simultaneously measures electrocardiogram (ECG) and EIT signals on all electrode leads in real-time, and has control features that halt data collection when electrodes are not attached to the body. Table 3.1 summarizes the specifications of the ACT5 System and the Dell Precision 7750 laptop.

Table 3.1: ACT5 System Specifications [14].

Property	Values
Default Number of Active Electrodes	16 or 32
Max. Current (each Electrode)	$1\,\mathrm{mA}$ peak-to-peak
Max. Voltage	$1\,\mathrm{V}$ peak-to-peak
Voltage Measurement	Complex
SNR	$>100\,\mathrm{dB}$
Frequency Range	$5\,\mathrm{kHz}$ to $500\,\mathrm{kHz}$
Frame Rate (32 Electrodes)	$27\,\text{frames}/\mathrm{sec}$
Frame Rate (16 Electrodes)	$54\,\text{frames}/\mathrm{sec}$
Cable Length	Adjustable (Default: $2\,\mathrm{m}$)
ECG	Measured on all Electrodes
ECG Sampling Rate	$864\,\mathrm{Hz}$
Processor	Intel 8-core processor i9-10885H
Operating System	Windows 10, 64-bit
Video card	NVIDIA Quadro RTX 4000 - 8GB GDDR6
Memory	32GB, 2x16GB
Hard Drive	512GB

3.9.1 Simultaneous ECG and EIT measurement

The ACT5 System can measure EIT and ECG signals simultaneously on all electrodes, however, the separation of both signals is not an easy task. The large amplitude in the EIT signal which allows a maximum swing of $1\,\mathrm{V}$ for the measured EIT voltage is about three orders of magnitude higher than a usual measured ECG signal that ranges in mV [78]. Moreover, although there is a large frequency difference between the EIT ($5\,\mathrm{kHz}$ to $500\,\mathrm{kHz}$) and ECG signals ($0.5\,\mathrm{Hz}$ to $150\,\mathrm{Hz}$), the $1.2\,\mathrm{MHz}$ clock used in ACT5 would require the use of high precision coefficients for a digital low pass filter in a fixed-point format, and down-sampling would not work since the aliasing of EIT signals into the ECG bandwidth would be more likely to happen [78].

Figure 3.8 shows the block diagram for the separation of the EIT and ECG signals. The integrate-and-dump filter completely removes frequency components at the EIT excitation frequency and its harmonics because EIT excitation frequencies are selected such that an integral number of cycles will occur over 1024 samples at the $1.2\,\mathrm{MSample/s}$ sampling frequency [78]. However, since the ACT5 System uses DC-blocking capacitors between the electronics and the electrodes to suppress the DC signal and ensure that it will not be applied to the subject, at the end of the EIT excitation burst, these capacitors may have some residual charge, which can create frequency components at the EIT frame rate ($27\,\text{frames}/\mathrm{sec}$ or $54\,\text{frames}/\mathrm{sec}$), and its harmonics. Thus, some interfering frequencies related to the EIT frame rate still remain after the integrate-and-dump filter stage, and because some of these frequencies are below $150\,\mathrm{Hz}$, the ECG bandwidth is corrupted by the interfering frequencies. In addition, the integrate-and-dump filters fail to block any power line interference noise [78].

Digital notch filters could be used to suppress the interfering frequencies and their harmonics since the EIT frame rate and the power line frequency are known and fixed. However, the standard finite and infinite impulse response filters cannot remove the harmonics without attenuating frequencies from the ECG signal because of limited quality factors, making them unfeasible. A better approach is to use an adaptive filter to subtract components at the frame rate and its harmonics as well as the USA power line frequency of $60\,\mathrm{Hz}$ and its harmonics, up to $150\,\mathrm{Hz}$. This approach will

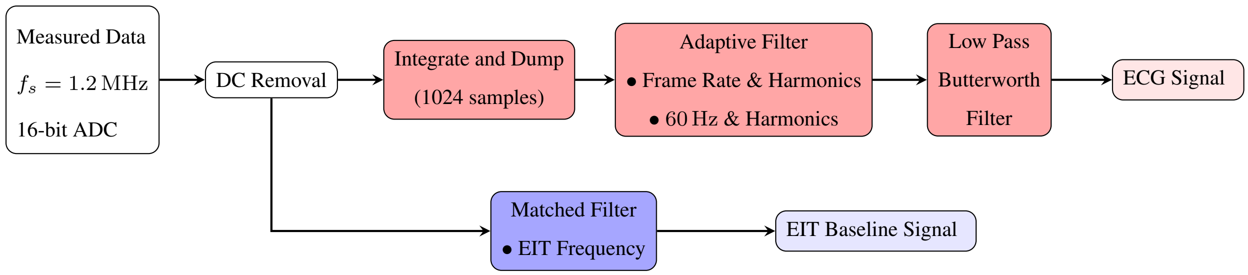

Figure 3.8: A block diagram of the simultaneous EIT/ECG system.

remove only the interfering frequency components, effectively implementing a set of very narrow bandwidth notch filters.

The implementation of the adaptive filter uses the least mean square (LMS) algorithm to minimize the residual signal at the interfering sinusoidal frequencies [79]. Figure 3.9 shows the block diagram of an LMS adaptive filter that can be used to remove a sinusoidal interference. The reference signals $u_1[n-i]$ and $u_2[n-i]$ are multiplied by the adaptive tap weights $W_i^1[n]$ and $W_i^2[n]$ to produce $y[n]$

$$y[n] = \sum_{i=0}^{M-1} W_i^1[n]u_1[n-i] + W_i^2[n]u_2[n-i], \quad i = 0, \ldots, M-1, \tag{3.63}$$

where

$$\begin{aligned} u_1[n] &= A_c \cos\left(2\pi f_k n T_s + \phi\right), \\ u_2[n] &= A_c \sin\left(2\pi f_k n T_s + \phi\right), \end{aligned} \tag{3.64}$$

M is the order of the LMS filter, f_k is the frequency of the sinusoidal interference, T_s is the ECG sampling interval, ϕ is the the phase, and n is the time increment. $y[n]$ is subtracted from the primary signal $x[n]$ which, in this case, is the ECG signal with the interference sinusoidal frequencies [79].

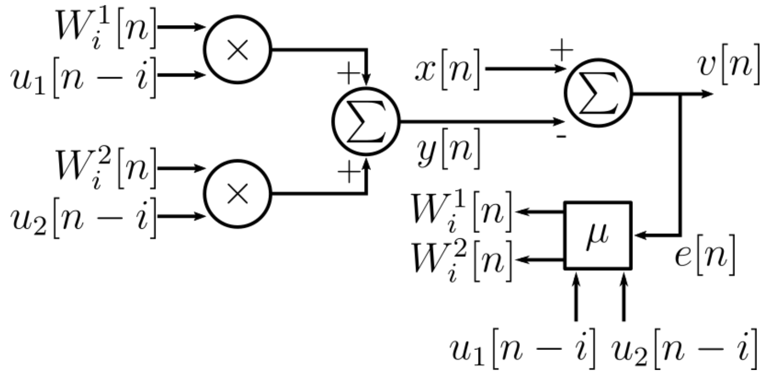

Figure 3.9: Adaptive LMS Filter diagram.

The Adaptive LMS filter implementation shown in 3.9 differs from the classical implementation in [79] and [80] by adding the u_2 and W_i^2 terms which include the sine function as a reference signal. Since the classical implementation only considers a cosine function as the reference signal, it will cause undesired time-varying effects to create distortions around f_k for low-order LMS filters due to the phase ϕ in the reference signal [80]. Thus, by adding a sine function as a reference signal the time-varying effects are removed, which allows the implementation of a low-order LMS filter [81].

The adaptive filter tap weights ($W[n+1]$) are adapted using [81]

$$\begin{aligned} W_i^1[n+1] &= W_i^1[n] + \mu e[n] u_1[n-i], \\ W_i^2[n+1] &= W_i^2[n] + \mu e[n] u_2[n-i], \end{aligned} \tag{3.65}$$

where μ is the step-size parameter and $e[n] = x[n] - y[n]$ is the error signal which is also equals to the filter output $v[n]$. Since the adaptive LMS filter approach shown in Fig. 3.9 removes a single interfering frequency, to suppress all harmonic interfering frequencies (f_k), adaptive LMS filters were implemented for each f_k and then cascaded where the primary signal for each subsequent filter is the filter output $v[n]$ from the previous stage and the reference signals $u_1[n]$ and $u_2[n]$ are the sine and cosine of the next frequency to be suppressed.

Following the medical standards for the ECG bandwidth, a low-pass Butterworth filter using the `filtfilt` function from MATLAB [82], with a cutoff frequency of $150\,\mathrm{Hz}$, was used as a final stage of filtering for the received ECG signal for offline post-processing. During real-time data collection, the low-pass Butterworth filter is implemented using the general infinite impulse response difference equation

$$\sum_{i=0}^{N} a_i y[n-i] = \sum_{j=0}^{M} b_j x[n-j] \tag{3.66}$$

where, $N+M+1$ is the total amount of coefficients, $y[n]$ is the filter output, $x[n]$ is the filter input, and a_i, b_j are the filter coefficients. Moreover, the `butter` function from MATLAB was used to find the filter coefficients a_i and b_j.

The low-pass Butterworth filter suppresses the remaining harmonic interfering frequencies (f_k) above $150\,\mathrm{Hz}$ as well as high-frequency noise. Moreover, the lower cutoff frequency is set to $0.159\,\mathrm{Hz}$ by the AC coupling prior to the ADC in ACT5 [83, 14].

3.9.2 Clinical User Interface

The Clinical User Interface that runs on the ACT5 system was developed in the Electrical Impedance Tomography Laboratory at Colorado State University using the MATLAB app designer for Graphical User Interface (GUI) development in standalone applications. The clinical interface was designed to be user-friendly so that operators can easily use the ACT5 System for data collection without the need to run the MATLAB software. This can be done by running a desktop executable created through the MATLAB Standalone toolbox. Figure 3.10 illustrates the executable with the designed ACT5 logo.

Figure 3.10: ACT5 logo.

The Clinical User Interface controls both the hardware and the EIT reconstructions display in real-time, including the ECG measurements and its display. Figure 3.11 shows the *Login Window* where the operator inputs information about the data collection which is used to run the reconstruction algorithms with proper parameters and also keep track for later offline processing. The *Login Window* provides the following field options:

Operator: Name of the person who is doing the data collection.

Location: Location where the data was collected.

Number of Electrodes per Row: The Number of Electrodes per row.

Size(mm): Electrode width and height in millimeters.

Electrode Type: Choose either a circular or rectangular shape.

Subject ID: A chosen number given to a subject.

File Name: Enter the file name. The data will be saved with the chosen file name plus the day and time stamp. However, special characters cannot be used as file name to avoid data corruption.

Circumference (in): Subject's chest circumference in inches.

Vertical Gap (cm): Center-to-center vertical gap in centimeter between the two rows of electrodes when using a 3D configuration.

Horizontal Gap: Display to users the horizontal gap between electrodes in cm. This is used for electrode spacing. If this number is negative, it means that the current amount of electrodes will not fit the subject's chest.

Shape: Chooses between chest shape or circular shape for the reconstruction display.

The *Main Window* of the ACT5 interface is shown in Figure 3.12, and it displays the reconstructions of the real and imaginary parts of the admittivity distribution, i.e. the conductivity and susceptivity ($\omega\varepsilon$, where ω is the angular frequency and ε is the electric permittivity), and a real-time ECG signal obtained by taking the difference between ECG signals from a pair of electrodes. This ECG signal is time-aligned with the reconstructed images [14]. The *Main Window* can be further described by the following blocks:

Block 1: Operator, location, date, and time are displayed on the interface.

Figure 3.11: Clinical User Interface - Login window.

Block 2: Contains the electrode contact status and message box. If an electrode is loose, it will be displayed in black color while the good contact is green color. The message box displays messages about the ACT5 system's operation as well as errors that may occur during the data collection.

Block 3: Controls the range of the reconstruction displays, adds annotations during the data collection, and allows setting the reference frame for the real-time EIT reconstructions.

Block 4: Allows the adjustment in real-time of γ_1 and γ_2 regularization parameters, ECG Filter μ factor and, ECG y-axis control display and heart rate (HR) display. Also, it shows the Safety status with a green color meaning that safety is on, and a red color when it is off. Although the data is saved automatically after the data collection is done, the save button is another alternative in case there are any issues with auto-saving.

Block 5: Shows the 2D or 3D EIT reconstructions of conductivity and susceptivity, and ECG measurement. Allows the toggle to a screen that displays the DC voltages on electrodes when the same small current is applied to all electrodes, which is useful for assessing real-time poor electrode contact, and to another screen that displays in real-time the real and imaginary parts of σ_{best}, which can be used to identify ventilation and perfusion segments.

Block 6: Run, Stop, Options, and Reset buttons. The Run button will initiate the data collection while the Stop button will halt data collection and automatically save the data. The Options button gives access to *Options Window*, and the Reset button allows the resetting of the hardware when a trip occurs. This is usually caused by bad electrode connections. Also, the Reset button turns red for easy identification when the hardware needs to reset.

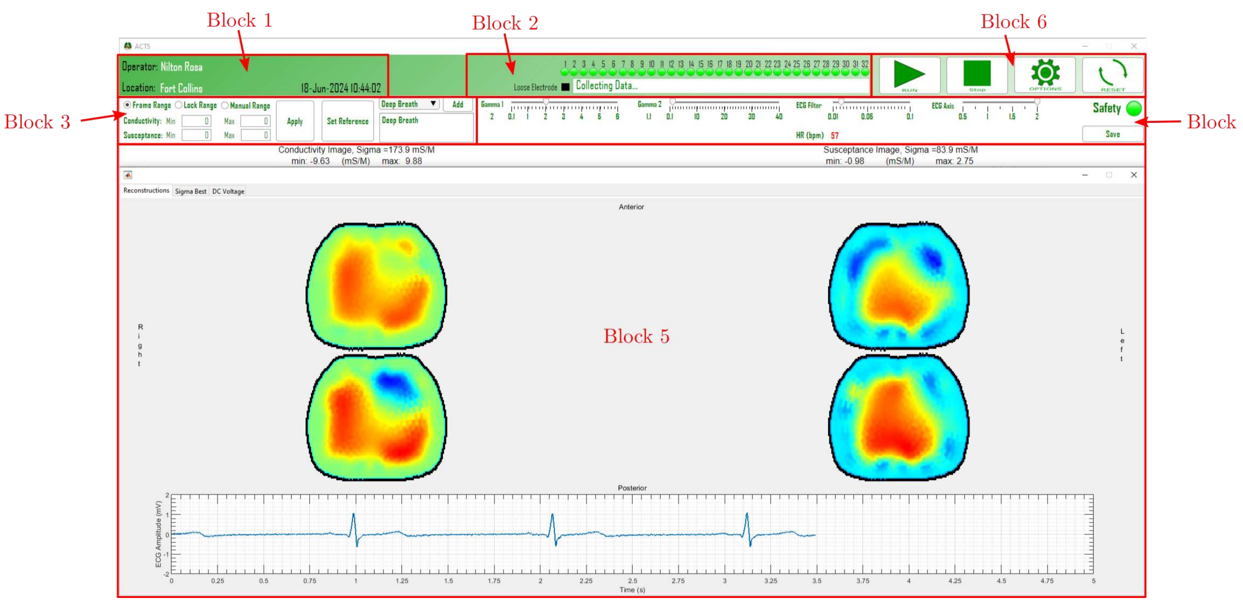

Figure 3.12: Clinical User Interface - Main window.

Figure 3.13 shows the *Options Window* which allows the operator to choose the data collection duration by selecting Continuous (1-hour) - default, 60 seconds, and Snapshot. The optimal mode is still in development but it allows the ACT5 system to apply optimal current patterns, and the offline mode can be used to load any data collected with ACT5 and choose the start, end, and reference frames for offline reconstruction display using the Clinical User interface. Moreover, the offline mode records and saves the time-sequence reconstruction videos.

The *Options Window* also has the MEAN Baby and Developer menu buttons. The MEAN baby button runs a modified NOSER algorithm which uses *a priori* information to improve reconstruc-

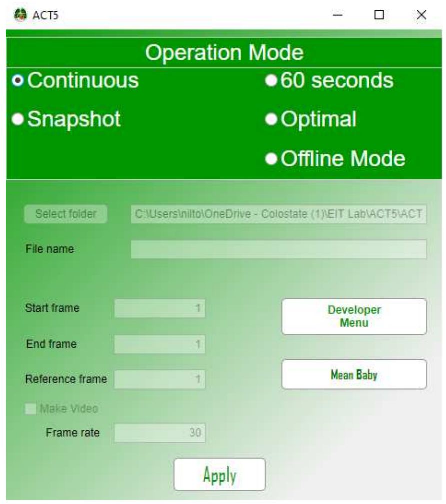

Figure 3.13: Clinical User Interface - Options window.

tions [84]. The developer menu button gives access to the *Developer Menu Window* which can only be accessed by entering a password, allowing only authorized personnel to access and change the ACT5 System parameters.

The *Developer Menu Window*, shown in Figure 3.14, was created so that parameters of the ACT5 System can be changed without having to manually do it by rewriting code sections, and therefore, only authorized personnel can access this menu. Having the ACT5 parameters on the Clinical User Interface also avoids issues such as turning the safety off for testing, and not turning it back on, which is more likely to happen when modifying codes.

The *Developer Menu Window* allows the operator to change the operation frequency, cable calibration, total number of frames per file, number of iterates during optimal patterns mode, the applied current amplitude, rearrange the current patterns by spatial frequency, change the file name, selected new current patterns, apply the identity matrix as current pattern and turn the safety off, which are used for troubleshooting.

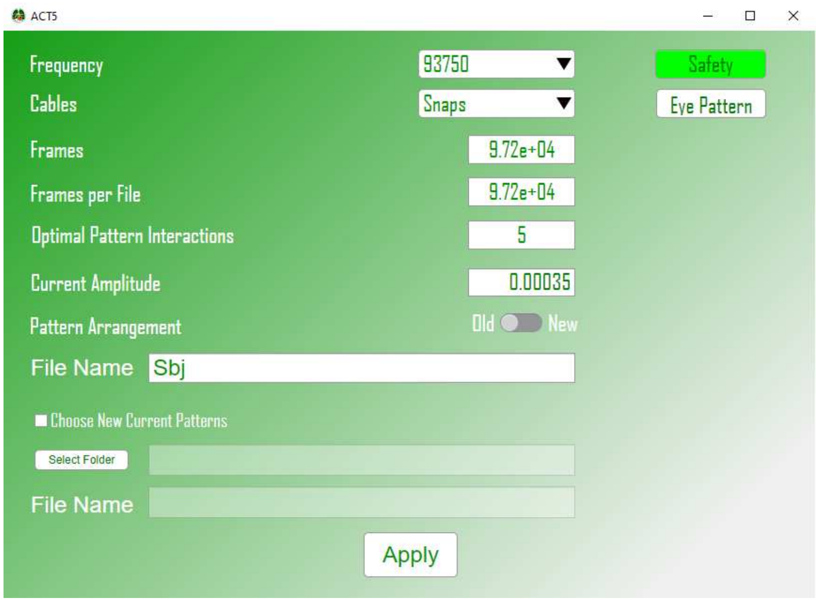

Figure 3.14: Clinical User Interface - Developer Menu Window.

3.10 EIT Imaging on Patients

Human data collection at University of Colorado Anschutz Medical Campus and Children's Hospital Colorado was in accordance with the amended Declaration of Helsinki–Ethical Principles for Medical Research Involving Human Subjects under the approval of the Colorado State University Institutional Review Board 2943, COMIRB 18-1843 and 21-3315 with written informed consent. Moreover, This project was supported by Award Number 3R01EB026710-02S1 from the National Institute Of Biomedical Imaging And Bioengineering for the ARDS study and NIH R01EB026710 for the CF study.

The ARDS data collection was performed at University of Colorado Anschutz Medical Campus in the intensice care unit using the GE GENESIS System for 3D ventilation EIT imaging while the patients were mechanically ventilated. The data were collected pre- and during spontaneous breathing test. In addition, the control groups for the ARDS study were imaged at Colorado State University.

The BPD data collection was perfomed at Children's Hospital Colorado using the ACT5 System for 2D ventilation and pulsatile perfusion EIT imaging in the Neonatal Intensive Care Unit

(NICU). The preterm infants had EIT imaging follow-ups every 3-4 weeks up to 5 visits or their discharge.

The CF and PVS data collection were also done at Children's Hospital Colorado using the ACT5 System for 3D ventilation and pulsatile perfusion EIT imaging. The data collection on CF patients were performed with EIT imaging follow-ups every 6 months. PVS patients are being imaged in the cardiac catheterization lab (Cath Lab) under mechanical ventilation pre- and post-catheterization. In addition, the control groups for the CF, BPD, and PVS studies were imaged at Children's Hospital Colorado.

EIT data for ventilation images were collected during tidal breathing while EIT data for pulsatile perfusion images were collected during breath pauses or breath holding. This is necessary since the lung ventilation changes cause the measured voltages to be more than 10 times higher than the measured voltages due to pulmonary perfusion changes. Thus, a simple approach to separate the ventilation and pulsatile perfusion signals is to use breath pauses. The small changes in voltage caused by pulmonary perfusion can only be measured by high-sensitive EIT systems with a high SNR and high-precision voltmeter such as the ACT5 system.

During short breath pauses, which can be done for less than $10\,\mathrm{s}$ by breath-holding, the changes in the measured voltages are only caused by the pulmonary perfusion. This allows an easy separation of the ventilation and perfusion signals since there is no highly accurate separation methods to extract the perfusion signals while during tidal breathing.

3.11 EIT Reconstructions and Data Collection

The first step during the EIT data collection is the electrode placement, which has to follow a pre-determined configuration so that the EIT reconstruction images are displayed in the correct orientation in the Clinical User Interface.

Figure 3.15 illustrates the electrode placement for 2D and 3D electrode configurations when using the ACT5 system. Electrode $\#1$ is placed under the subject's armpit in a counterclockwise direction in 2D configuration while in the 3D configuration, the bottom row starts with electrode

$\#1$ and the top row starts with electrode $\#17$. Both electrodes are placed under the subject's armpit following a counterclockwise direction. The ground electrode is always recommended to be placed at the subject's right trapezium.

(a) 2D electrode configuration.

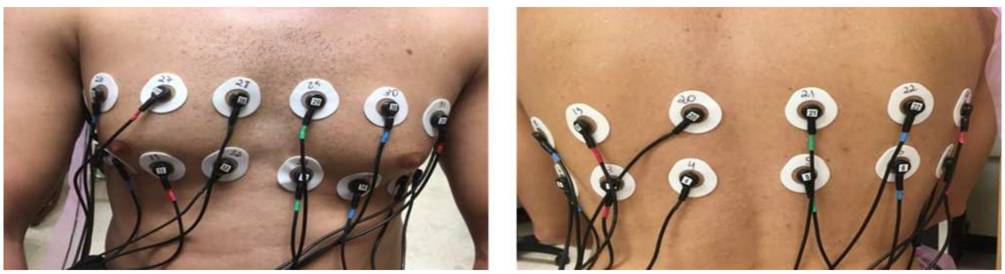

(b) 3D electrode configuration.

Figure 3.15: Electrode placements for data collection the ACT5 system.

A wearable electrode applicator textile (WEAT) belt of electrodes of the correct size is applied to the subject's torso when collecting 3D EIT data with the GE GENESIS system as shown in Figure 3.16. This belt was developed by the GE team to make electrode placement on mechanically ventilated patients easier and faster.

Using the same standard display from CT scans, The EIT images are displayed in DICOM orientation as shown in Figure 3.17, which means the right side of the subject's body will be on the left side of the display and the left side of the subject's body will be on the right. In addition, the 3D EIT image display also follows the DICOM orientation with the upper ring of electrodes as the top row and the lower ring as the bottom row.

Due to the ill-conditioning of the EIT inverse problem, and the linearization used in both NOSER and ToDLeR algorithms, absolute images are hard to obtain in human subjects. Therefore,

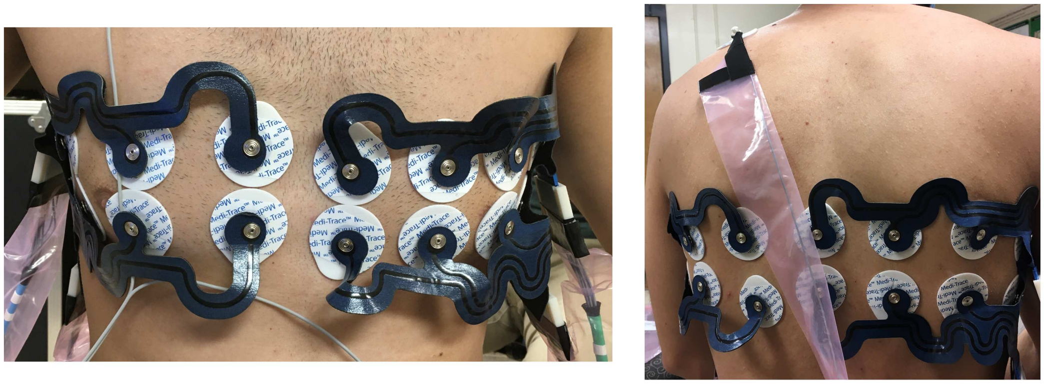

Figure 3.16: The WEAT electrode belt placement.

difference images are used to display the functional changes over time in the lungs. These images can be obtained by subtracting the reconstructed frame sequences from a single reconstructed reference frame.

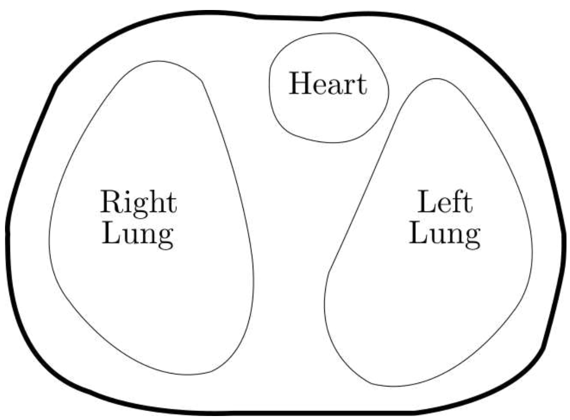

Figure 3.17: DICOM Orientation.

The reference frame can be found based on the type of reconstructions, either ventilation or pulsatile perfusion images. For ventilation images, the reference frame is chosen to be the end of expiration since the relative changes will occur due to inspiration. For pulsatile perfusion images, the reference frame is chosen to be at the end of the ECG QRS complex leading to relative changes due to systole. Using the same approach to find the reference frame when reconstructing the EIT images for multiple subjects makes it easier to analyze and compare the reconstructions.

3.12 EIT Derived-Measures

To compute EIT-derived measures, the EIT images were segmented to determine lung regions separately for the ventilation and pulsatile perfusion images. For perfusion, a cardiac voxel in the heart region was first selected manually from the image sequence. Since the pulmonary perfusion conductivity voxels are out of phase with the cardiac conductivity voxels, perfused pulmonary voxels were identified as those with low correlation with the chosen cardiac voxel.

For ventilation, the lung region was identified and segmented by a threshold method. Any voxel with a minimum relative conductivity value that remains larger than $0.5(\sigma_{aM} + \sigma_{am})$ over the entire data set was considered to be too conductive to be included as a lung voxel, where σ_{aM} and σ_{am} are the maximum and minimum values, respectively, of the conductivity over all voxels and over the entire data collection period of interest. Any voxel with maximum relative conductivity value over the entire data set exceeding 90% of σ_{aM} was also considered to be too conductive to be a lung voxel. Voxels that have peak-to-peak conductivity smaller than 30% of the highest peak-to-peak voxel conductivity, which could represent voxels with small variations close to the electrodes (such as in the upper axilla), were excluded from the computations. Finally, a lung conductivity voxel was selected manually from the respiratory image sequence and pixels highly correlated in the time domain with the chosen lung pixel were identified as being ventilated pixels. In addition, voxels in the outer four rings of the Joshua tree mesh were excluded from the segmentation for ventilation and pulsatile perfusion.

3.12.1 Global Inhomogeneity (GI) Index

The GI index is an EIT-derived measure that has been used to assess lung heterogeneity during ventilation to quantify volume distribution within the lungs [4]. The GI index can be computed by quantifying the difference between the conductivity of a voxel and the median conductivity value over the segmented lung region, and it can be described as

$$GI(\%) = \frac{\sum_{x,y \in lungs} \mid \Delta\sigma_{x,y} - median(\Delta\sigma_{lungs}) \mid}{\sum_{x,y \in lungs} \mid \Delta\sigma_{x,y} \mid} \times 100 \tag{3.67}$$

where $\Delta\sigma_{x,y}$ is a pixel in the lung region from the difference image between a frame at full inspiration and full expiration, $\Delta\sigma_{lungs}$ is all the pixels in the lung region from the difference image between a frame at full inspiration and full expiration.

3.12.2 Regional Ventilation Delay (RVD)

Regional Ventilation Delay (RVD) is a measure of how long it takes for inspired air to spread through the lungs during a breathing cycle. This is another EIT-derived measure that estimates ventilation homogeneity during inspiration. For each voxel p in the segmented lung region, using the start of inspiration from the global volume curve as the reference time point $tmin_G$, the RVD for each voxel is defined as

$$RVD(voxel) = \frac{t_{40\%} - tmin_G}{tmax_G - tmin_G} \cdot 100\%, \tag{3.68}$$

where $t_{40\%}$ is the time that the voxel volume takes to reach 40% of its maximum amplitude, and $tmax_G$ is the time that the global volume takes to reach its maximum amplitude. Figure 3.18 illustrates the calculation of the RVD for a single voxel.

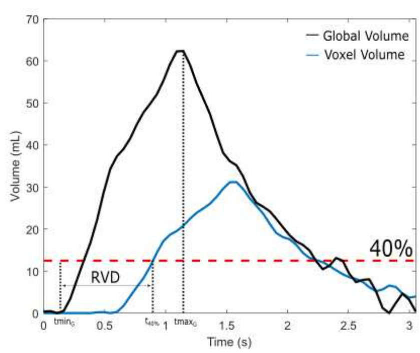

Figure 3.18: Representation of the RVD computation for a single voxel.

3.12.3 Estimation of air and blood volumes

EIT reconstructions can also be used to estimate the volumes of air and blood in the lungs during tidal breathing or breath hold. These measures can provide regional information about the volume of air delivered during mechanical ventilation and changes in blood volumes after a cardiac procedure. For each frame, the inspired volume of air in each voxel was estimated from the conductivity values in the EIT image using the method from [85] and [30].

Volume fractions are required when estimating the volumes of air and blood. For a given voxel p in the segmented lung region, let $\sigma_a(p,t)$ denote the conductivity in the pth voxel at time t corresponding to a given frame from a difference reconstruction during tidal ventilation. The volume fraction $f_a(p,t)$, of air in the pth voxel at time t, is related to the conductivity in the pth voxel at time t by

$$f_a(p,t) = \frac{\sigma_a(p,t) - \sigma_{aM}}{\sigma_{am} - \sigma_{aM}} \tag{3.69}$$

where σ_{aM} and σ_{am} are the maximum and minimum values, respectively, of the conductivity over all voxels and over the entire data collection period of interest. The volume fraction of blood $f_b(p,t)$ is computed following the same principles as the $f_a(p,t)$ and it is given by

$$f_b(p,t) = \frac{\sigma_b(p,t) - \sigma_{bm}}{\sigma_{bM} - \sigma_{bm}} \tag{3.70}$$

where $\sigma_b(p,t)$ denotes the conductivity in the pth voxel at time t corresponding to a given frame from a difference reconstruction breath hold, σ_{bM} and σ_{bm} are the maximum and minimum values, respectively, of the conductivity over all voxels and over the entire data collection period of interest.

By having the volume fractions $f_a(p,t)$ and $f_b(p,t)$, the total estimate of volume of air V_a and blood V_b in the lungs can be denoted as volume fractions multiplied by each voxel volume Vol_{voxel} which are given by

$$V_a(p,t) = f_a(p,t) \times Vol_{voxel}, \;\; V_b(p,t) = f_b(p,t) \times Vol_{voxel} \tag{3.71}$$

The volume of a voxel can be determined from the Joshua tree mesh in Fig. 3.1 and the height of the electrodes (Fig. 3.2 and 3.3). Since the Joshua tree elements have the same area, the area of all voxels are also the same. The height of the electrode is used to find an estimate of the voxel height, and it is determined based on whether it is a 2D or 3D electrode configuration.

3.12.4 Rapid Shallow Breathing Index (RSBI)

The EIT-derived Rapid Shallow Breathing Index ($RSBI_{EIT}$) can be estimated by using the global volume estimation from the EIT ventilation images and the respiratory rate (RR), and it is given by

$$RSBI_{EIT} = \frac{RR}{V_a} \tag{3.72}$$

where V_a is the tidal volume estimation from the EIT reconstructions. The $RSBI_{EIT}$ can provide information on how the patient responds to weaning maneuvers. The higher the RSBI value, the more distress the patient is experiencing due to the weaning process. Thus, the RBSI is one variable that can be used as an indicator of whether the patient can be removed from mechanical ventilation.

Chapter 4

Results and Discussion

4.1 Tank Reconstructions

Figures 4.1 and 4.2 shows the targets and tanks used for testing the 2D reconstruction algorithms. The PVC targets shown in Figure 4.1a are $2.7\,\mathrm{cm} \times 4.6\,\mathrm{cm}$ (PVC1), and $3.2\,\mathrm{cm} \times 5.4\,\mathrm{cm}$ (PVC2) while the copper targets are $2.4\,\mathrm{cm} \times 4.0\,\mathrm{cm}$ (COPPER1), and $3.1\,\mathrm{cm} \times 4.8\,\mathrm{cm}$ (COPPER2).

Both the 2D circular, Figure 4.1b, and chest-shaped, Figure 4.1c, tanks have 32 electrodes with size $2.54\,\mathrm{cm} \times 2.54\,\mathrm{cm}$. The 2D circular tank has a $15\,\mathrm{cm}$ radius while the The 2D chest-shaped tank has a $107\,\mathrm{cm}$ circumference.

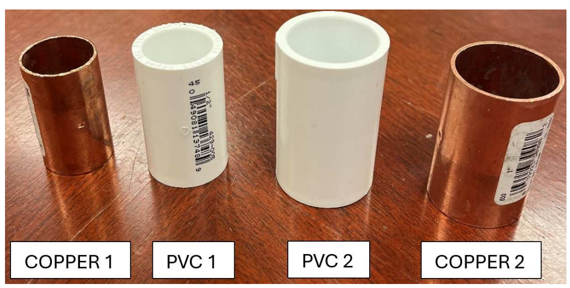

(a) PVC and copper targets.

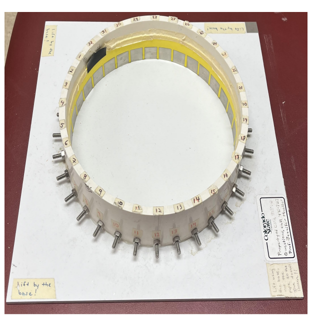

(b) 2D circular tank.

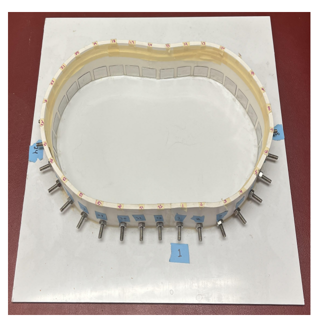

(c) 2D chest-shaped tank.

Figure 4.1: (a) PVC and Copper targets used on 2D tanks. (b) 2D circular tank. (c) 2D chest-shaped tank.

Figure 4.2a shows the targets used when doing the measurements on the 3D tank, Figure 4.2b. Both the insulator and the stainless steel spherical targets have $1\,\mathrm{cm}$ radius. The height from the bottom of the tank to the center of the lower row of electrodes is $7.7\,\mathrm{cm}$, and the height from the bottom of the tank to the center of the upper row of electrodes is $11\,\mathrm{cm}$. The 3D tank has 64 electrodes, $2.54\,\mathrm{cm} \times 2.54\,\mathrm{cm}$ each. The 3D tank was arranged in 2×32 rows by connecting a jumper cable for each two electrodes, and for the reconstructions, the electrode size was considered to be sum of both electrodes together as $5.08\,\mathrm{cm} \times 2.54\,\mathrm{cm}$. The vertical gap is $V_{GAP} = 3.1\,\mathrm{cm}$ from center-to-center of the electrodes.

(a) Targets.

(b) 3D cylindrical tank.

Figure 4.2: (a) Insulator and Stainless steel targets used on the 3D tank. (b) 3D cylindrical tank.

4.1.1 2D Tank Reconstructions

Figures 4.3-4.8 show the NOSER and ToDLeR conductivity and susceptivity, ($\omega\varepsilon$, where ω is the angular frequency and ε is the electric permittivity), difference reconstructions on the 2D circular tank using the ACT5 System, and the target configurations.

The applied current amplitude was $0.35\,\mathrm{mA}$ at $93.750\,\mathrm{kHz}$, and the saline solution was $340\,\mathrm{mS}$ measured by a conductivity meter with the saline height being the same as the electrode height, $2.54\,\mathrm{cm}$. The reference frame was chosen to be the average of 1600 frames with no targets in the tank. In addition, 1600 frames were also averaged for each target configuration.

Both the NOSER and ToDLeR 2D reconstructions have similar conductivity images and σ_{best} values. The σ_{best} for NOSER is $393.3\,\mathrm{mS}$ and the σ_{best} for ToDLeR is $383.5\,\mathrm{mS}$ when there is only saline solution in the tank. Both are slightly higher than the saline solution $340\,\mathrm{mS}$ due to the 32-electrode contact with the saline solution which is not accounted for in the forward problem.

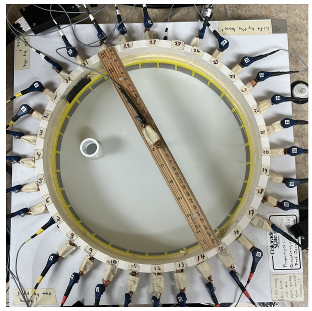

(a) Target Placement.

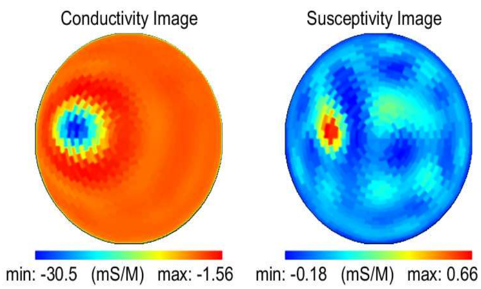

(b) NOSER reconstructions.

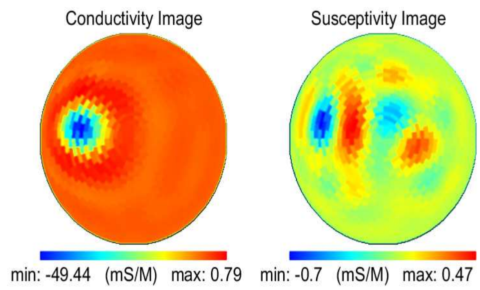

(c) ToDLeR reconstructions.

Figure 4.3: Comparison of NOSER and ToDLeR reconstructions using the PVC1 pipe target. (a) PVC Target placed in the tank. (b) NOSER Reconstruction. (b) ToDLeR reconstruction.

The Gap and AVG-Gap Models do not account for electrode contact impedance. This can only be done by the Complete Model [86], which is not discussed in this dissertation. However, both σ_{best} values are close to the expected $340\,\mathrm{mS}$, which shows that the forward solutions in eq. 3.25 and 3.46 are good approximations to the 2D circular tank problem.

The conductivity images show a lower conductivity, blue color, where the PVC targets are placed and higher conductivity, red color, where the copper targets are placed, which means that the PVC target is less conductive than the saline solution while the copper target is more conductive. In terms of spatial resolution, there is no visual difference between the PVC1 and PVC2 conductivity images (Figures 4.3 and 4.4), and the COPPER1 and COPPER2 conductivity images (Figures 4.5 and 4.6), despite the conductivity PVC2 and COPPER2 images having a higher range because of

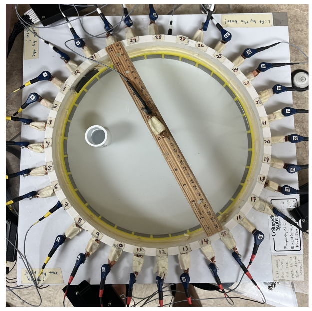

(a) Target Placement.

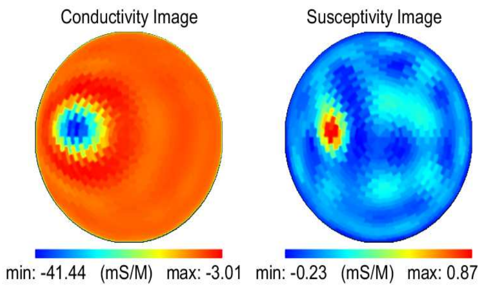

(b) NOSER reconstructions.

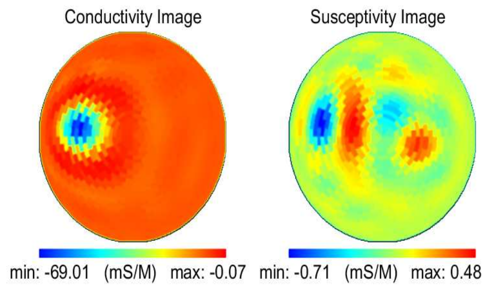

(c) ToDLeR reconstructions.

Figure 4.4: Comparison of NOSER and ToDLeR reconstructions using the PVC2 pipe target.(a) PVC Target placed in the tank. (b) NOSER Reconstruction. (b) ToDLeR reconstruction.

the target sizes. This can happen due to the ill-posed EIT problem and smoothing effects related to regularization. The regularization parameters for the reconstructions are $\alpha = 0.01$ for NOSER algorithm and $\alpha_1 = 0.005$, $\alpha_2 = 0.001 \times 10^{-4}$ for ToDLeR algorithm.

When the PVC and copper targets are placed at the same time in the tank, we can see there is a good contrast between them, shown in Figure 4.7. Moreover, when the PVC and copper are placed about $2.5\,\mathrm{cm}$ apart (Figure 4.8), there is still a good contrast between the targets in the conductivity images.

The NOSER and ToDLeR reconstructions shows different susceptivity images in all target arrangements, which is an effect that we are still investigating and trying to understand and explain. We can see that both PVC and copper targets appear with less susceptivity, blue color, than the saline, which is zero, in the ToDLeR reconstructions. Conversely, the NOSER susceptivity images show higher susceptivity, red color, for both PVC and copper targets. One would expect that the susceptivity of the PVC and copper pipes is higher than the background [14], which can be

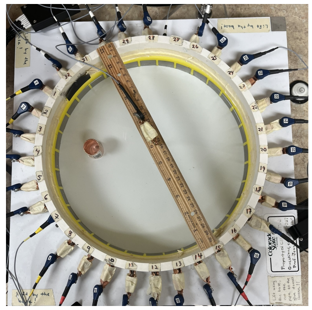

(a) Target Placement.

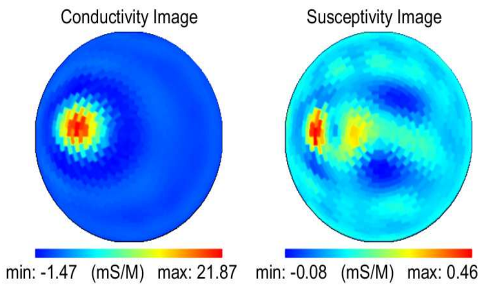

(b) NOSER reconstructions.

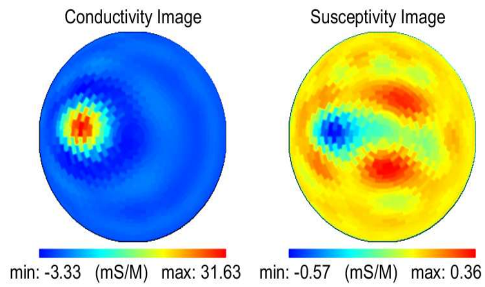

(c) ToDLeR reconstructions.

Figure 4.5: Comparison of NOSER and ToDLeR reconstructions using the Copper1 pipe target. (a) Copper target placed in the tank. (b) NOSER Reconstruction. (b) ToDLeR reconstruction.

seen in the NOSER susceptivity image, but it is the opposite in the ToDLeR susceptivity image. Another explanation is that the algorithms use different approaches to solve the inverse problem, and different regularization strategies.

The differences that occur in the NOSER and ToDLeR reconstructions could be related to the frequency dependence of the susceptivity. The PVC target becomes more capacitive as the frequency increases, and the copper targets more inductive, and at $93.750\,\mathrm{kHz}$ operation frequency, is when these changes start to become more distinguished [14]. Thus, since the operation frequency is around the threshold frequency for the reactive component changes in the PVC and copper targets, the NOSER algorithm may be picking up the susceptivity as above the threshold while the ToDLeR algorithm below the threshold.

Since the susceptivity images are either showing higher susceptivity (NOSER) or lower susceptivity (ToDLeR) for the PVC and copper targets, the contrast shown in the conductivity images (Figure 4.7) when the PVC and copper target are placed $2.5\,\mathrm{cm}$ apart is reduced in the susceptivity images. We can see that both targets appear as one single target in NOSER and ToDLeR reconstructions (Figure 4.7). Thus, this shows that the conductivity and susceptivity images give different results based on the property of the targets.

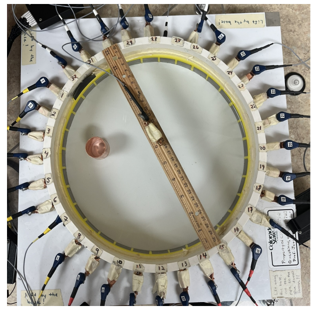

(a) Target Placement.

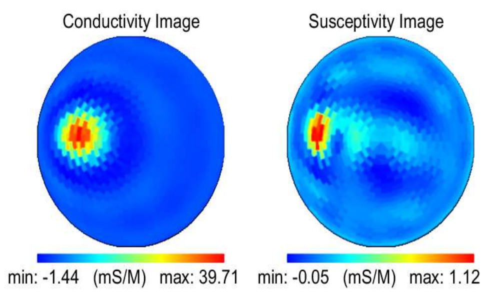

(b) NOSER reconstructions.

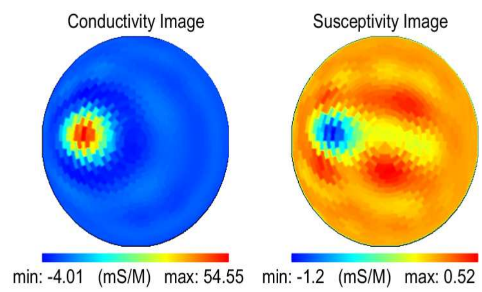

(c) ToDLeR reconstructions.

Figure 4.6: Comparison of NOSER and ToDLeR reconstructions using the Copper2 pipe target. (a) Copper Target placed in the tank. (b) NOSER Reconstruction. (b) ToDLeR reconstruction.

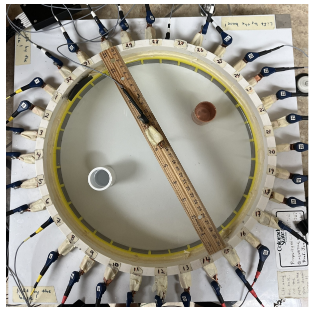

(a) Target Placement.

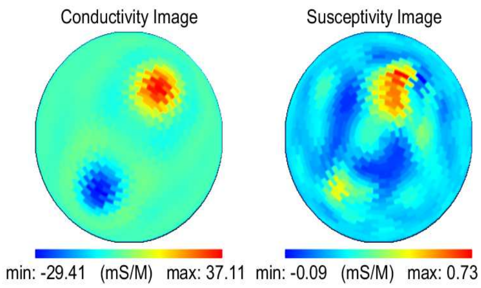

(b) NOSER reconstructions.

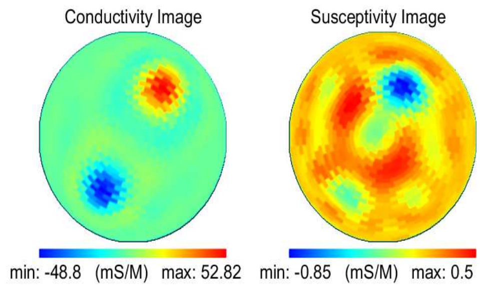

(c) ToDLeR reconstructions.

Figure 4.7: Comparison of NOSER and ToDLeR reconstructions using PVC1 and Copper2 targets placed opposite from each other. (a) Targets placed in the tank. (b) NOSER Reconstruction. (b) ToDLeR reconstruction.

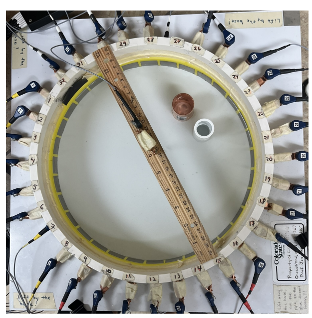

(a) Target Placement.

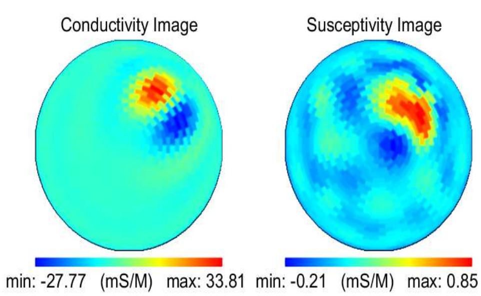

(b) NOSER reconstructions.

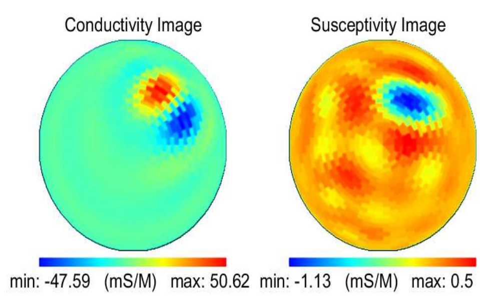

(c) ToDLeR reconstructions.

Figure 4.8: Comparison of NOSER and ToDLeR reconstructions using PVC1 and Copper2 targets placed close to each other. (a) Targets placed in the tank. (b) NOSER Reconstruction. (b) ToDLeR reconstruction.

Out-of-plane Current Effects

Since the ToDLeR algorithm can account for different saline level heights while NOSER assumes that the saline level height is the same as the electrode height, $1000\,\mathrm{mL}$ of saline was added to the tank, increasing the saline level height by approximately $1.41\,\mathrm{cm}$ above the level of the electrodes, and keeping its conductivity at $340\,\mathrm{mS}$. This experiment was performed to evaluate differences in the EIT reconstructions and forward problems due to out-of-plane current effects due to a higher saline level that is not accounted for in the NOSER algorithm , but it is modeled in the ToDLeR algorithm by considering the total the saline level height.

The NOSER and ToDLeR reconstructions from the PVC and copper targets shown in Figures 4.9 and 4.10, respectively, do not show any visual spatial difference in the target reconstructions. However, the ToDLeR σ_{best} is $376.7\,\mathrm{mS}$ while the NOSER σ_{best} is $548.1\,\mathrm{mS}$ for only saline solution without any targets in the tank. This shows that the ToDLeR forward solver can account for the out-of-plane current effects better than NOSER because the ToDLeR model considers the full saline level while NOSER only considers what is in the same level of the electrodes. Therefore, the extra saline that is out-of-electrode-plane is seen as a parallel impedance by the NOSER algorithm.

Although this effect does not seem to make any difference for the inverse problem reconstructions when comparing the NOSER and ToDLeR algorithms, this may not be the case when doing reconstructions on human subjects where the out-of-plane current effects are more pronounced due to the differences in tissue impedance.

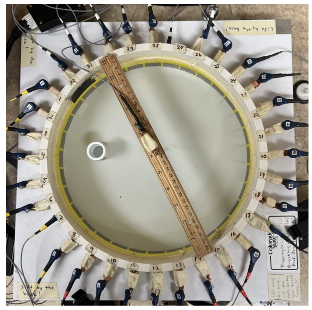

(a) Target Placement.

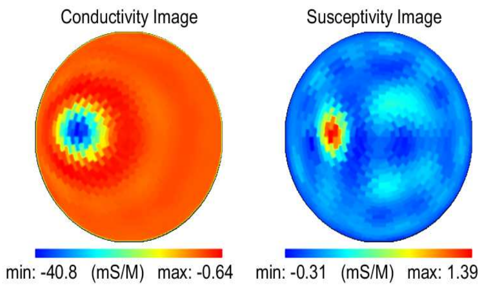

(b) NOSER reconstructions.

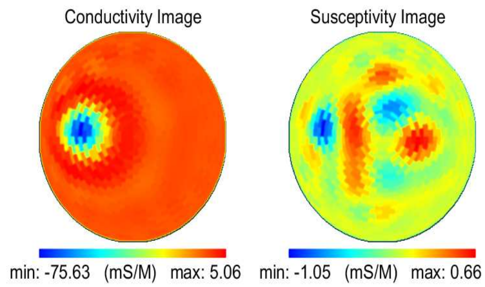

(c) ToDLeR reconstructions.

Figure 4.9: Comparison of NOSER and ToDLeR reconstructions using the PVC1 pipe target with a high water volume. (a) PVC target placed in the tank. (b) NOSER Reconstruction. (b) ToDLeR reconstruction.

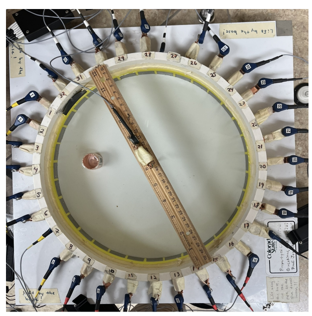

(a) Target Placement.

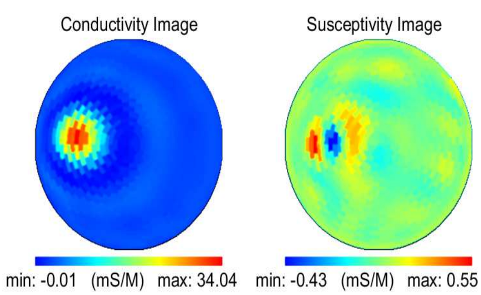

(b) NOSER reconstructions.

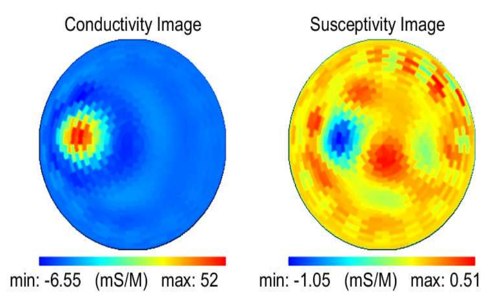

(c) ToDLeR reconstructions.

Figure 4.10: Comparison of NOSER and ToDLeR reconstructions using the Copper1 pipe target with a high water volume. (a) Copper target placed in the tank. (b) NOSER Reconstruction. (b) ToDLeR reconstruction.

4.1.2 2D Chest-Shaped Tank Reconstructions

Both NOSER and ToDLeR reconstructions assume circular or cylindrical models when solving the forward and inverse problems. The main disadvantage of these approaches is not accounting for the actual human chest shape.

Although the conformal map does not change the NOSER and ToDLeR solutions, it can provide a better display of the reconstructions using a chest-shaped display. To test the positioning of the targets after using the conformal map, a chest-shaped tank was used with saline solution $340\,\mathrm{mS}$ and saline level height the same as the electrode height, $2.54\,\mathrm{cm}$. The applied current amplitude was $0.35\,\mathrm{mA}$ at $93.750\,\mathrm{kHz}$, and the reference frame was chosen to be the average of 1600 frames with no targets in the tank and 1600 frames were also averaged for the target configuration.

Figures 4.11 and 4.12 show the NOSER and ToDLeR reconstructions, respectively, on a circular domain and chest shape domain with the PVC and copper targets. We can see that the NOSER conductivity and susceptivity, and ToDLeR conductivity and susceptivity images are a much better representation of the actual 2D chest-shaped tank.

This shows that despite the fact that both reconstruction algorithms consider circular or cylindrical models, the conformal map provides a realistic display for the NOSER and ToDLeR reconstructions, which will be used for displaying the human subject EIT reconstructions. Moreover, the conformal map can be pre-computed before doing the reconstructions, which means that it does not affect the real-time reconstructions as long as the display matrix has about the same number of pixels.

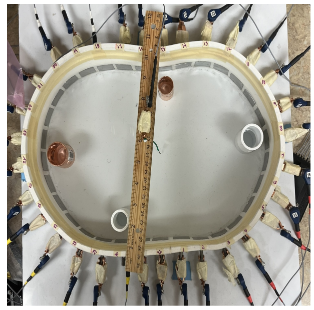

(a) Target Placement.

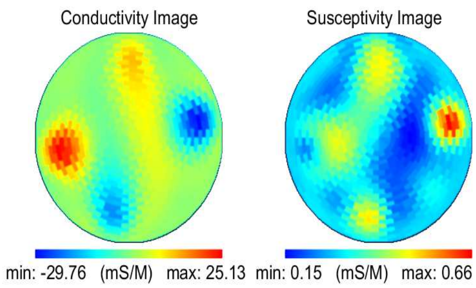

(b) Circular Domain.

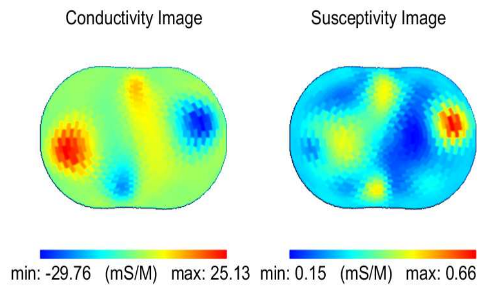

(c) Chest-Shaped Domain.

Figure 4.11: NOSER reconstructions on a 2D chest-shaped tank. (a) All targets placed in the tank. (b) NOSER Reconstruction display on a circle domain. (c) NOSER Reconstruction display on a chest-shaped domain.

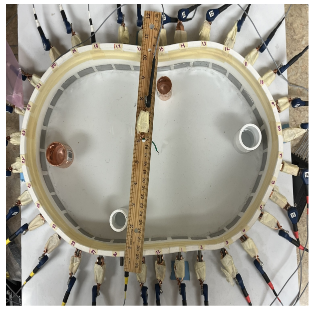

(a) Target Placement.

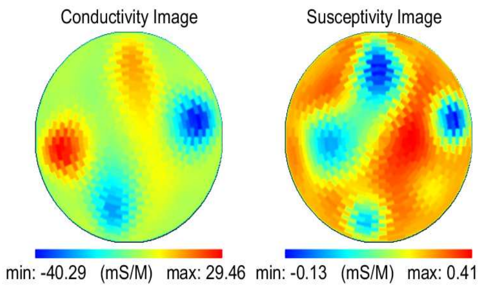

(b) Circular Domain.

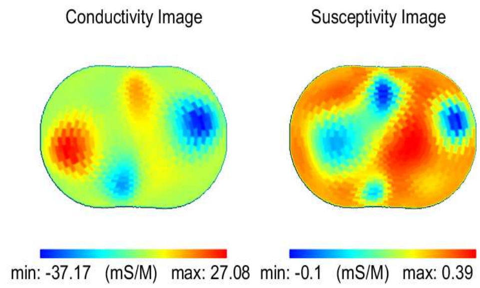

(c) Chest-Shaped Domain.

Figure 4.12: ToDLeR reconstructions on a 2D chest-shaped tank. (a) All targets ToDLeR in the tank. (b) ToDLeR Reconstruction display on a circle domain. (c) ToDLeR Reconstruction display on a chest-shaped domain.

4.1.3 3D Tank Reconstructions

The ToDLeR algorithm was also tested on a 3D cylindrical tank. The applied current amplitude was $0.35\,\mathrm{mA}$ at $93.750\,\mathrm{kHz}$, and the saline solution was $340\,\mathrm{mS}$ with the saline level height of $18.2\,\mathrm{cm}$. The reference frame was chosen to be the average of 1600 frames with no targets in the tank. In addition, 50 frames were also averaged for each reconstruction as the target is moved in the 3D cylindrical tank. Since 2 rows of 16 electrodes are used in human subject data collection, pairs of electrodes were connected together to reduce the 2×32 to $2x16$ rows of electrodes on the 3D tank. Moreover, since the water body is too high due to the 3D tank size and the ground connection is small when touching the water, the data collected on the 3D tank was noisier than the ones collected on the 2D tank. Thus, a low pass filter was used to filter the voltages before doing the reconstructions.

Figure 4.13 shows the $Re(\sigma_{best})$ curve and three different time ranges (T0 - red color, T1 - blue color, T2 - green color) representing each average reconstruction as the stainless steel target moves from the top of the tank ($18.5\,\mathrm{cm}$) to the electrode plane ($\approx 10\,\mathrm{cm}$) close to electrodes number 14 and 30. The $Re(\sigma_{best})$ curve is used in this case to track the position of the target as it moves since as it gets closer to the electrode plane, the $Re(\sigma_{best})$ will increase because the medium is becoming more conductive. In addition, we can see that the $Re(\sigma_{best})$ considering only the saline solution is $466.6\,\mathrm{mS}$ when compared to the measured conductivity $340\,\mathrm{mS}$ from saline solutions. The higher value is caused by the number of electrodes in contact with the saline solution, which in this case is 64 electrodes.

At T0, the target is barely submerged, which does not show up on the bottom row, and a minimal effect can be seen on the top row in the conductivity image. At T1, the target can be seen on the top row and a minimal effect can be seen on the bottom row in the conductivity image. At T3, the target is between both plane of electrodes, and it can be seen in both top and bottom conductivity images. Conversely, we can not see much changes occurring on the susceptivity image since the stainless steel has a very small reactive component.

The same experiment was repeated with results shown in Figure 4.14, but this time an insulator was used as target. Since the insulator has lower conductivity than the background, the $Re(\sigma_{best})$ curve decreases as the target gets closer to the electrode plane ($\approx 10\,\mathrm{cm}$) close to electrodes number 14 and 30. The same effects are observed at T0, T1, and T2 conductivity images, but the insulator shows as low conductivity region (blue color) as it moves towards the electrode plane. Moreover, the susceptivity images also shows minimal changes since the insulator has a small reactive component.

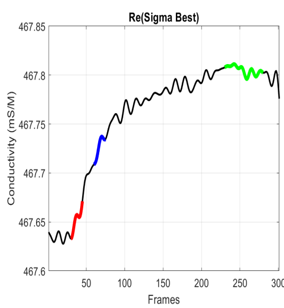

(a) $Re(sigma_{best})$ curve.

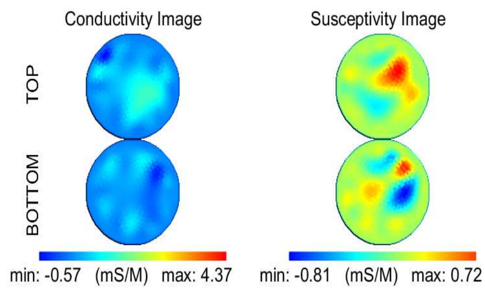

(b) T0 - average of frames in red.

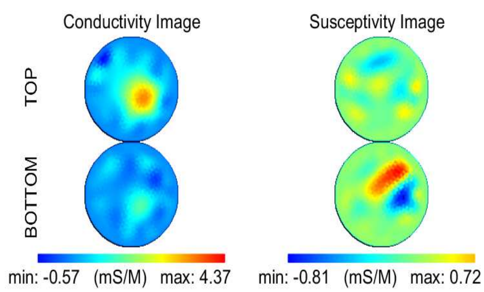

(c) T1 - average of frames in blue.

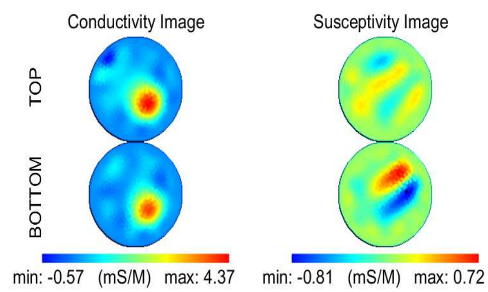

(d) T2 - average of frames in green.

Figure 4.13: ToDLeR reconstructions on a 3D tank using the stainless steel target. (a) Real part of sigma best (σ_{best}), and the time range for each reconstruction is represented in red, blue, and green colors. (b) Reconstruction in the red time range (T0). (c) Reconstruction in the blue time range (T1). (d) Reconstruction in the green time range (T2).

The reconstructions of the insulator and stainless steel targets show that objects close to the water height will not show up on the images, and the out-of-plane effects are minimized by adding more row of electrodes since the objects have to be much closer to the electrode plane to be seen on both reconstruction planes.

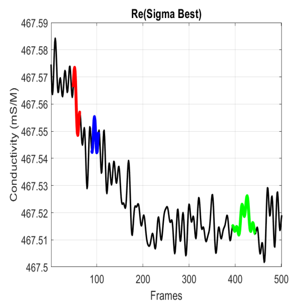

(a) $Re(sigma_{best})$ curve.

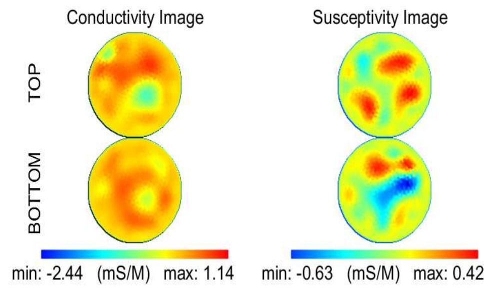

(b) T0 - average of frames in red.

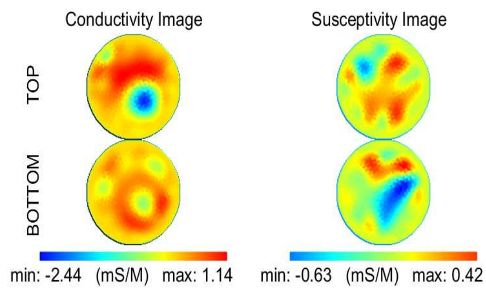

(c) T1 - average of frames in blue.

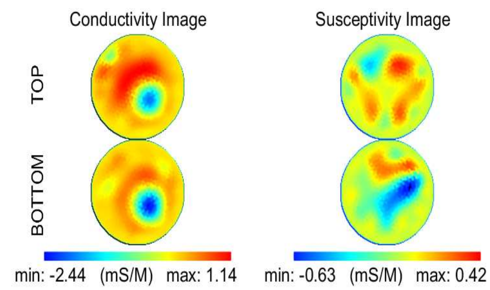

(d) T2 - average of frames in green.

Figure 4.14: ToDLeR reconstructions on a 3D tank using the insulator target. (a) Real part of sigma best (σ_{best}), and the time range for each reconstruction is represented in red, blue, and green colors. (b) Average reconstruction at the red time range (T0). (c) Average reconstruction at the blue time range (T1). (d) Average reconstruction at the green time range (T2).

4.2 ECG Filtering Algorithm

To evaluate the ECG filtering algorithm, data were collected using the ACT5 system on a 35-year-old healthy male subject having a body mass index (BMI) of $28.4\ \mathrm{kg/m^2}$ and a chest circumference of $100.3\ \mathrm{cm}$. The subject was laying in the supine position with 2 rows of 16 electrodes attached around his thorax with the top row placed above the nipple line and the bottom row below the nipple line, and with the approximation for the lead II electrocardiogram taken to be the voltage difference between electrodes 16 and 25 as seen in Figure 4.15.

In a standard ECG electrode placement, the lead II measurement is taken from electrodes placed in the right arm and below the torso or left leg. Therefore, electrodes 16 and 25 are the closest in positions to estimate the lead II ECG from the 3D EIT electrode placement.

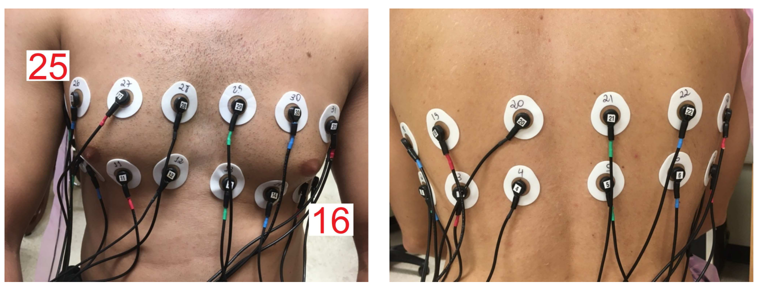

Figure 4.15: 2x16 electrode arrangement. The estimate for lead II electrocardiogram is taken to be the voltage difference between electrodes 16 and 25. Electrode 25 is in the upper ring below the subject's right arm and electrode 16 is in the lower ring on the left side of the torso.

First, ECG data was collected without applying EIT to evaluate the filter algorithm. We implemented adaptive filters to remove each interfering frequency that was identified by Fourier analysis with $\mu = 0.001$, $A_c = 1$, $f_k = f_{\text{FR}}k$, with $k = \{1, ..., 11\}$. In addition, due to USA power line interference, we included the first five harmonics of $60\ \mathrm{Hz}$ in the adaptive filter stage, with $f_k = 60k$ and $k = \{1, ..., 5\}$. Thus, nineteen harmonic frequencies are attenuated using the adaptive filter. Moreover, for the low-pass filter stage, we implemented the Butterworth filter of order 40 with the cutoff frequency of $150\ \mathrm{Hz}$ using the `filtfilt` toolbox.

For the EIT signal, trigonometric current patterns with amplitude $0.35\,\mathrm{mA}$ and frequency of $93.750\,\mathrm{kHz}$ were used when the subject was tidal breathing and breath-holding to compare with the ECG measurements for when EIT current patterns were not applied.

Figure 4.16a shows the comparison between the raw and filtered ECG signals for lead II without applying EIT current patterns. The top image shows the raw ECG signal and its harmonic components. We can see the powerline $60\,\mathrm{Hz}$ frequency interference present in the FFT plot. The middle image illustrates the filtered ECG with an attenuated $60\,\mathrm{Hz}$ interference in the FFT plot while the bottom image shows both raw and filtered ECG displayed on the same plot which shows that the filter stage is targeting the interfering harmonic frequencies with minimal signal attenuation and without delaying the ECG signal.

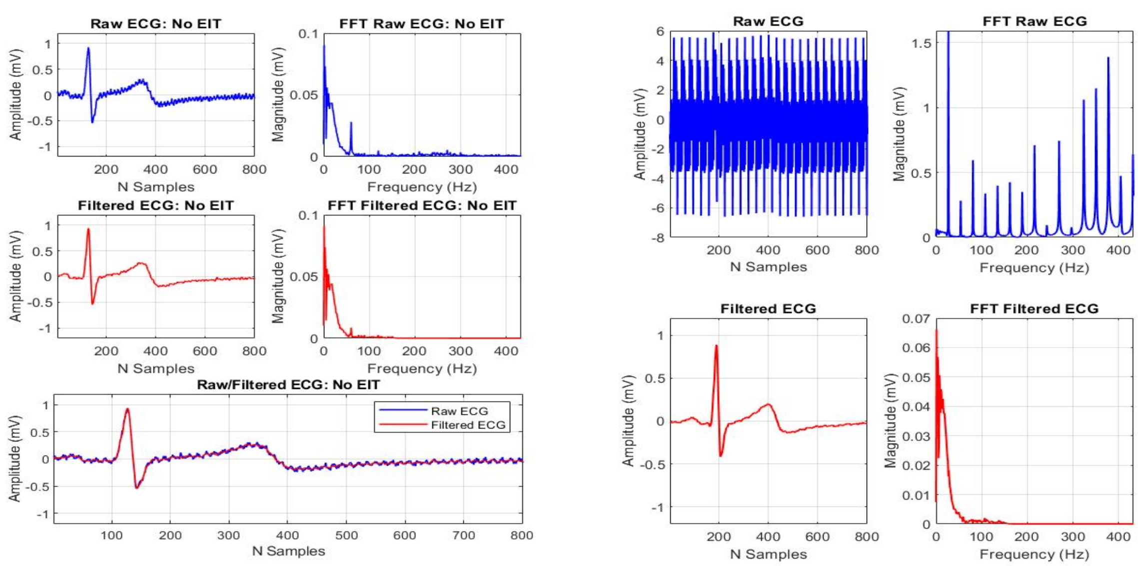

(a) Without EIT current patterns being applied. **(b)** With EIT current patterns being applied.

Figure 4.16: (a) Comparison between Raw and Filtered ECG signals without applying EIT current patterns. (b) Comparison between Raw and Filtered ECG signals while applying EIT current pattern.

Figure 4.16b shows the comparison between the raw and filtered ECG signals when applying EIT current patterns. The top image shows the raw ECG signal and its harmonic components, including the interfering frequencies from EIT and powerline. The bottom image shows the ECG signal and its harmonics after the adaptive and low-pass filter stages. This demonstrates that the filter stage is suppressing the interfering frequencies effectively, resulting in a clean ECG signal.

The ECG filter algorithm was also evaluated on a patient aged 7 year-old with diagnosed right bundle branch block, which blocks or delays the cardiac signals. Figure 4.17 shows the patient's ECG report taken by the hospital's ECG machine and the ECG measurement taken by the ACT5 system. We can see that the lead II ECG traces are very similar between the two ECG measurements with differences being caused by the lead II electrode position. This shows that the ECG filter algorithm can produce accurate filtered ECG results when compared to standard ECG measurements.

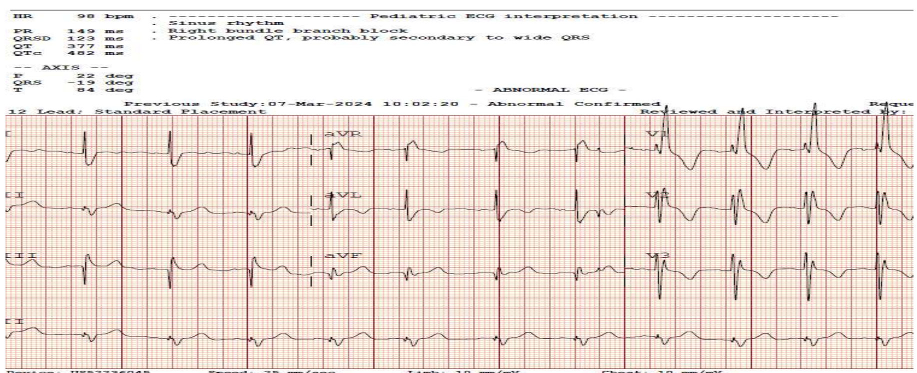

(a) Patient's ECG report.

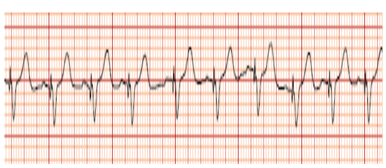

(b) Lead II ECG measurement with hospital's ECG machine.

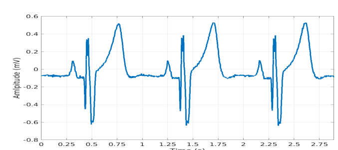

(c) Lead II ECG measurement with the ACT5 system.

Figure 4.17: Comparison of ECG measurements with the hospital's ECG machine and the ACT5 system.

The main disadvantage of the Adaptive LMS filter is the adaptation time. It takes about 7 s for the filter to converge, which makes the ECG signal close to the beginning of the data collection not usable. This can be shortened by increasing the μ step-size, but it will cause distortions on the ECG signal, leading to inaccurate ECG signals.

4.3 Examples of Ventilation and Perfusion Images

EIT has high temporal resolution which allows us to reconstruct several frames from a ventilation and perfusion sequence. For each reconstruction that is shown in the following sections, videos were made with the full frame sequence of reconstructions, but only time snapshots are displayed as the results in this dissertation.

For pulsatile perfusion reconstructions, frames corresponding to systole and diastole can be determined from the ECG. Figure 4.18 shows an ECG signal from a healthy subject where each red mark represents an EIT frame. The ECG signal is measured while each EIT current pattern is applied.

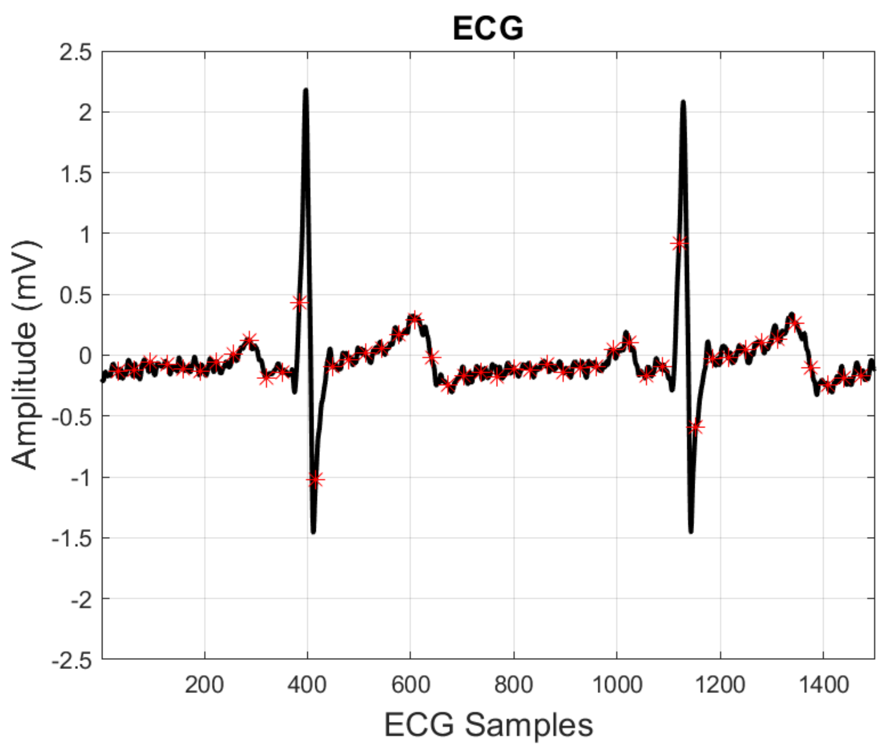

Figure 4.18: ECG signal from a healthy subject used to find the reference frame. Red marks correspond to an EIT frame.

Since we usually apply 16 or 32 current patterns, which includes the $L-1$ number of patterns plus a constant DC pattern for ground current measurements, the EIT frame represents the data between two red marks on the ECG signal plot. Thus, to find the corresponding EIT frame based on the ECG signal, we need to divide the ECG sample number by 16 or 32, depending on the number of current patterns applied, since there are more ECG measurements than EIT measurements.

Figure 4.19 shows a ToDLeR perfusion reconstruction over a period of time from a healthy subject during breath-holding. The upper image is the reconstruction through the upper plane of electrodes and the lower image is the reconstruction through the lower plane of electrodes.

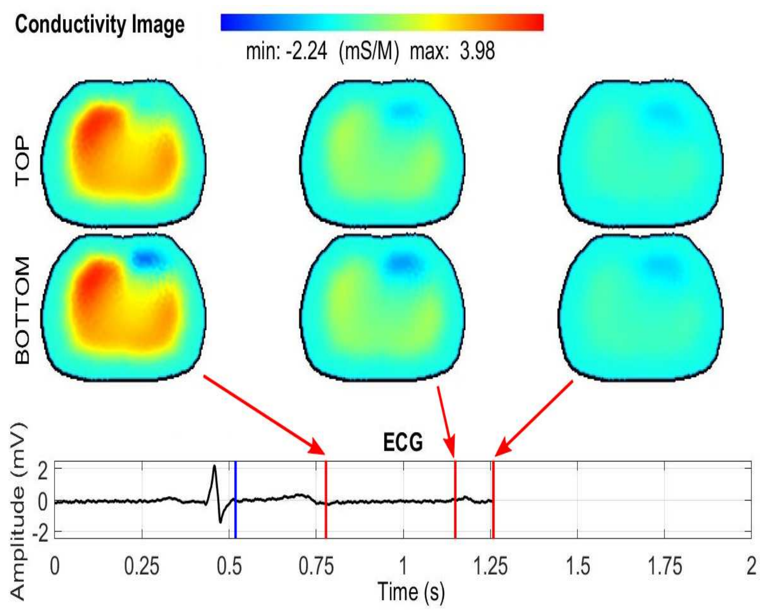

Figure 4.19: 3D perfusion reconstruction on a healthy subject.

The blue vertical line on the ECG plot indicates the EIT reference frame, which is at the end of the S-wave, corresponding to the end of diastole. The red vertical lines at the end of T-wave, beginning of P-wave, and beginning of Q-wave, indicates each EIT reconstruction image time. Choosing a reference at the end of diastole means that during systole, the lung region will have red color because of the movement of blood into the lungs while the heart region will have blue color since the blood is leaving the heart to the pulmonary and systemic circulation.

The peak of systole occurs at the end of the T-wave, and we can see on the conductivity images that is the time where the lung regions have the highest conductivity (red color), and the heart region the lowest conductivity (blue color). As the time advances in the cardiac cycle, the heart becomes more conductive and the lungs less conductive represented by the reconstructions at the beginning of the P-wave. Then, reconstructions closer to the end of the S-wave will barely show any changes since it is close to the reference frame.

Figure 4.20 shows the $Re(\sigma_{best})$ curve. For ventilation reconstructions, the $Re(\sigma_{best})$ curve gives information about the ventilation changes in the lungs and when the full-inspiration and full-expiration time occurs. At full-inspiration (blue marks), the lung regions become less conductive because of a higher volume of air in the lungs while at full-expiration (red marks), the lung regions become more conductive due to less volume of air.

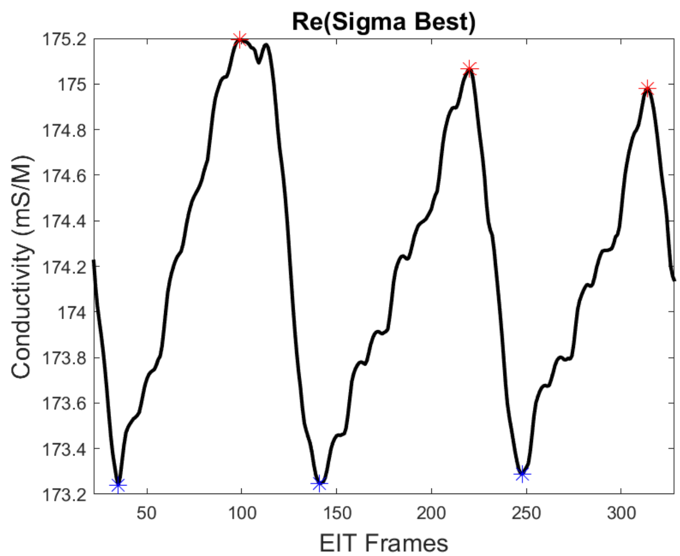

Figure 4.20: Sigma best (σ_{best}) ventilation curve used to find the reference frame. Red marks correspond to the end of expiration frames and blue marks correspond to the end of inspiration frames.

Figure 4.21 show the ventilation reconstructions of a ventilatory time sequence. The blue vertical line corresponds to the reference frame at full-expiration while the red vertical lines corresponds to full-expiration, middle of inspiration, and at full inspiration. As the lungs have more air volume during inspiration, the lungs regions in the conductivity images become more blue, representing areas of low conductivity. At full-inspiration, it is the moment where the lung regions show the lowest conductivity values due to the high volume of air.

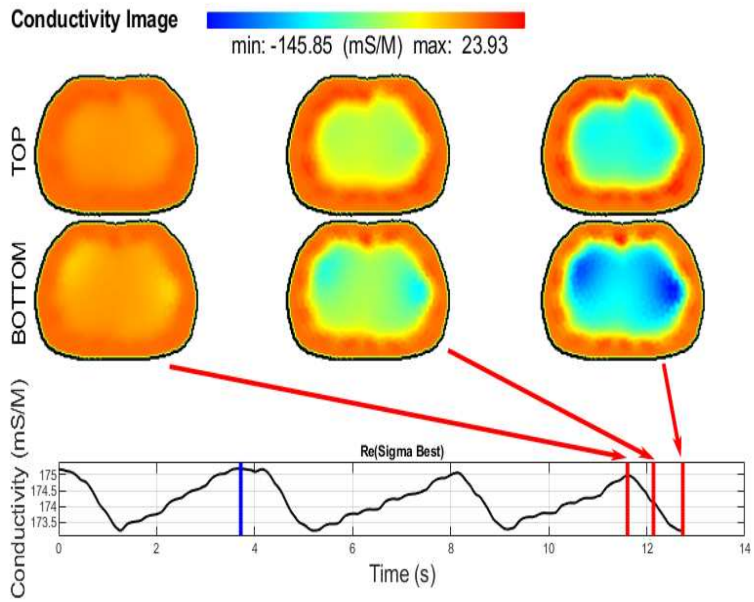

Figure 4.21: 3D ventilation reconstruction on a healthy subject.

For convention, in the next sections, the perfusion images will be shown at the end of T-wave with reference frame at the end of S-wave while the ventilation images will be shown at full-inspiration with reference frame at full-expiration.

To compute EIT-derived measures, both ventilation and pulsatile perfusion reconstructions must be segmented. Figure 4.22 shows examples of ventilation and pulsatile perfusion images segmented with the lung regions. The areas in blue correspond to aerated lung regions which are used to compute the EIT-derived measures from the ventilation reconstructions. The areas in red correspond to the amount blood presence in the lungs from the pulsatile perfusion reconstructions. Moreover, to better understand how disease affects different regions of the lungs, the lung regions are separated as upper right (UR), upper left (UL), lower right (LR), and lower left (LL).

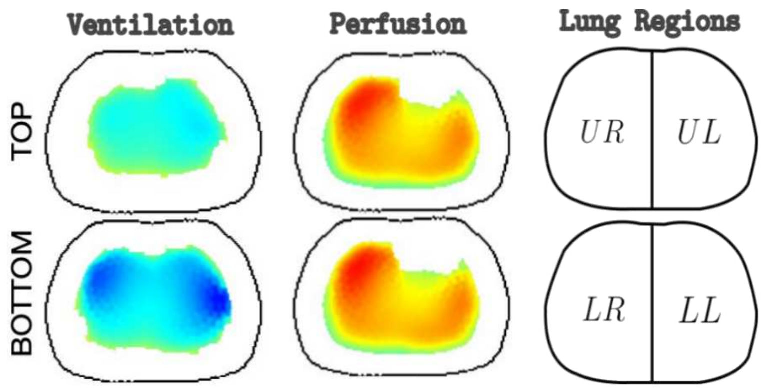

Figure 4.22: Ventilation and perfusion segmented images and lung region definitions.

4.4 EIT Reconstructions of preterm babies

This section shows the ventilation and pulsatile perfusion images from a subset of five healthy control babies with gestational age $(37.1, \pm 3.6)$ weeks and chronological age $(46.7, \pm 40.9)$ days, and patients with BPD with gestational age $(31.2, \pm 1.0)$ weeks and chronological age $(33.8, \pm 21.2)$ days during the first visit using the NOSER and ToDLeR algorithms, and the ACT5 system. The data were collected at Children's Hospital Colorado in the Neonatal Intensive Care Unit (NICU).

Sixteen electrodes were placed around each baby's torso (Figure 4.23) and trigonometric current patterns with amplitude $0.35\,\mathrm{mA}$ and frequency of $93.750\,\mathrm{kHz}$ were applied during the data collection. Since we are using 16 electrodes, the frame rate was doubled to $54\,\mathrm{frames/sec}$. Moreover, the ventilation reconstructions were performed from tidal breathing while the perfusion reconstructions were performed during the baby's breathing pauses or extracted from long expiration time sequence.

4.4.1 NOSER Ventilation Reconstructions

Figures 4.24-4.26 show the NOSER ventilation reconstruction snapshots at full inspiration with reference frame at full expiration from the control babies and babies with BPD, which are displayed in numbering order. We can see that the control conductivity and susceptivity images of the controls show more aerated region than the BPD conductivity and susceptivity images, which

Figure 4.23: Single row of 16 electrodes placed on a baby with BPD.

could be caused by the age difference between the controls and infants with BPD. However, we can see that the BPD patient 2 and 3 only show more ventilation changes towards the left lung.

The radiology report from visit 1 for BPD patient 2 says that *("Similar mild lung hyperexpansion. Diffuse granular and interstitial opacities appear slightly decreased. Mild streaky opacity in the right upper lobe, likely atelectasis.").* Thus, we can see that the BPD patient 2 reconstructions are in accordance with the radiology report since the right lung does not show much changes dues to ventilation.

The radiology report from visit 1 for BPD patient 3 says that *("Lung volumes are normal. Interstitial opacities are slightly worsened. Small bilateral effusions are similar. The heart is normal in size. No Pneumothorax.").* In this case, the report does not say anything about the right/left lung condition besides that the interstitial opacities are slightly worsened. However, we can still see that the both lungs are not fully open, which can indicate the effect of the interstitial opacities.

BPD patients 1 and 5 also have interstitial opacities according to the radiology, but it does not seem to cause more changes in the NOSER ventilation reconstructions when compared to the controls. Moreover, BPD patient 4 has an improved bilateral linear upper lobe atelectasis.

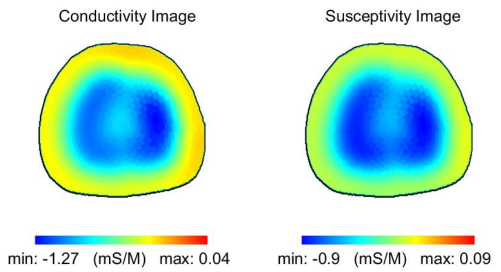

(a) Control 1.

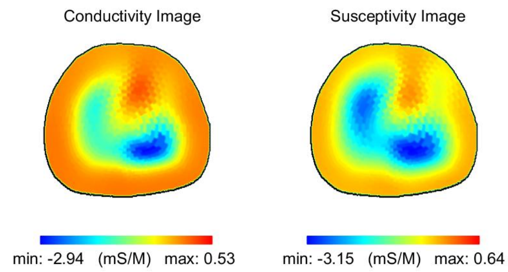

(b) BPD patient 1.

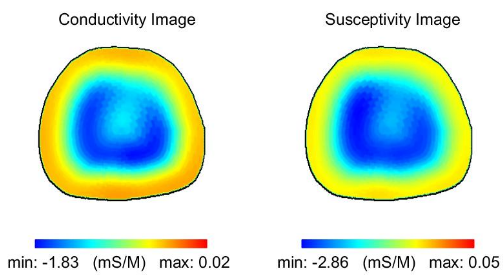

(c) Control 2.

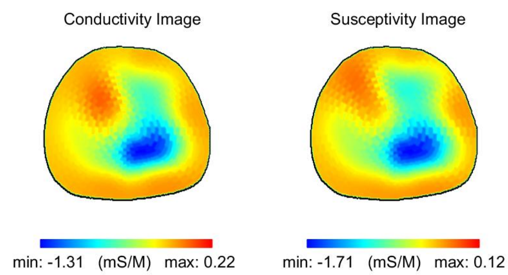

(d) BPD patient 2.

Figure 4.24: NOSER Ventilation Reconstructions on Controls 1 and 2, and BPD patients 1 and 2. (Left) Controls and (Right) BPD patients.

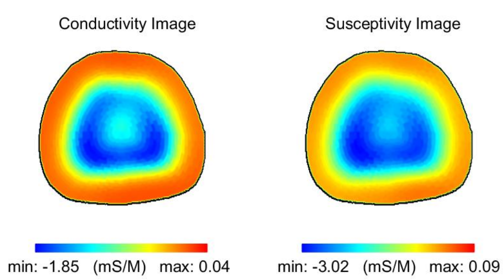

(a) Control 3.

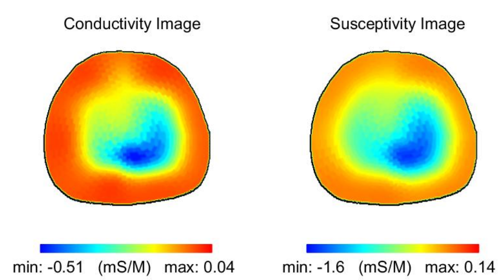

(b) BPD patient 3.

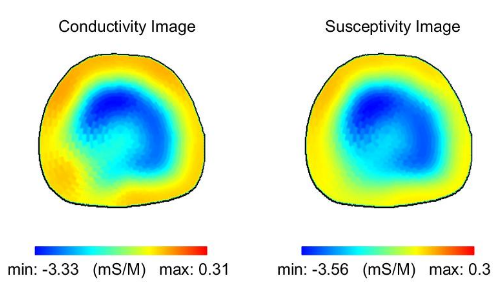

(c) Control 4.

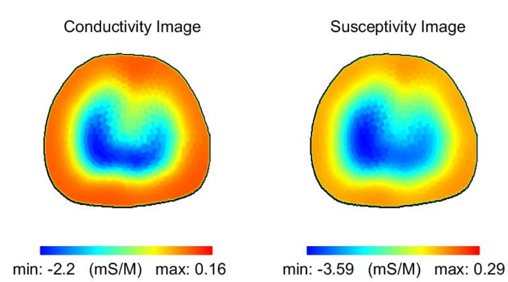

(d) BPD patient 4.

Figure 4.25: NOSER Ventilation Reconstructions on Controls 3 and 4, and BPD patients 3 and 4. (Left) Controls and (Right) BPD patients.

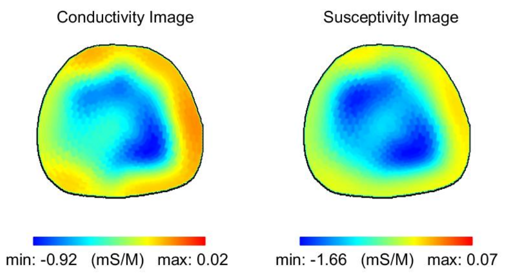

(a) Control 5.

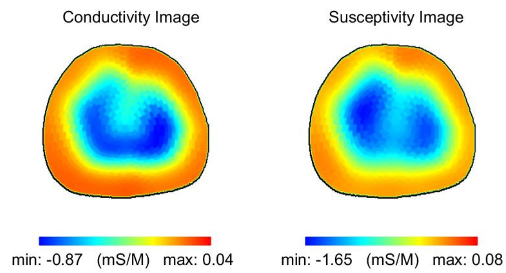

(b) BPD patient 5.

Figure 4.26: NOSER Ventilation Reconstructions on Control 5, and BPD patient 5. (Left) Control and (Right) BPD patient.

4.4.2 ToDLeR Ventilation Reconstructions

Figures 4.27-4.27 shows the ToDLeR ventilation reconstruction snapshots at full inspiration with reference frame at full expiration for the same control babies and BPD patients, and ventilatory sequence as the NOSER reconstructions. We can see a better spatial resolution and lung definition in the ToDLeR conductivity images when compared to the NOSER conductivity images for both controls and BPD patients. Conversely, the NOSER susceptivity images shows better reconstructions when compared to the ToDLeR susceptivity images.

A more pronounced effect due to the mild streaky opacity in the right upper lobe in the BPD patient 2 can be seen as the red spot in the right lung region in the conductivity image. Also, BPD patient 3 presents conductivity changes due to ventilation in the left lung.

BPD patient 4 has small ventilation changes in the conductivity image occurring in the left lung, which could be caused by the interstitial opacities. BPD patients 1 and 5 were also reported with interstitial opacities but it seems to cause small effects in the ventilation conductivity images.

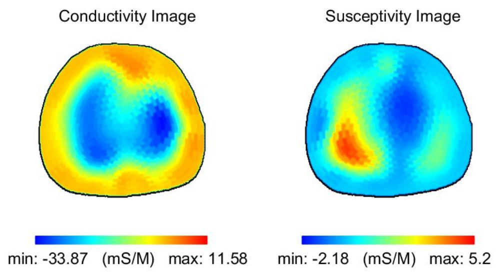

(a) Control 1.

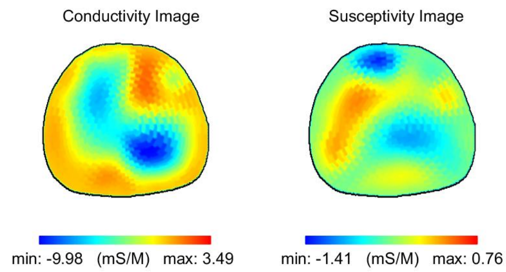

(b) BPD patient 1.

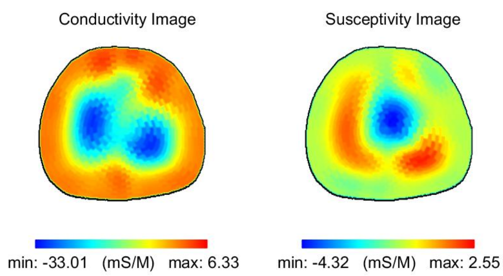

(c) Control 2.

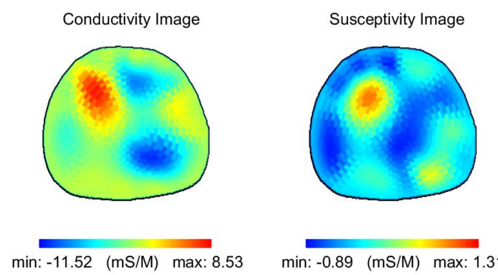

(d) BPD patient 2.

Figure 4.27: ToDLeR Ventilation Reconstructions on Controls 1 and 2, and BPD patients 1 and 2. (Left) Controls and (Right) BPD patients.

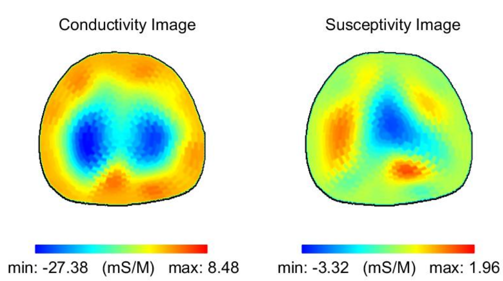

(a) Control 3.

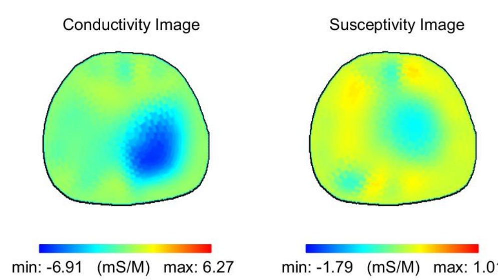

(b) BPD patient 3.

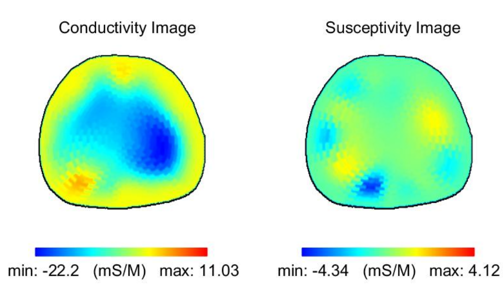

(c) Control 4.

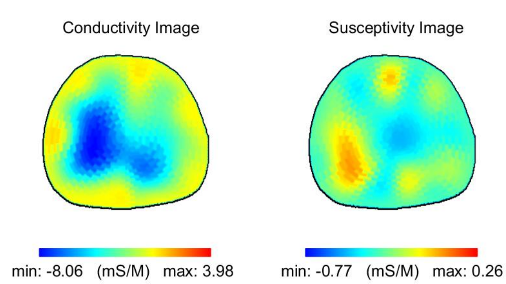

(d) BPD patient 4.

Figure 4.28: ToDLeR Ventilation Reconstructions on Controls 3 and 4, and BPD patients 3 and 4. (Left) Controls and (Right) BPD patients.

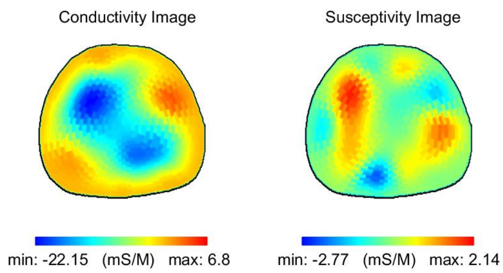

(a) Control 5.

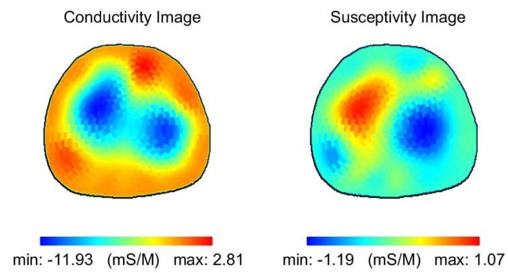

(b) BPD patient 5.

Figure 4.29: ToDLeR Ventilation Reconstructions on Control 5, and BPD patient 5. (Left) Control and (Right) BPD patient.

Both NOSER and ToDLeR reconstructions shows changes in ventilation from controls and BPD patients, and effects due to lung diseases in BPD patients. The ToDLeR conductivity reconstructions shows better resolution than the NOSER conductivity reconstructions which could be caused by the out-of-plane current effects since the ToDLeR reconstruction algorithm uses a 3D model to solve the forward and inverse problems.

The ToDLeR susceptivity images shows poor reconstructions when compared to the NOSER susceptivity reconstructions on controls and BPD patients. This could be related to regularization factors since we used the same parameters when reconstructing the conductivity and susceptivity images.

4.4.3 NOSER Perfusion Reconstructions

Figures 4.30-4.32 show the NOSER perfusion reconstruction snapshots at the end of the T-wave with reference frame at the end of the S-wave for the controls and BPD patients, which are displayed in numbering number order. Comparing the NOSER perfusion reconstructions from controls and BPD patients, we can see that they have a similar distribution of blood in the lung regions.

The radiology report for BPD patient 4 says that *("Heart size is mildly enlarged")*, which is not captured by the NOSER perfusion reconstructions, which could result from the low spatial res-

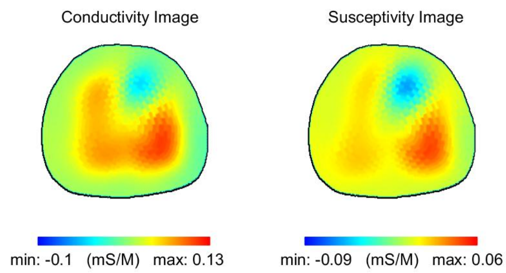

(a) Control 1.

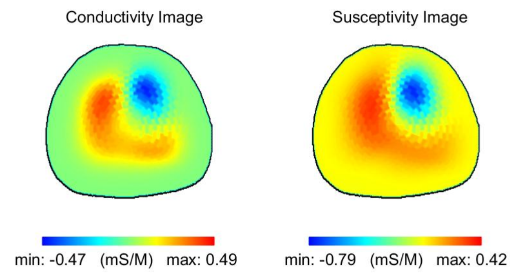

(b) BPD patient 1.

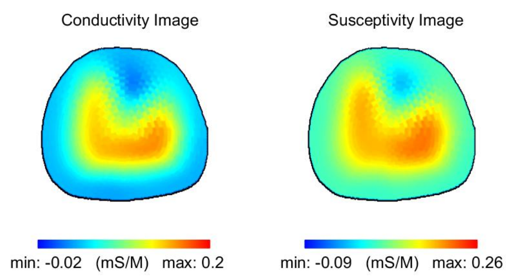

(c) Control 2.

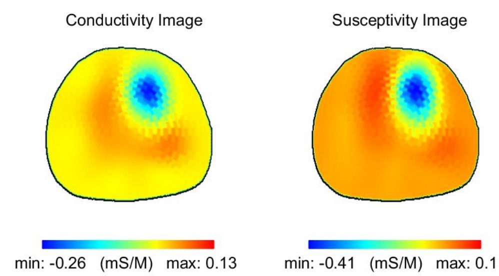

(d) BPD patient 2.

Figure 4.30: NOSER Perfusion Reconstructions on Controls 1 and 2, and BPD patients 1 and 2. (Left) Controls and (Right) BPD patients.

olution. The other BPD patients either have normal size heart or it is not reported on the radiology report.

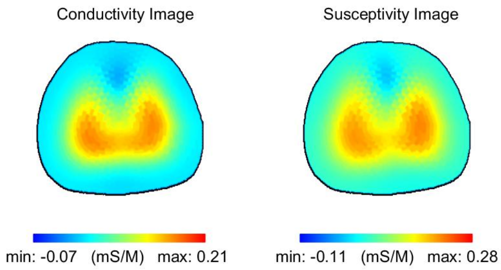

(a) Control 3.

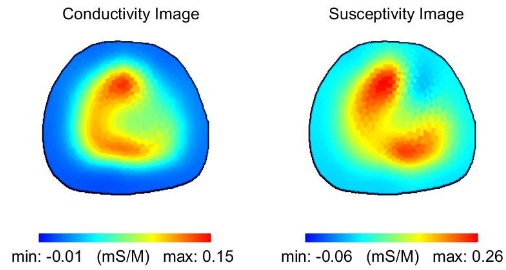

(b) BPD patient 3.

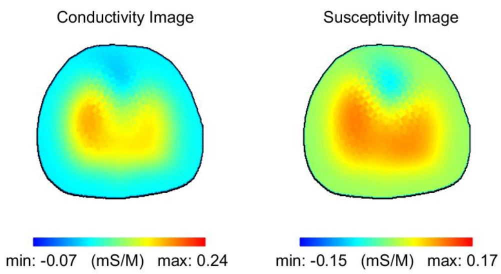

(c) Control 4.

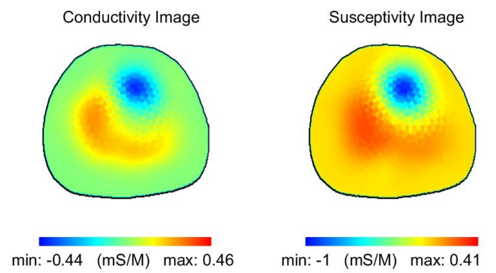

(d) BPD patient 4.

Figure 4.31: NOSER Perfusion Reconstructions on Controls 3 and 4, and BPD patients 3 and 4. (Left) Controls and (Right) BPD patients.

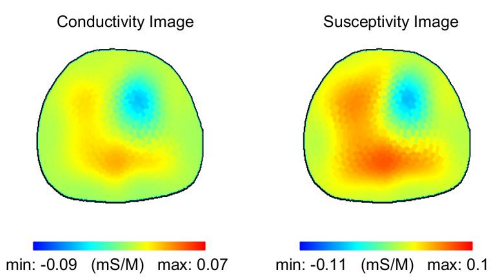

(a) Control 5.

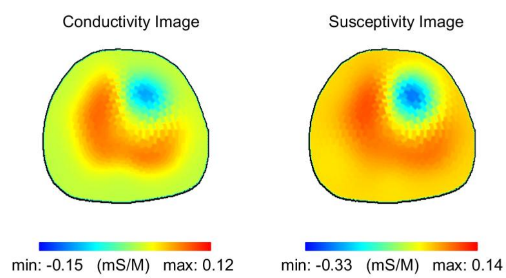

(b) BPD patient 5.

Figure 4.32: NOSER Perfusion Reconstructions on Control 5, and BPD patient 5. (Left) Control and (Right) BPD patient.

4.4.4 ToDLeR Perfusion Reconstructions

Figures 4.33-4.35 shows the ToDLeR perfusion reconstruction snapshots at the end of the T-wave with reference frame at the end of the S-wave for the controls and BPD patients. We can see a slightly better spatial resolution in the conductivity images when compared to the NOSER conductivity images.

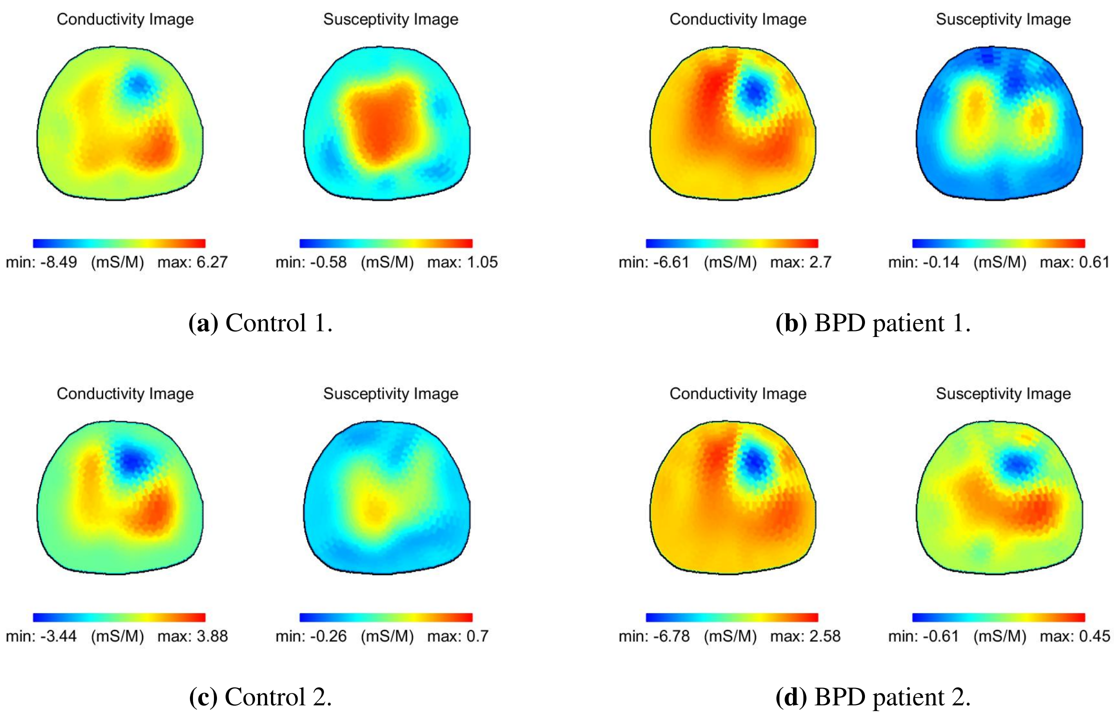

(a) Control 1.

(b) BPD patient 1.

(c) Control 2.

(d) BPD patient 2.

Figure 4.33: ToDLeR Perfusion Reconstructions on Controls 1 and 2, and BPD patients 1 and 2. (Left) Controls and (Right) BPD patients.

The ToDLeR conductivity image from BPD patient 3 shows better lung perfusion definition than the NOSER conductivity image for the same patient. Moreover, the BPD patient 4 heart region seems slightly enlarged when compared to controls and other BPD patients, which indicates the the ToDLeR conductivity images can capture smaller spatial changes when compared to the NOSER conductivity images.

The ToDLeR susceptivity images from perfusion changes are also poor when compared to the NOSER susceptivity images, which could be related to the regularization parameters since we can

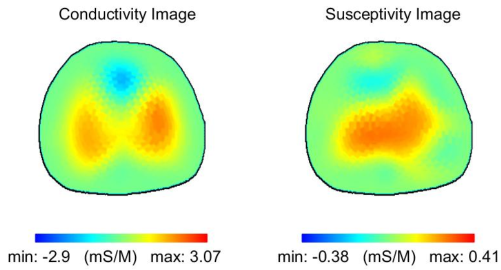

(a) Control 3.

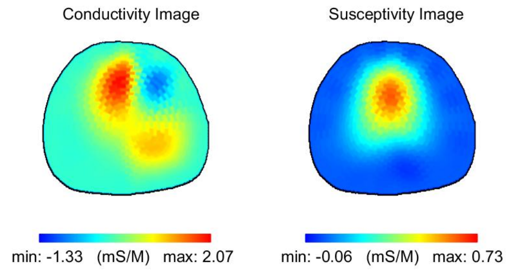

(b) BPD patient 3.

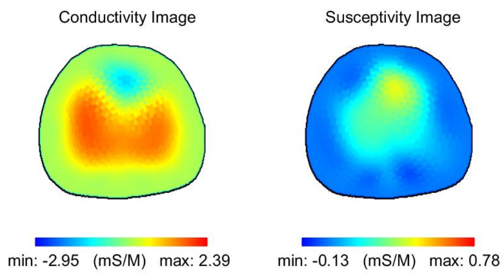

(c) Control 4.

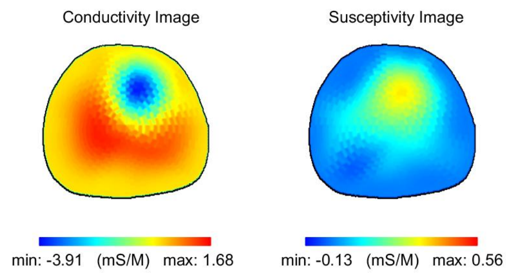

(d) BPD patient 4.

Figure 4.34: ToDLeR Perfusion Reconstructions on Controls 3 and 4, and BPD patients 3 and 4. (Left) Controls and (Right) BPD patients.

see good 2D ToDLeR susceptivity images from targets in a tank shown in section 4.1.1. Overall, the ToDLeR reconstructions have better spatial resolution than the NOSER reconstructions on controls and BPD patients.

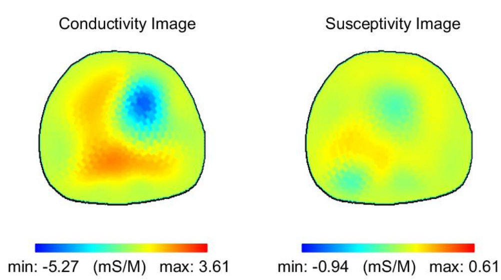

(a) Control 5.

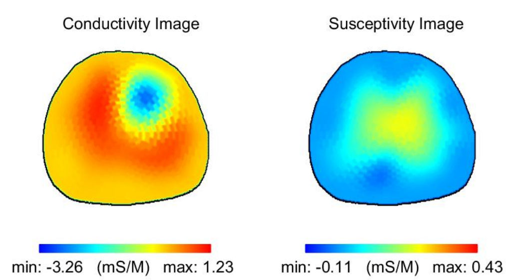

(b) BPD patient 5.

Figure 4.35: ToDLeR Perfusion Reconstructions on Control 5, and BPD patient 5. (Left) Control and (Right) BPD patient.

4.4.5 Longitudinal Analysis

A longitudinal analysis of the preterm infants was performed, and 18 preterm and 5 control infants were enrolled. In this study, two patients withdrew, leaving 16 patients included in the study. Table 4.1 shows the study population was 38% female and had a mean birth gestational age of 26.6 weeks and mean birth weight of 953 g. At 36 weeks post-menstrual age (PMA), 1 infant (6%) had no BPD, 6 (38%) had grade 1 BPD, 6 (38%) had grade 2 BPD, and 3 (19%) had grade 3 BPD.

Table 4.1: Demographics of patients with BPD.

	Preterm Infants (n=16)	**Term Infants (Controls) (n=5)**
Mean Gestational Age (range)	26.63 (23.4 – 31) weeks	38.83 (37-40.4) weeks
Mean Birth Weight (range)	953 (425 – 1575) grams	3031 (2440 – 2581) grams
Female n (%)	6 (38%)	3 (60%)
Mean Chronological Age at First EIT Visit (range)	49 (19-108) days	56.6 (42-106) days
BPD Severity		
No BPD, n (%)	1 (6.25%)	N/A
Grade 1, n (%)	6 (37.5%)	N/A
Grade 2, n (%)	6 (37.5%)	N/A
Grade 3, n (%)	3 (18.75%)	N/A

Figures 4.36-4.40 show the 2D ToDLeR reconstructions from ventilation and pulsatile perfusion at full inspiration and peak of systole with reference frames at full expiration and end of diastole, respectively, for 3 patients with different grades of BPD. During some visits, the patients were imaged pre (T1) and post (T2) airway clearance, which in some cases also included albuterol administration.

Figures 4.36-4.37 show the ventilation and pulsatile reconstructions from 4 visits of a patient with BPD grade 3. During visits 1, 2 and 4, the patient underwent airway clearance, which is used to removed mucus from the lungs, and albuterol was administered in visits 3 and 4. We can see that there is a better ventilation and perfusion distribution at T1 in visits 3 and 4 when compared to visits 1 and 2, which could be related to the patient's growth and response to treatment. However, there is a decrease in lung ventilated regions at T2 compared to T1 during visits 3 and 4, which is not expected since the patient received albuterol.

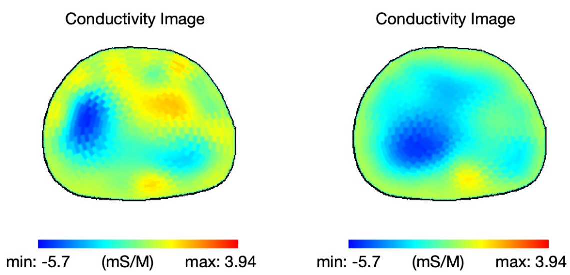

(a) Ventilation Visit 1 (T1-T2).

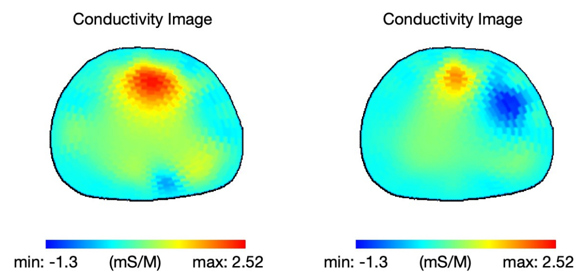

(b) Perfusion Visit 1 (T1-T2).

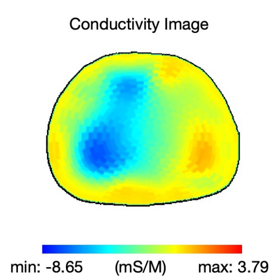

(c) Ventilation Visit 2.

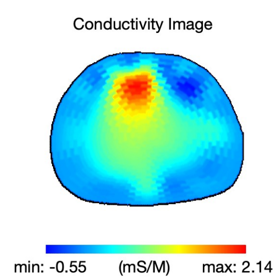

(d) Perfusion Visit 2.

Figure 4.36: Patient with grade 3 BPD. The patient underwent airway clearance in visit 1 and a follow-up in visit 2.

Figures 4.38-4.39 show the ventilation and pulsatile reconstructions from 3 visits of a patient with BPD grade 2. The patient underwent airway clearance and albuterol was administered only at visit 3. This patient also shows an improvement in ventilation and perfusion distributions in visits 2 and 3 when compared to visit 1.

Figure 4.40 shows the ventilation and pulsatile reconstructions from 2 visits of a patient with grade 1 BPD. The patient underwent airway clearance only at visit 1. This patient presented a more homogeneous ventilation at T1 than T2 during visit 1. Moreover, the ventilation reconstruction in

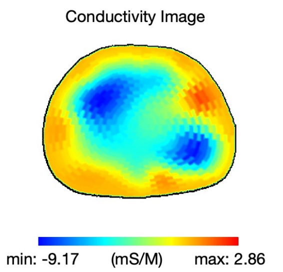

(a) Ventilation Visit 3 (T1-T2).

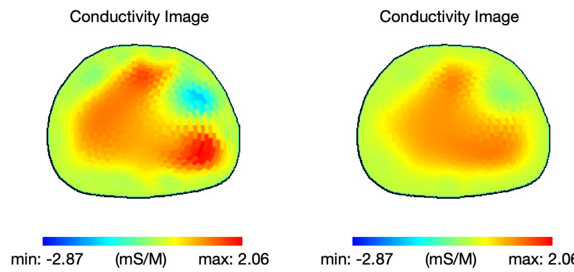

(b) Perfusion Visit 3 (T1-T2).

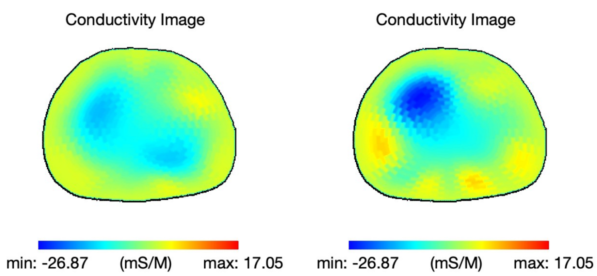

(c) Ventilation Visit 4 (T1-T2).

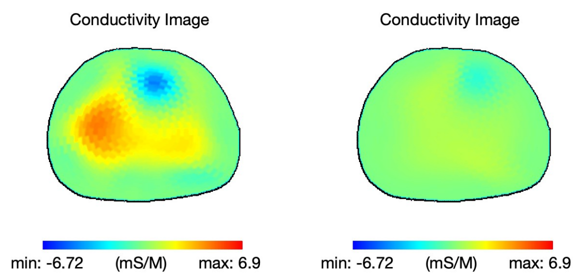

(d) Perfusion Visit 4 (T1-T2).

Figure 4.37: Patient with grade 3 BPD. The patient underwent airway clearance and albuterol in visit 3 and 4.

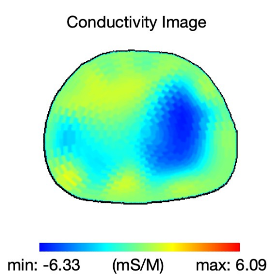

(a) Ventilation Visit 1.

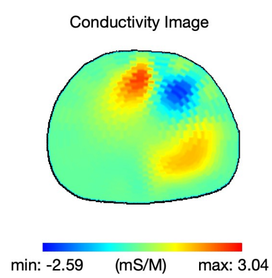

(b) Perfusion Visit 1.

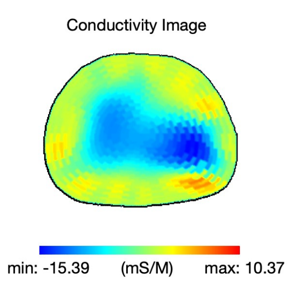

(c) Ventilation Visit 2.

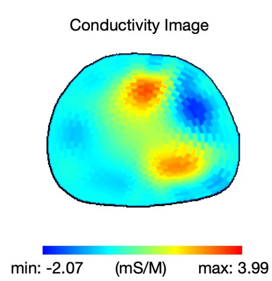

(d) Perfusion Visit 2 .

Figure 4.38: Patient with grade 2 BPD. The patient had follow-ups without airway clearance in visit 1 and 2.

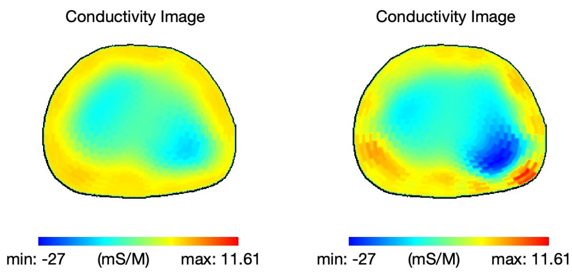

(a) Ventilation Visit 3 (T1-T2).

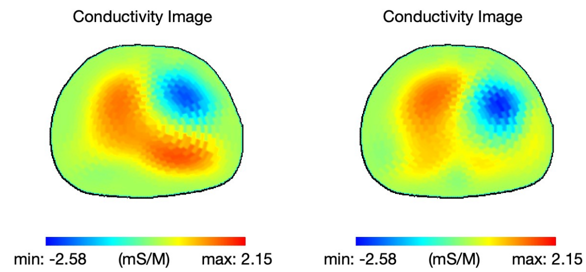

(b) Perfusion Visit 3 (T1-T2).

Figure 4.39: Patient with grade 2 BPD. The patient underwent airway clearance without albuterol in visit 3.

visit 2 shows more heterogeneity in ventilation than during visit 1 while the perfusion reconstruction has a better contrast during visit 2 than during visit 1.

Both patients with grade 2 and 3 BPD shown improvements over time for ventilation and perfusion images. Although the reconstructions at T2 seems to be worse than then reconstructions at T1, this could be related to the airway clearance, which can cause electrode attachment issues as well as put the patient in distress. Also, the patient with grade 1 BPD showed more homogeneous ventilation during visit 1 than visit 2, which could be explained by the patient activity during data collection, or worsening condition.

Table 4.2 shows GI and tidal volume outcome measures in control infants and infants of each BPD severity at their study visit closest to 36 weeks PMA. This statistical analysis was performed by the statisticians Ella Hagopian and John T. Brinton from University of Colorado Denver. Preterm infants had significantly higher GI than control infants. This trend was sustained for all BPD groups compared to controls. When combined into a single group of patients with BPD (n=13), the mean GI was significantly higher compared to the five controls (mean=0.49 SD=0.1 vs. mean=0.32 SD=0.1, p=0.002). Additionally, GI was higher in preterm infants at the visit closest to 36 weeks PMA when compared to controls. On the other hand, Tidal volumes for infants with BPD tended to be lower compared to control infants at the visit closest to 36 weeks PMA, although this difference was not statistically significant, and the trend was not sustained

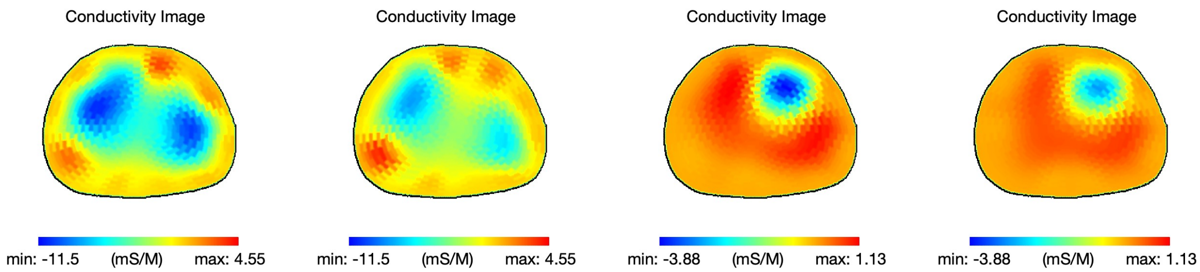

(a) Ventilation Visit 1 (T1-T2). **(b)** Perfusion Visit 1 (T1-T2).

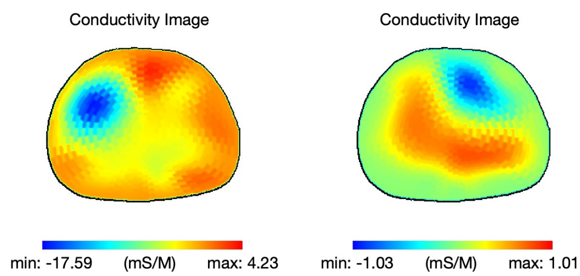

(c) Ventilation Visit 2. **(d)** Perfusion Visit 2.

Figure 4.40: Patient with grade 1 BPD. The patient underwent airway clearance without albuterol in visit 1 and a follow-up in visit 2.

Table 4.2: Summary Mean EIT Measurements in Preterm vs Term Infants at EIT visit closest to 36 weeks PMA.

EIT Metric	Control (N=5)	None/Grade 1 (N=9)	Grade 2 (N=2)	Grade 3 (N=2)	p-value
GI	0.32 (0.1)	0.51 (0.1)	0.41 (0.1)	0.51 (0.1)	0.02*
Tidal Volume	50.00 (33.5)	37.09 (11.2)	27.30 (4.9)	41.69 (12.3)	0.54

Note: Mean (SD), [Median]. *Omnibus F-test. Abbreviations: EIT=Electrical Impedance Tomography; BPD=Bronchopulmonary Dysplasia; GI=Global Inhomogeneity Index; VQI=Ventilation Perfusion Index.

4.5 EIT Reconstructions on ARDS Patients

This section shows the ventilation conductivity images from a subset of eight healthy control adults with BMI of $(22.8, \pm 4.8)\ \mathrm{kg/m^2}$ and eight ARDS patients with BMI of $(24.4, \pm 4.8)\ \mathrm{kg/m^2}$ under mechanical ventilation with EIT data collected using the GE GENESIS System. The data were collected at UCHealth at University of Colorado Anschutz Medical Campus in the Intensive Care Unit (ICU).

A total of 32 electrodes arranged in 2 rows of 16 were placed around each subject's torso, and 3D trigonometric current patterns with amplitude $93.5\,\mu\mathrm{A}$ and frequency of $10\,\mathrm{kHz}$ were applied during the data collection. Moreover, the ventilation reconstructions from control subjects were done during tidal breathing while laying in supine position.

4.5.1 Comparison versus healthy subjects

Figure 4.41 shows the 3D ToDLeR ventilation conductivity images snapshots at full inspiration with reference frame at full expiration from eight healthy control adults while Figure 4.42 shows the reconstructions from mechanically ventilated ARDS patients. The reconstructions are displayed in numbering order and the susceptivity images were not computed since the GE GENESIS system operates at $10\,\mathrm{kHz}$, which is not high enough to show susceptivity changes.

The conductivity images from controls show more ventilation changes occurring in the anterior parts of the lungs. This effect is expected because the controls were laying in supine position which cause dorsal lung compression due to gravitational effects [87].

The conductivity images from ARDS patients are overall different from the control conductivity images. Table 4.3 contains the radiology report for each ARDS patient. The report for ARDS patient 1 says *"Increased streaky retrocardiac opacities could reflect atelectasis"*, which could explain why there is more conductivity changes towards the anterior lung than the posterior lung regions. The report for ARDS patient 2 says *"Streaky bibasilar opacities favor atelectasis"*, which can be noticed in the conductivity images since most of the ventilation changes is located in the anterior lung regions.

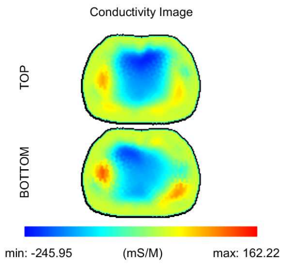

(a) Control 1.

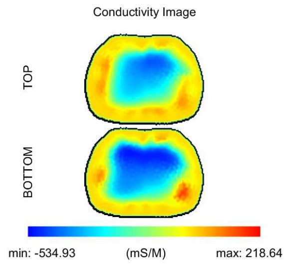

(b) Control 2.

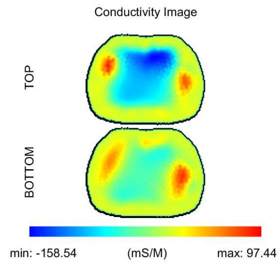

(c) Control 3.

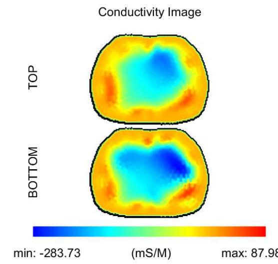

(d) Control 4.

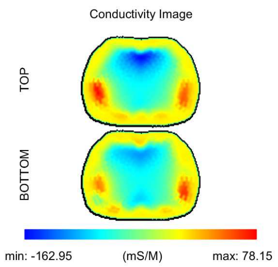

(e) Control 5.

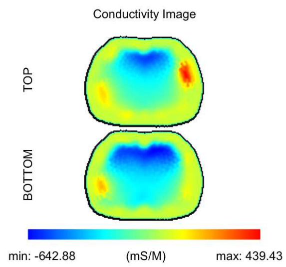

(f) Control 6.

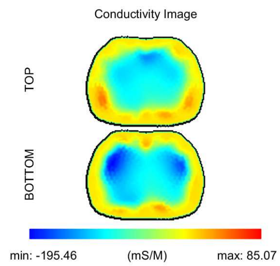

(g) Control 7.

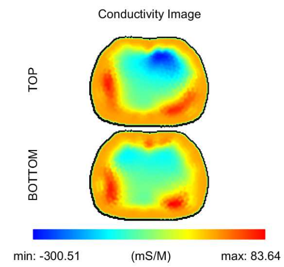

(h) Control 8.

Figure 4.41: EIT Ventilation Reconstructions on Controls using the GENESIS System.

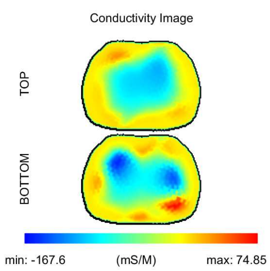

(a) ARDS patient 1.

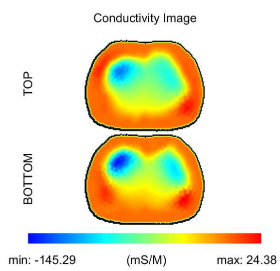

(b) ARDS patient 2.

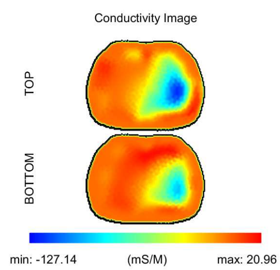

(c) ARDS patient 3.

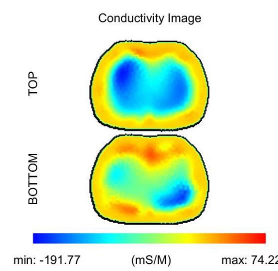

(d) ARDS patient 4.

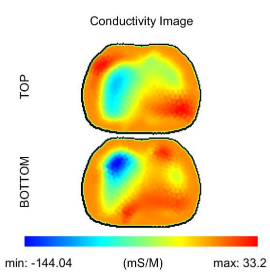

(e) ARDS patient 5.

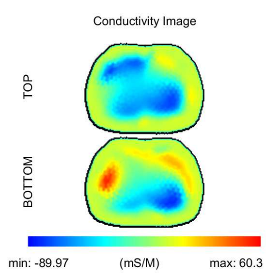

(f) ARDS patient 6.

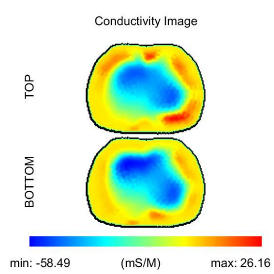

(g) ARDS patient 7.

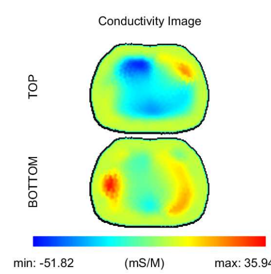

(h) ARDS patient 8.

Figure 4.42: EIT Ventilation Reconstructions on ARDS patients using the GENESIS System.

Table 4.3: Radiology report from ARDS patients.

Patient	Radiology report
1	Increased streaky retrocardiac opacities could reflect atelectasis, infection/aspiration or combination of these processes.
2	Streaky bibasilar opacities favor atelectasis. No consolidation or pleural effusion.
3	Residual hazy opacities throughout the right lung
4	Slightly improved left perihilar opacities. Decreased left pleural effusion. Stable right pleural effusion.
5	The central airways are patent. Small volume left pleural effusion. Mixed density consolidation in the left lower lobe. Opacities in the left upper and lower lobe superior segment.
6	Similar mild interstitial opacities bilaterally, left greater than right
7	Patchy consolidation of the right lower lobe air bronchograms.
8	Patchy central airspace opacities in both upper lobes. Trace bilateral pleural effusions with small adjacent hyperattenuating atelectasis.

We can see that the report for ARDS patient 3 says *"hazy opacities through the right lung"*, and the conductivity images show small to no ventilation changes in the right lung. Conversely, ARDS patient 5 shows small ventilation changes in the left lung which is in accordance with the radiology report which states that *"small volume left pleural effusion and mixed density consolidation in the left lower lobe"*.

ARDS patient 4 shows small aerated region in the right lower lung, but the radiology report says that *"Stable right pleural effusion"*. The left lung shows good ventilation in the conductivity images. The conductivity image shows more ventilation in the upper lungs for ARDS patient 6 than the lower lungs, with the left lower lung being better ventilated in the posterior section, which could relate to the reported *"Similar mild interstitial opacities bilaterally, left greater than right"*.

The conductivity image for ARDS patient 7 shows good ventilation in both lungs, with more ventilation changes occurring in the anterior part, which agrees with the radiology report. In addition, ARDS patient 8 has heterogeneous ventilation distribution in the upper lungs while small ventilation occurring in the lower lungs, which could be consist with the radiology report - *"Patchy central airspace opacities in both upper lobes"*.

The 3D ToDLeR conductivity images show good accordance with the radiology reports, including the affected lung regions. Some discrepancy could be explained by electrode placement being either to high or low on the torso, which could make some pathology not appear in the conductivity images. Moreover, for some ARDS patients, we removed the data from some electrodes when running the reconstructions due to poor or no connection during the data collection, which reduces the reconstruction quality.

4.5.2 Pre and during SBT reconstructions and statistical results

Figures 4.43 and 4.44 show the EIT reconstructions for the same 8 patients at full inspiration during Pre SBT (T1) and On SBT (T2) displayed on the same scale. Table 4.4 shows the demographic information for the subset of 8 patients with groups a (successful liberation in less than 1 day), b (required greater than or equal to 1 day for ventilator liberation) and c (terminally extubated or discharged) [88].

Table 4.4: Demographic information from a subset of 8 mechanically ventilated patients.

Patient	Group	Gender	Age (years)	Thorax Perimeter (inches)	BMI (kg/m2)
1	c	F	62	36	21.19
2	a	M	47	36	20.21
3	c	M	73	36	21.43
4	b	M	52	40	22.33
5	c	M	68	32	25.47
6	a	F	73	44	31.33
7	a	M	62	36	21.19
8	a	M	79	44	32.22

We can see that there is minimal change in the reconstructions from T1 to T2, except for ARDS patient 1 and ARDS patient 8. For those patients, we can see some ventilation differences in both upper and lower lungs at T1 and T2. Figures 4.45-4.46 show the estimated global and regional volumes (ULL, URL, LRL, LLL) derived from the EIT-conductivity images.

For all patients, except ARDS 4 and 6, the estimated global volumes are in acceptable range between 400 mL and 800 mL at T1 and T2. Some differences to the actual applied volume of air during mechanical ventilation can be related to defining the voxel volumes, regularization, and electrode artifacts.

EIT-derived measures were also compared between T1 and T2 for the 18 patients with interpretable data (Table 4.5) using statistical hypothesis tests. In the cases for which the data samples were not normally distributed, the logarithmic transformation or a non-parametric test was performed. The paired samples t-test or the non-parametric Wilcoxon rank-sum test were used to verify if there was a statistical difference ($p < 0.05$) for the mean or median between T1 and T2.

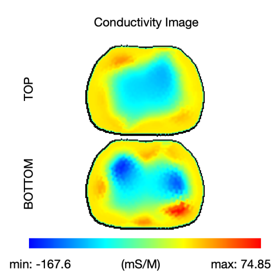

(a) ARDS patient 1 (T1-T2).

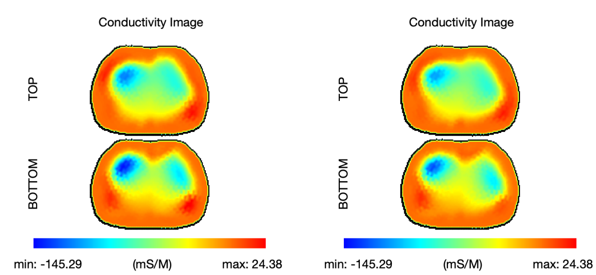

(b) ARDS patient 2 (T1-T2).

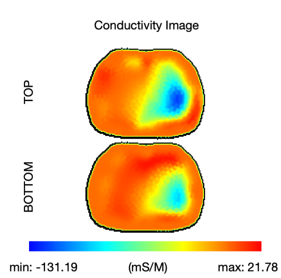

(c) ARDS patient 3 (T1-T2).

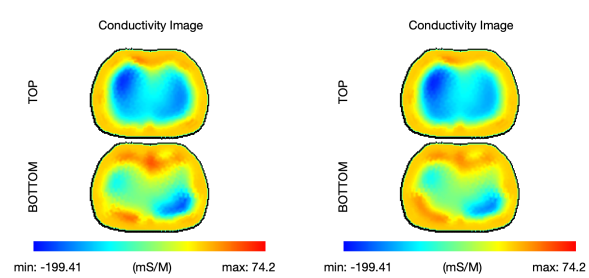

(d) ARDS patient 4 (T1-T2).

Figure 4.43: EIT SBT Ventilation Reconstructions at T1 and T2 of ARDS patients using the GENESIS System.

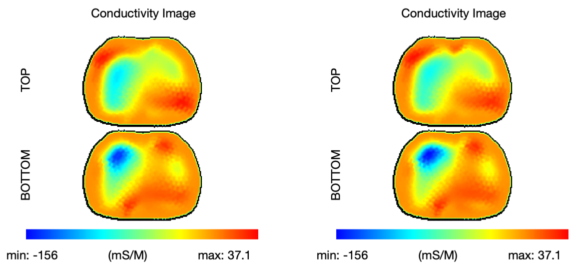

(a) ARDS patient 5 (T1-T2).

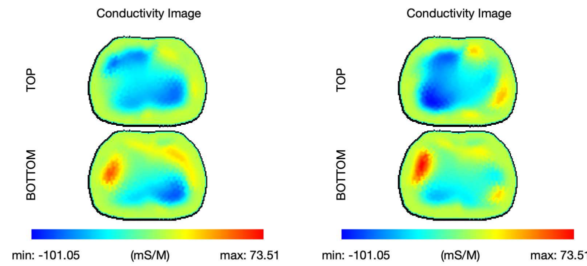

(b) ARDS patient 6 (T1-T2).

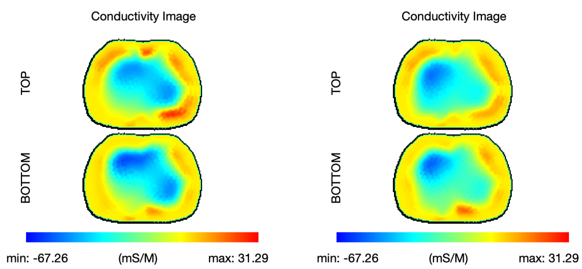

(c) ARDS patient 7 (T1-T2).

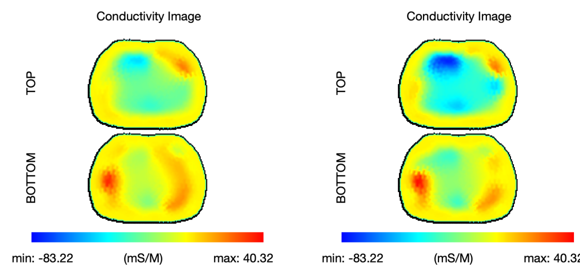

(d) ARDS patient 8 (T1-T2).

Figure 4.44: EIT SBT Ventilation Reconstructions at T1 and T2 of ARDS patients using the GENESIS System.

GI, global volume, RSBI, RVDI, the RVD Spatial Mean (RVDSM, the average of RVD from all lung voxels), and the RVD Spatial CV (RVDSCV, the coefficient of variation defined by RVDI divided by RVDSM) were computed at T1 and T2 using 3 consecutive breaths in the computations.

We did not observe significant differences between T1 and T2 across the cohort for RVDSM, RVDI, RVDSCV, global volume, GI, or RSBI. Of the 18 patients, 7 underwent successful liberation in less than 1 day, whereas 6 required greater than or equal to 1 day for ventilator liberation. The remaining five were terminally extubated or discharged from hospital on MV.

Among patients with successful liberation and failed liberation, we can see that there was a small decrease in RVDSM, GI, and RSBI between T1 and T2 while there was a small increase in RVDI and RVDSCV for both groups. Comparing the patients with successful and failed liberation, the RVSM, RVDI, RVDSCV, and GI are higher for the failed liberation group than the succesful liberation. However, these small changes were not statistically significant.

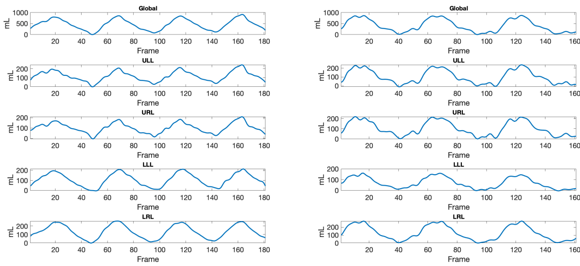

(**a**) ARDS patient 1 (T1-T2).

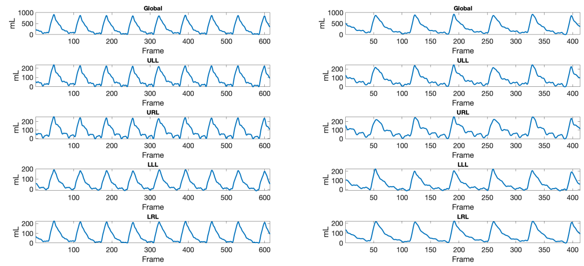

(**b**) ARDS patient 2 (T1-T2).

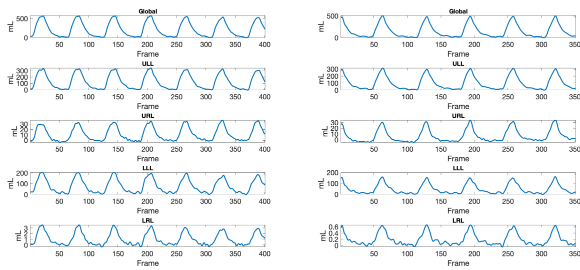

(**c**) ARDS patient 3 (T1-T2).

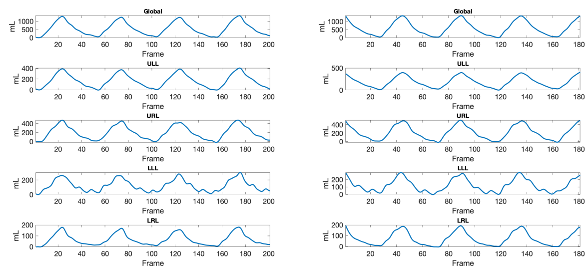

(**d**) ARDS patient 4 (T1-T2).

Figure 4.45: Estimated global and regional volumes at T1 and T2 from ARDS patients 1, 2, 3, and 4.

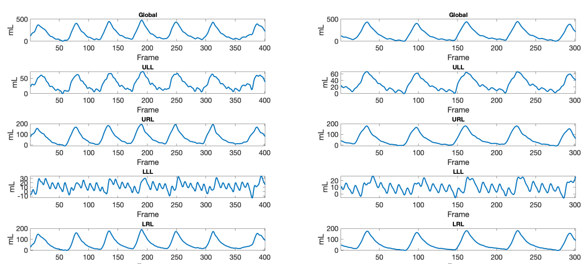

(**a**) ARDS patient 5 (T1-T2).

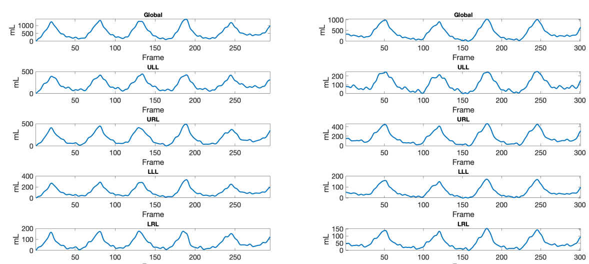

(**b**) ARDS patient 6 (T1-T2).

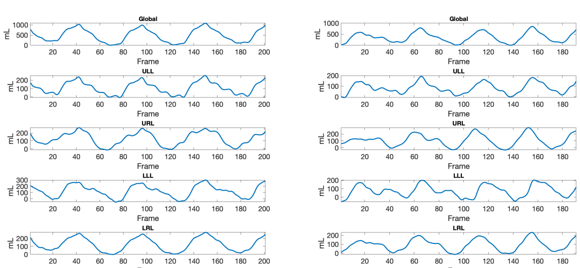

(**c**) ARDS patient 7 (T1-T2).

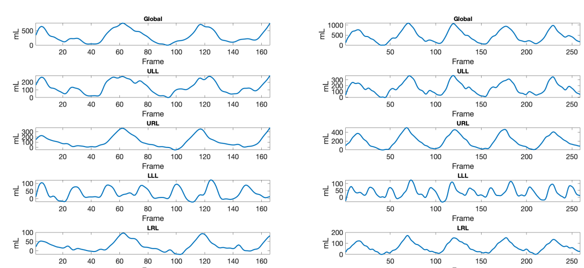

(**d**) ARDS patient 8 (T1-T2).

Figure 4.46: Estimated global and regional volumes at T1 and T2 from ARDS patients 5, 6, 7, and 8.

During SBT, patients are still under mechanical ventilation with minimal ventilator settings to evaluate the patients ability to breath without the ventilator assistance. Since the data collected at T1 and T2 are within 30 minutes, it may occur that there was not enough time to evaluate the differences between T1 and T2. Moreover, 18 patients may not have lead to enough power in the statistical analysis to determine whether there were differences between T1 and T2.

Table 4.5: Summary of Electrical Impedance Tomography-Derived Measures From 18 Mechanically Ventilated Patients Before the Spontaneous Breathing Trial (T1) and During the Spontaneous Breathing Trial (T2).

Measure	T1, Median (IQR)	T2, Median (IQR)	p-value
Entire cohort, n = 18			
RVD spatial	49.78 (41.39–55.28)	48.74 (44.65–53.58)	0.974
RVDI	11.33 (7.38–13.95)	11.28 (8.15–15.54)	0.840
RVD spatial CV	0.22 (0.15–0.33)	0.24 (0.16–0.35)	0.940
Global volume	810.42 (570.44–1128.60)	877.06 (594.35–1006.36)	0.929
GI	83.09 (77.38–89.32)	77.28 (73.73–92.10)	0.442
RSBI	39.26 (34.39–60.62)	41.25 (27.62–55.29)	0.832
Successful liberation, n = 7			
RVD spatial	51.95 (44.88–55.14)	48.06 (43.34–50.36)	0.133
RVDI	7.56 (6.32–14.72)	8.73 (6.80–14.06)	0.781
RVD spatial CV	0.18 (0.12–0.28)	0.19 (0.16–0.31)	0.491
Global volume	862.95 (750.49–1200.60)	1004.03 (864.51–1018.85)	0.578
GI	78.05 (77.17–97.19)	77.77 (73.00–90.57)	0.219
RSBI	52.67 (38.20–60.79)	50.70 (44.90–57.34)	0.469
Failed liberation, n = 6			
RVD spatial	53.27 (44.51–55.91)	48.29 (41.49–53.58)	0.333
RVDI	11.33 (9.49–12.83)	11.78 (9.53–14.94)	1.000
RVD spatial CV	0.22 (0.20–0.34)	0.26 (0.20–0.29)	0.803
Global volume	905.61 (657.45–1181.35)	821.37 (594.35–1221.11)	0.481
GI	85.27 (82.99–92.19)	79.34 (75.78–102.13)	1.000
RSBI	48.42 (35.38–66.37)	40.13 (22.00–73.26)	0.275

4.5.3 Comparison versus X-rays and CT scans

To evaluate the spatial resolution and regional lung information of the EIT reconstructions, the conductivity images at full inspiration were also compared to X-rays and CT scans of the patients with ARDS taken at the nearest date to the EIT data collection. Also, the X-rays and CT scans correspond to the radiology reports shown previously in Table 4.3, and the top and bottom CT scan slices correspond to the thoracic vertebrae (T5) and (T8), respectively, which is an estimation of each electrode plane.

Figures 4.47 and 4.48 show the EIT reconstructions of each patient shown previously and their corresponding X-ray or CT scans. We can see that for ARDS patient 3, there are opacities throughout the lower and middle right lung lobe, which is consistent with the EIT reconstruction.

The same consistency can be observed for the ARDS patients 5, 7, and 8. The CT scan for ARDS patient 5 C shows consolidations in the left lower lobe while the EIT images show very little to no changes in the left lower lung. The CT scan for ARDS patient 7 shows consolidations in the posterior right lower lobe, which is consistent with the EIT reconstructions. The CT scan for ARDS patient 8 shows abnormalities in the lower lungs, which can be observed as small changes in the EIT reconstruction of the bottom slice.

For ARDS patients 1, 2, and 4, a professional radiologist can better distinguish abnormalities in the lungs as in the radiology report (Table 4.3), which could relate to the effects observed in the EIT reconstructions. However, we can see that overall the EIT reconstructions are consistent with the X-rays and CT scans.

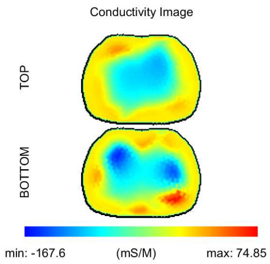

(**a**) ARDS patient 1.

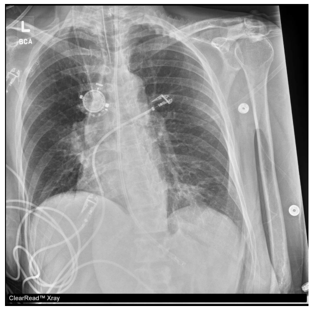

(**b**) X-ray: 6 days apart.

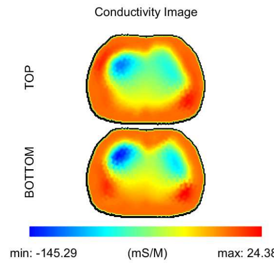

(**c**) ARDS patient 2.

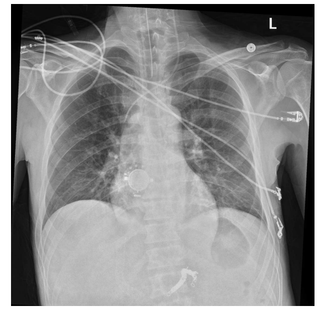

(**d**) X-ray: same day.

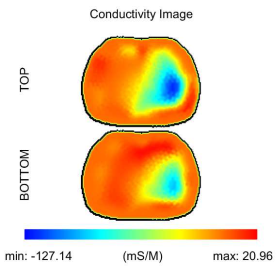

(**e**) ARDS patient 3.

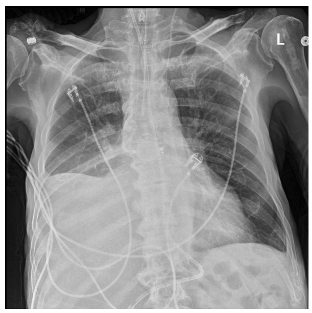

(**f**) X-ray: 2 days apart.

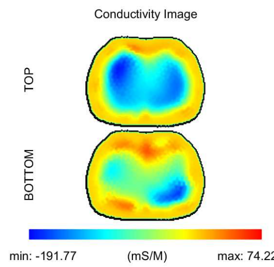

(**g**) ARDS patient 4.

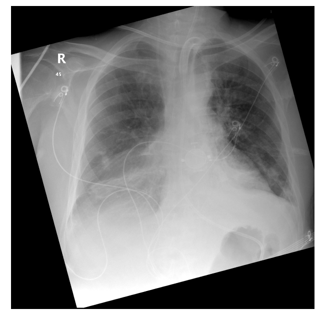

(**h**) X-ray: 5 days apart.

Figure 4.47: EIT Ventilation Reconstructions on ARDS patients and corresponding X-rays or CT scans for ARDS patients 1-4.

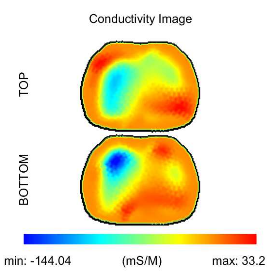

(**a**) ARDS patient 5.

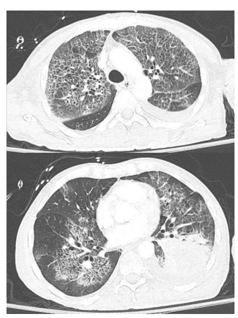

(**b**) CT: 7 days apart.

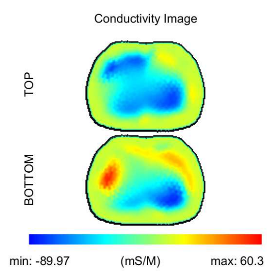

(**c**) ARDS patient 6.

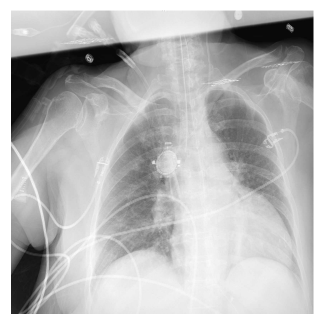

(**d**) X-ray: 2 days apart.

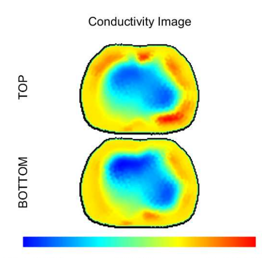

(**e**) ARDS patient 7.

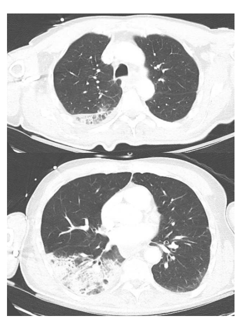

(**f**) CT: 8 days apart.

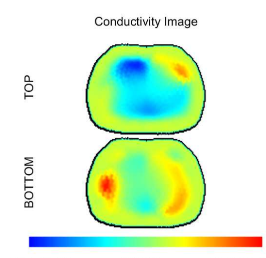

(**g**) ARDS patient 8.

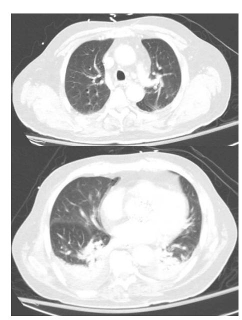

(**h**) CT: 1 day apart.

Figure 4.48: EIT Ventilation Reconstructions on ARDS patients and corresponding X-rays or CT scans for ARDS patients 5-8.

4.6 EIT Reconstructions on CF Patients

In the CF study, 20 patients were imaged over the span of three years. This section shows the ventilation and pulsatile perfusion images from a subset of eight controls aged $(8, \pm 2.5)$ years old and CF patients aged $(11, \pm 3.9)$ years old during their first visit computed using the 3D ToDLeR algorithm. This subset of patients was chosen because of having ages similar to the control subjects. Data were collected at Children's Hospital Colorado in the Breathing Institute using the ACT5 system.

A total of 32 electrodes arranged in 2 rows of 16 were placed around each subject's torso, and 3D trigonometric current patterns with amplitude $0.35\,\mathrm{mA}$ and frequency of $93.750\,\mathrm{kHz}$ were applied during the data collection at 27 frames/sec. The ventilation reconstructions computed from data collected during tidal breathing while the perfusion reconstructions were computed from data collected during breath-holding while the subject was sitting upright.

4.6.1 Ventilation Reconstructions

Table 4.6 shows the demographics for the subset of eight CF patients. We can see that all CF patients, except for CF patient 7, are receiving cystic fibrosis transmembrane conductance regulator (CFTR) modulators - either Trikafta or Orkambi.

Table 4.6: CF patient demographics.

Patient	Gender	Age	CF Genotypes	Treatment	FVC(%)	FEV1(%)
1	F	10y0m	F508del/F508del	Trikafta	108	114
2	F	8y0m	F508del/W128X	Trikafta	121	122
3	M	17y4m	F508del/2789+5G>A	Trikafta	88	98
4	M	14y4m	F508del/2789+5G>A	Trikafta	125	124
5	M	4y10m	F508del/F508del	Orkambi	83	83
6	M	11y1m	F508del/G542X	Trikafta	96	96
7	F	11y1m	F508del/F508del	None	99	105
8	M	13y9m	F508del/F508del	Trikafta	119	115

Table 4.7 shows the FVC and FEV1 for each healthy control subject. Except for control 8, which has FVC = 65% and FEV1 = 70%, all other control subjects have FVC and FEV1 values above 90%. The low values of FVC and FEV1 reported from the control subject 8 may be related to practice, a lack of experience, skill, or effort when doing the pulmonary function tests.

Table 4.7: Spirometry results from control subjects.

Control	Gender	Age	FVC(%)	FEV1(%)
1	M	6y10m	101	112
2	M	8y8m	106	97
3	F	5y0m	102	98
4	M	9y2m	108	107
5	M	7y4m	99	92
6	M	6y6m	108	112
7	M	11y0m	114	94
8	F	12y0m	65	70

Figures 4.49-4.52 show the ventilation reconstruction snapshots at full inspiration with reference frame at full expiration from control subjects and CF patients, which are displayed in numbering order. The conductivity images from CF patients 1-4 show similar lung aerated regions as the conductivity images from controls. Except for CF patient 3, the pulmonary function test Forced Vital Capacity (FVC) and Forced Expiratory Volume in 1 second (FEV1) are above 100%, which indicates good pulmonary ventilation. We also observed that both the controls and CF patients susceptivity images have poor resolution, which could be related to the applied $93.750\,\mathrm{kHz}$ frequency since the susceptivity highly depends on ω.

CF patients 5-7 have FVC and FEV1 around 100%, with CF patient 5 having FVC 83, which also indicates normal values, but the conductivity images show poor lung ventilation during tidal breathing, which may be due to lung damage. The conductivity image from CF patient 8 shows good lung ventilation with the patient reporting FVC and FEV1 above 100%. Also, PFTs have poor correlation with lung health in persons with CF, which can possibly be attributed to the fact that they do them often, and so they can get good at performing the tests.

The EIT conductivity images seem to be in good accordance with the pulmonary function tests showing more ventilated lung areas for those with high FCV and FEV1. The susceptivity images do not provide information about the lung conditions since they seem to be exhibiting more reconstruction artefacts.

The CFTR modulators are designed to stop CF disease progression as long as the person continues to take them, however, it will not revert lung damage caused by the CF disease. Thus, some patients may have more lung damage depending how early aged they started the CFTR therapy and how fast the disease progressed.

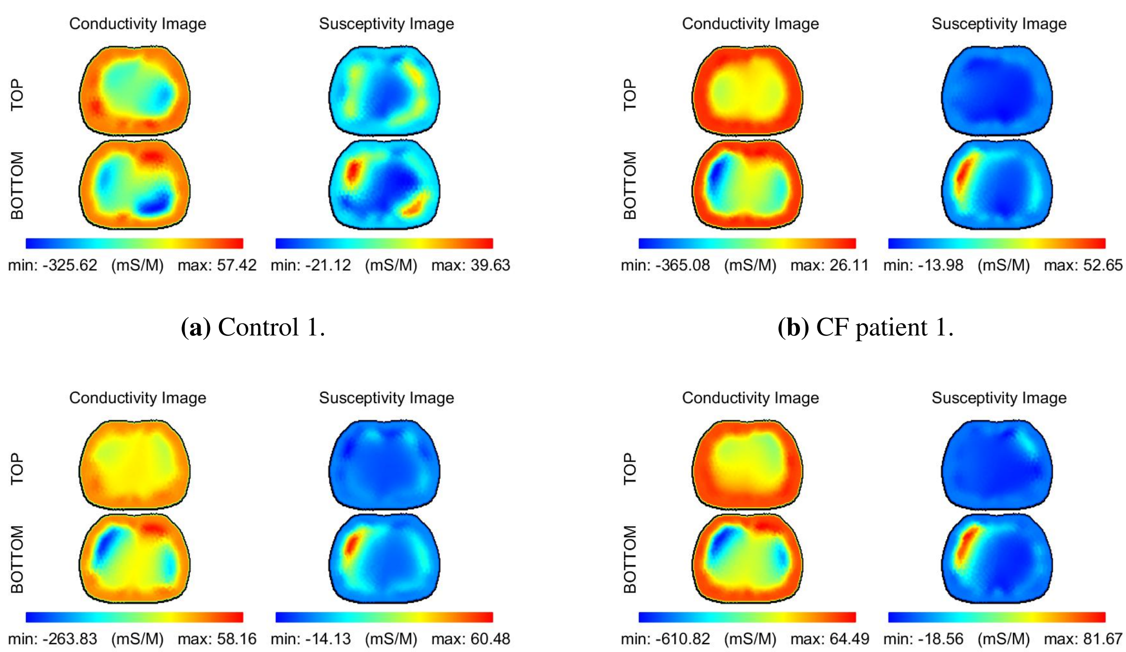

(a) Control 1.

(b) CF patient 1.

(c) Control 2.

(d) CF patient 2.

Figure 4.49: EIT Ventilation Reconstructions on Controls 1 and 2, and CF patients 1 and 2. (Left) Controls (Right) CF patients.

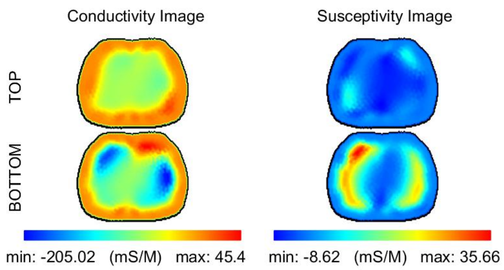

(a) Control 3.

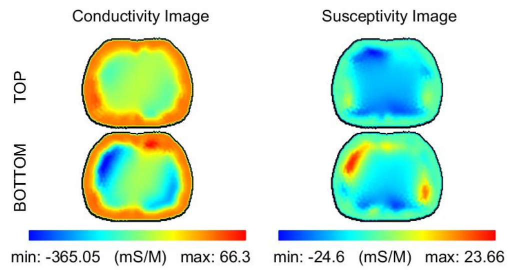

(b) CF patient 3.

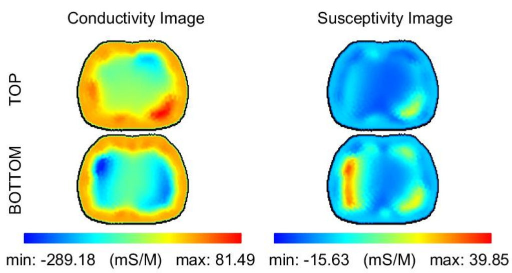

(c) Control 4.

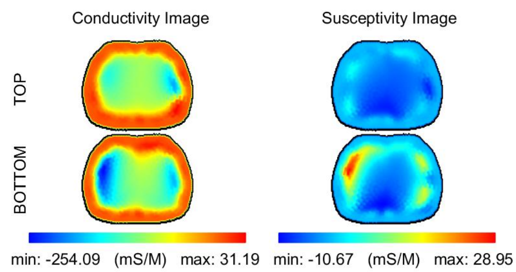

(d) CF patient 4.

Figure 4.50: EIT Ventilation Reconstructions on Controls 3 and 4, and CF patients 3 and 4. (Left) Controls (Right) CF patients.

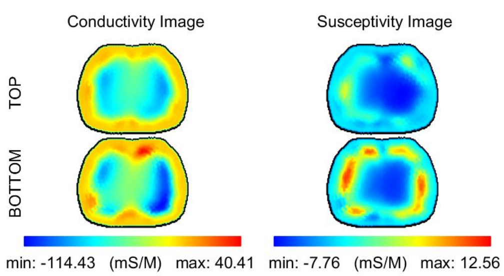

(a) Control 5.

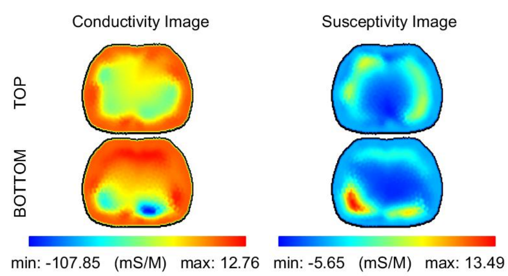

(b) CF patient 5.

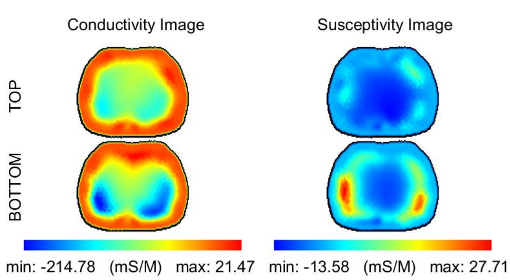

(c) Control 6.

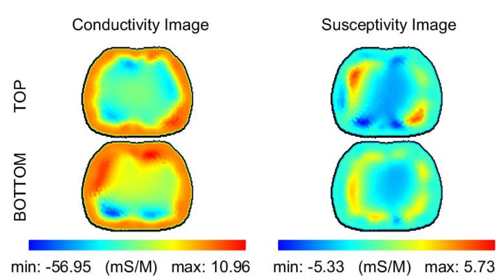

(d) CF patient 6.

Figure 4.51: EIT Ventilation Reconstructions on Controls 5 and 6, and CF patients 5 and 6. (Left) Controls (Right) CF patients.

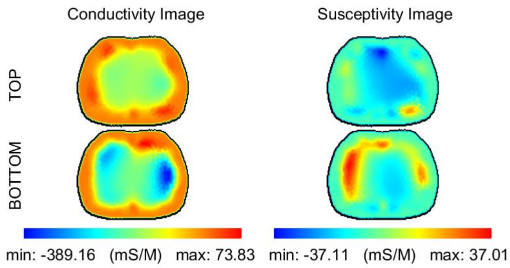

(a) Control 7.

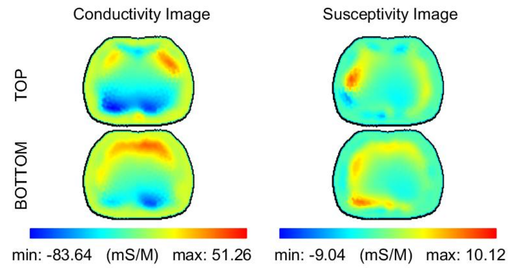

(b) CF patient 7.

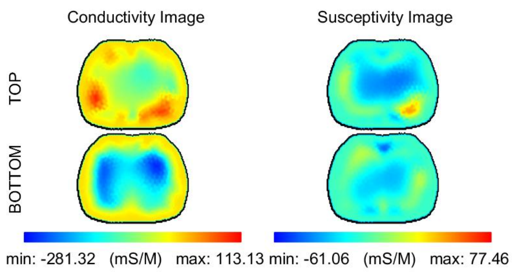

(c) Control 8.

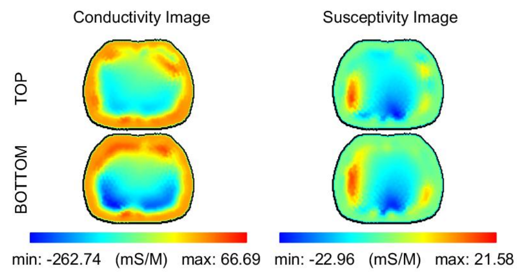

(d) CF patient 8.

Figure 4.52: EIT Ventilation Reconstructions on Controls 7 and 8, and CF patients 7 and 8. (Left) Controls (Right) CF patients.

4.6.2 Perfusion Reconstructions

Figures 4.53-4.56 show the pulsatile perfusion reconstruction snapshots at the end of the T-wave with reference frame at the end of the S-wave for the controls and CF patients, which are displayed in numbering number order. The conductivity images from CF patients have similar blood distribution during the peak of systole. This indicates that although CF patients 5-7 showed poorly ventilated lung regions, their pulmonary perfusion seems normal when compared to healthy controls.

The perfusion susceptivity images look better when compared to the ventilation susceptivity images for all controls and CF patients. Since the ventilation and perfusion images capture susceptivity changes caused to air and blood movement, respectively, it may indicates that different regularization strategies are needed when reconstructing susceptivity images as well as different operation frequencies.

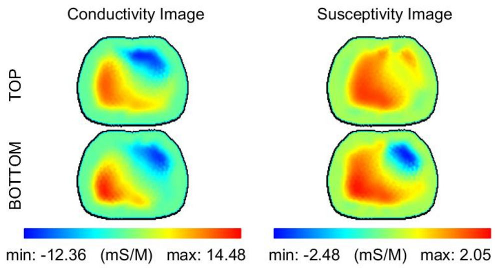

(a) Control 1.

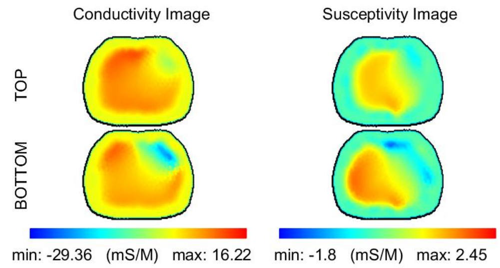

(b) CF patient 1.

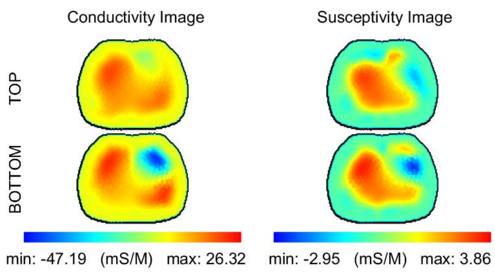

(c) Control 2.

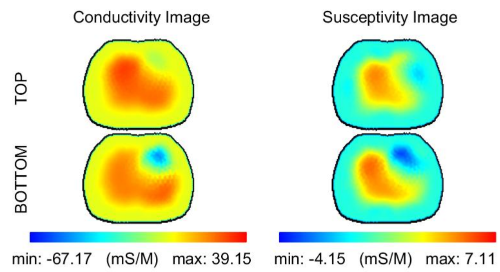

(d) CF patient 2.

Figure 4.53: EIT Perfusion Reconstructions on Controls 1 and 2, and CF patients 1 and 2. (Left) Controls (Right) CF patients.

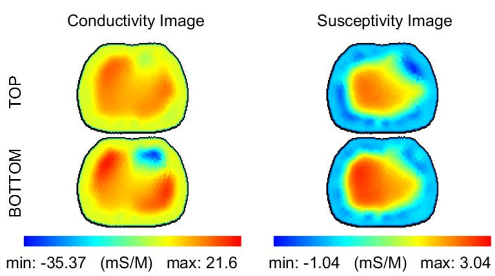

(a) Control 3.

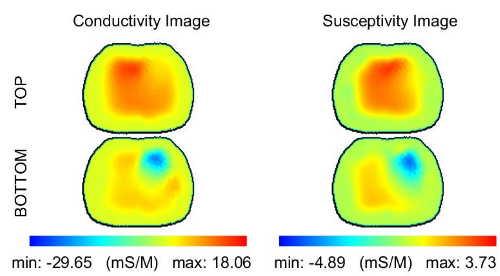

(b) CF patient 3.

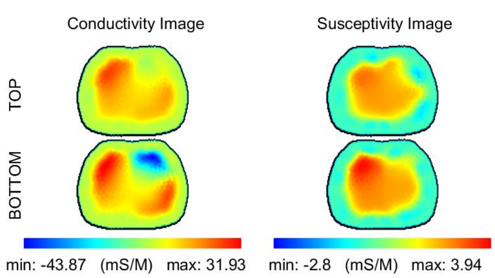

(c) Control 4.

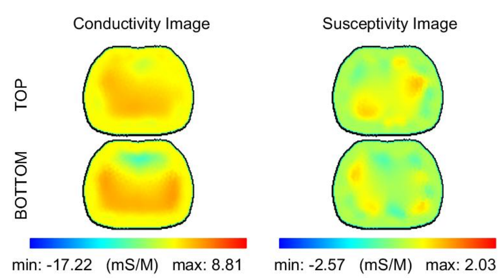

(d) CF patient 4.

Figure 4.54: EIT Perfusion Reconstructions on Controls 3 and 4, and CF patients 3 and 4. (Left) Controls (Right) CF patients.

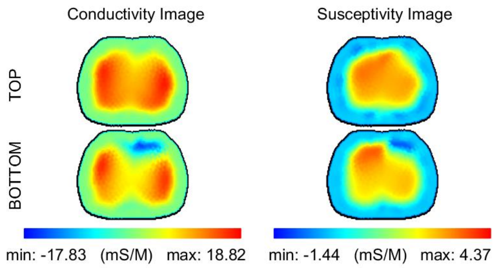

(a) Control 5.

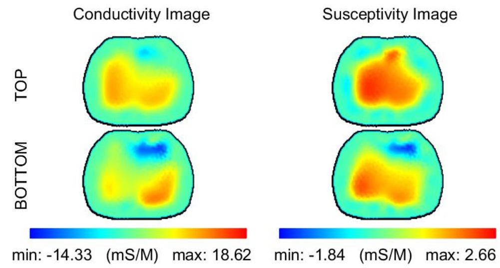

(b) CF patient 5.

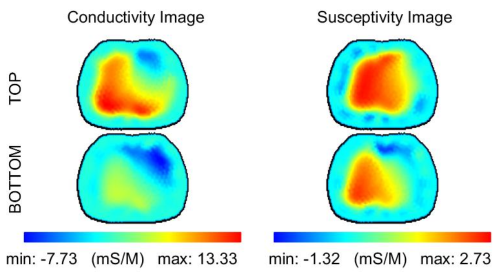

(c) Control 6.

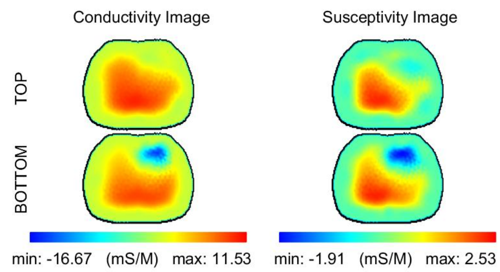

(d) CF patient 6.

Figure 4.55: EIT Perfusion Reconstructions on Controls 5 and 6, and CF patients 5 and 6. (Left) Controls (Right) CF patients.

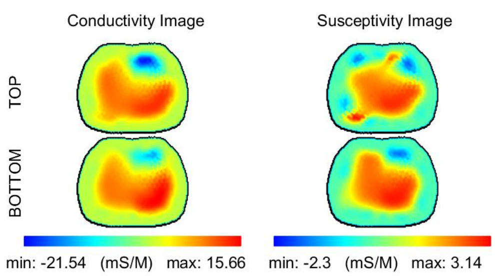

(a) Control 7.

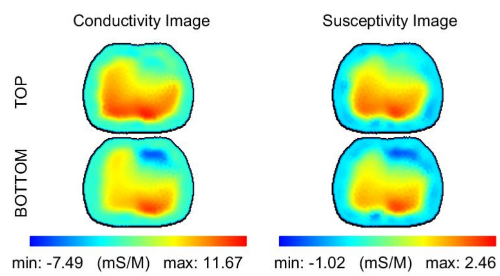

(b) CF patient 7.

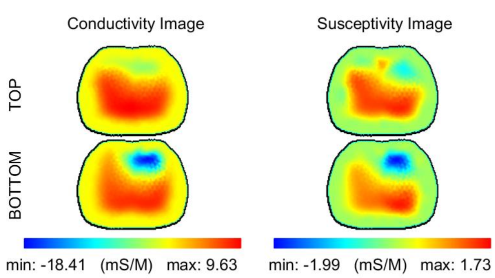

(c) Control 8.

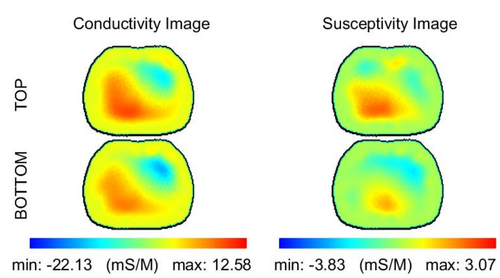

(d) CF patient 8.

Figure 4.56: EIT Perfusion Reconstructions on Controls 7 and 8, and CF patients 7 and 8. (Left) Controls (Right) CF patients.

The 3D EIT images show heterogeneity in ventilation distribution in patients with CF. The reconstructions from patient 1 are similar to those of the healthy controls, possibly indicating beneficial effectors of modulator therapy or lesser lung damage. Patient 2 presents more heterogeneity and variations between visits. Moreover, the PFTs for patient 1 showed higher values than for patient 2, which could indicate better lung function.

4.6.3 Longitudinal Analysis

20 patients with CF were imaged using the ACT5 EIT system over 3 years at Children's Hospital Colorado while healthy control subjects were imaged once. During data collection, subjects were sitting upright and asked to breathe normally for up to 5 minutes. During some visits, patients also performed pulmonary function tests (PFTs) and multiple breath washouts (MBWs).

CF causes difficulty breathing due to the mucus build-up in the lungs and bronchietatis, which directly affects the EIT ventilation reconstructions instead of the perfusion reconstructions. We can also see in the previous section that the perfusion reconstructions from CF patients and healthy controls were similar. For this reason, only ventilation reconstructions will be shown for multiple patient visits.

Figure 4.57 shows the 3D EIT ventilatory difference reconstructions at full inspiration with the reference at full expiration from a male patient (patient A) aged 17 year-old while Figure 4.58 shows the reconstructions from a female patient (patient B) aged 4 year-old. Patient A was imaged during 7 visits 12 weeks apart on average while on Cystic Fibrosis Transmembrane Conductance Regulator (CFTR) modulator therapy during all visits. This patient has CF genotype $F508del/2789+5G\>A$. patient B was imaged during 8 visits 10 weeks apart on average. This patient has CF genotype $F508del/G542X$ and started CFTR modulator therapy in visit 4 due to age restrictions.

We can see that the ventilation reconstructions of patient A show homogeneity for both upper and lower lungs for all visits. On the other hand, the ventilation reconstructions of patient B show more heterogeneity in visits 2, 5, 6, and 7 with more variations in ventilation distributions between visits. Moreover, Figure 4.59 shows the PFT and MBW results for each patient, and we can see that the PTF results for the male patient are higher than for the female patient while the MBW results are similar for both patients after visit 3.

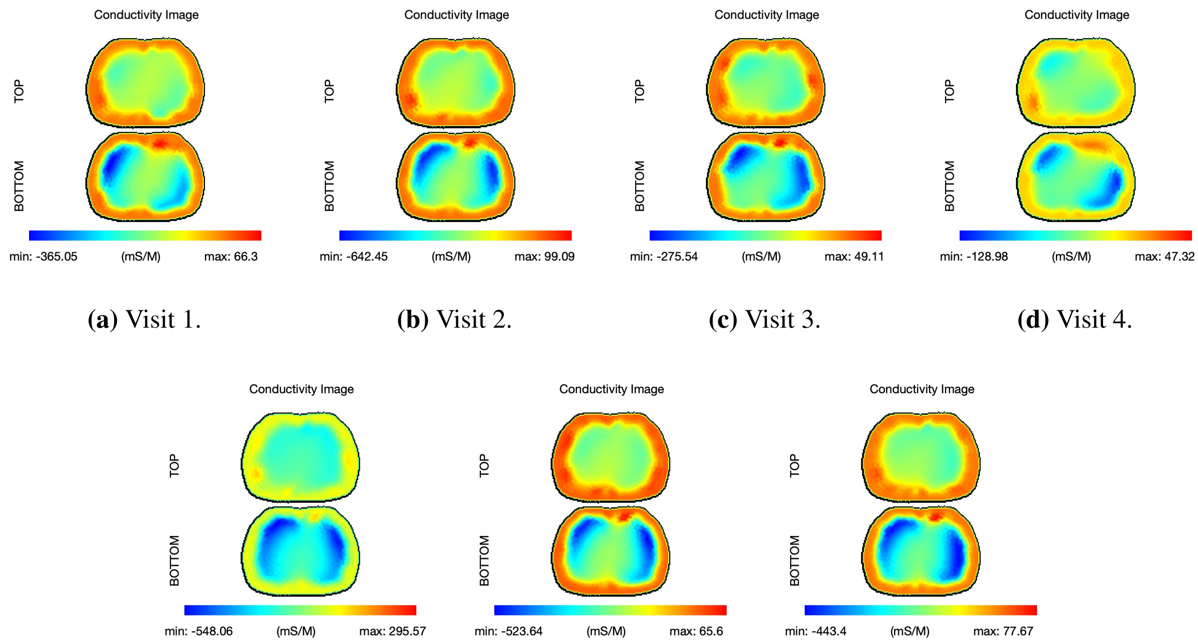

(a) Visit 1. **(b)** Visit 2. **(c)** Visit 3. **(d)** Visit 4.

(e) Visit 5. **(f)** Visit 6. **(g)** Visit 7.

Figure 4.57: 3D ventilation reconstructions at full inspiration for a 17-year-old male (Patient A) with CF genotype $F508del/2789 + 5G\> A$, from 7 visits 12 weeks apart on average. The patient was on CFTR modulator therapy during all visits.

3D EIT ventilation reconstructions can provide information about lung heterogeneity in ventilation distribution in patients with CF. The ventilation reconstructions of the male patient are similar to those of the healthy controls, as seen in the previous section, possibly indicating beneficial effects of CFTR modulator therapy or lesser lung damage over the years. The female patient presents more heterogeneity in the lungs and variations in ventilation distributions between visits, which could relate to the patient's condition during a given visit. Moreover, the PFTs for the male patient showed higher values than for the female patient, which could indicate better lung function as seen in the ventilation reconstructions.

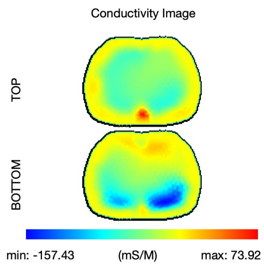

(a) Visit 1.

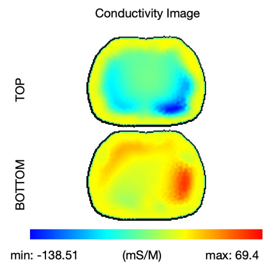

(b) Visit 2.

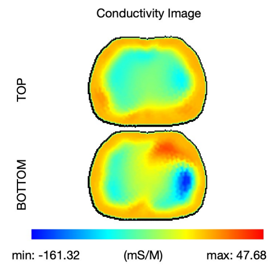

(c) Visit 3.

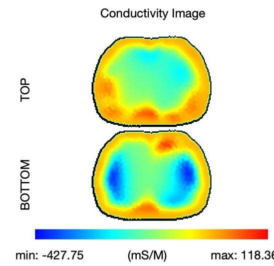

(d) Visit 4.

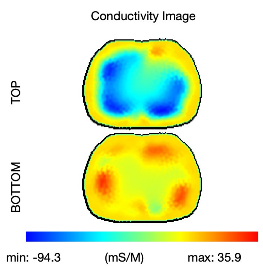

(e) Visit 5.

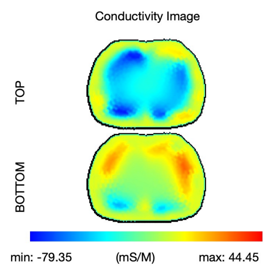

(f) Visit 6.

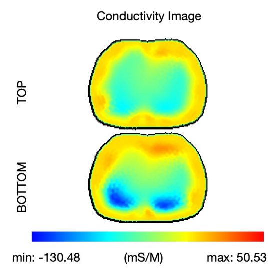

(g) Visit 7.

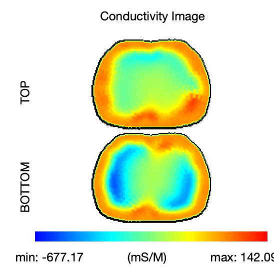

(h) Visit 7.

Figure 4.58: 3D ventilation reconstructions at full inspiration for a 4-year-old female (Patient B) with CF genotype $F508del/G542X$, from 8 visits 10 weeks apart on average. From (visit 1 - visit 3), the patient was ineligible for CRTR modulator therapy. From (visit 4 - visit 8), the patient received CRTR modulator therapy.

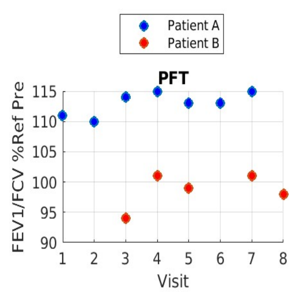

(a) PFT.

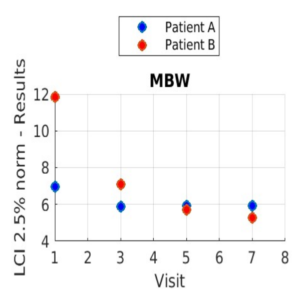

(b) MBW.

Figure 4.59: PFTs and MBWs from Patients A and B.

To date, this is the first longitudinal study using 3D EIT to monitor patients with CF worldwide. This could bring new insights into managing the effects of CF on individuals receiving CFTR modulator therapy, and for those who are ineligible for CFTR modulator therapy due to their specific genetic mutation.

4.7 EIT Reconstructions on PVS Patients

This section shows the ventilation and pulsatile perfusion images from a subset of eight controls aged $(8, \pm 2.5)$ years old and pre-cardiac intervention PVS patients aged $(3.3, \pm 2.8)$ years old using the 3D ToDLeR algorithm, and the ACT5 System. The data were collected at Children's Hospital Colorado in the Cath Lab.

A total of 32 electrodes arranged in 2 rows of 16 were placed around each subject's torso, and 3D trigonometric current patterns with amplitude $0.35\,\mathrm{mA}$ and frequency of $93.750\,\mathrm{kHz}$ were applied during the data collection at $27\,\mathrm{frames/sec}$. The PVS patients were sedated and mechanically ventilated, and the ventilation reconstructions were computed from data collected during tidal breathing while the perfusion reconstructions were computed from data collected during an induced breath-hold. Moreover, the same control group reconstructions and numbering from the CF patient result section are used for comparison.

4.7.1 Comparison versus healthy subjects

Figures 4.60-4.63 show the ventilation reconstruction snapshots at full inspiration with reference frame at full expiration for the controls and PVS patients, which are displayed in numbering order. PVS Patients 1, 3, 4, 5, and 6 show more anterior than posterior lung ventilated areas in the conductivity images. Since the patients are laying down in supine position, dorsal lung compression may occur, which causes the ventilation to be more towards the anterior lung regions.

PVS patients 2 and 7 show poorly ventilated left lung regions, which could result from PVS disease complications or previous lung disease such as BPD. The conductivity image from PVS

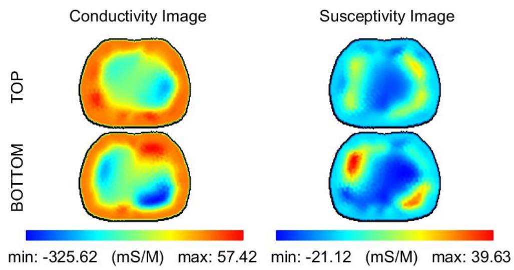

(a) Control 1.

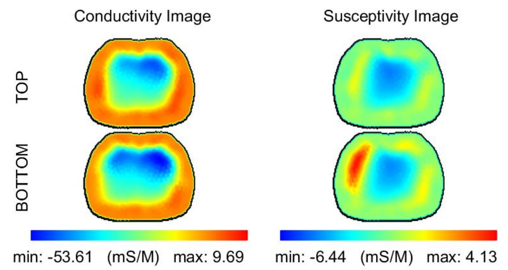

(b) PVS patient 1.

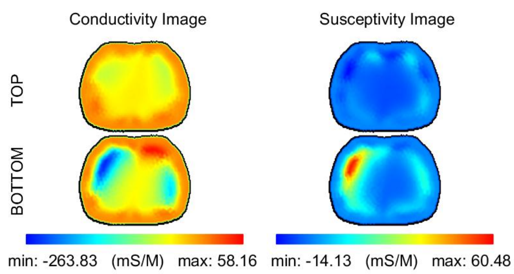

(c) Control 2.

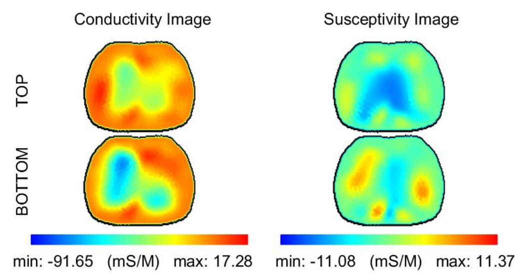

(d) PVS patient 2.

Figure 4.60: EIT Ventilation Reconstructions on Controls 1 and 2, and PVS patients 1 and 2. (Left) Controls (Right) PVS patients.

patient 6 show good right lower lung ventilation while the upper lung and left lower lung has smaller opening due to ventilation.

Since the controls were sitting upright during the data collection, the ventilation distribution in the conductivity images are more uniform throughout the lungs when compared to conductivity images computed from data in which the subject was laying down in supine position. Moreover, as we have seen before, the ventilation susceptivity images from PVS patients are poor when compared to the conductivity images.

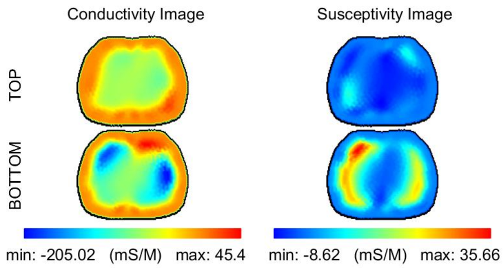

(a) Control 3.

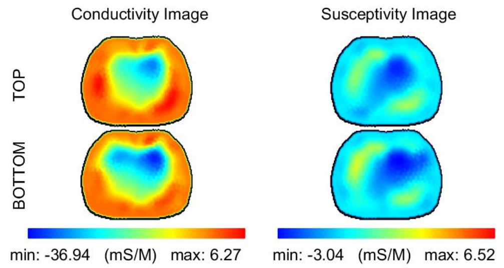

(b) PVS patient 3.

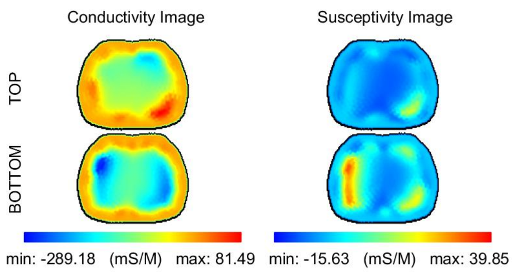

(c) Control 4.

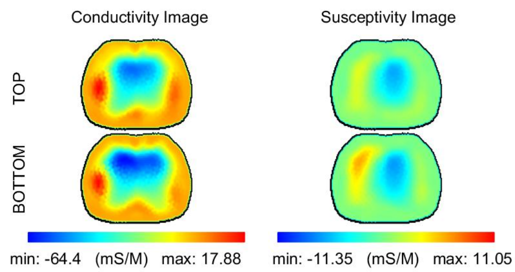

(d) PVS patient 4.

Figure 4.61: EIT Ventilation Reconstructions on Controls 3 and 4, and PVS patients 3 and 4. (Left) Controls (Right) PVS patients.

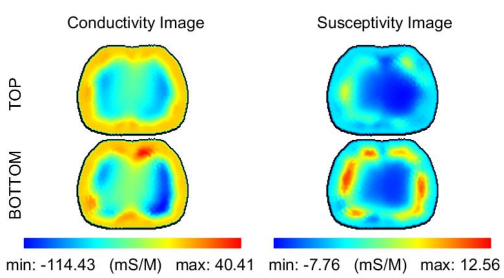

(a) Control 5.

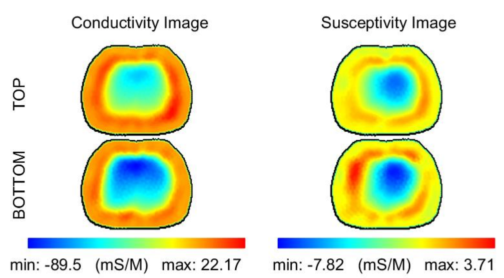

(b) PVS patient 5.

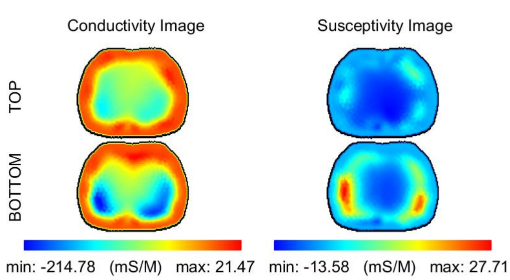

(c) Control 6.

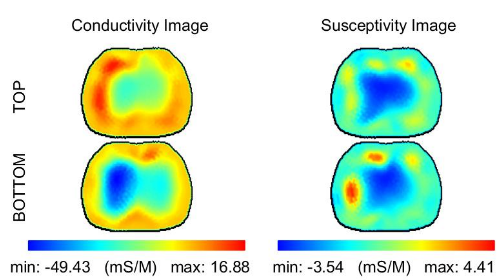

(d) PVS patient 6.

Figure 4.62: EIT Ventilation Reconstructions on Controls 5 and 6, and PVS patients 5 and 6. (Left) Controls (Right) PVS patients.

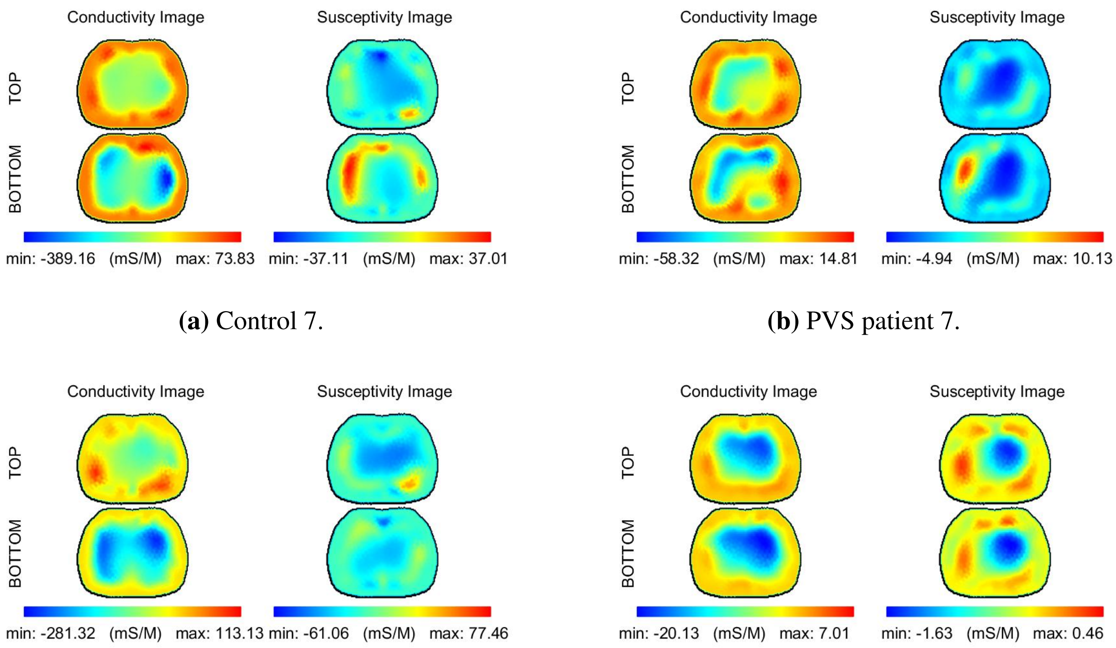

(a) Control 7.

(b) PVS patient 7.

(c) Control 8.

(d) PVS patient 8.

Figure 4.63: EIT Ventilation Reconstructions on Controls 7 and 8, and PVS patients 7 and 8. (Left) Controls (Right) PVS patients.

Figures 4.64-4.67 show the perfusion reconstruction snapshots at the end of the T-wave with reference frame at the end of the S-wave for the controls and PVS patients, which are displayed in numbering order. In general, the conductivity images from controls show more blood distribution homogeneity throughout the lungs when compared to the conductivity images from PVS patients.

PVS Patients 2 and 6 have small perfused areas in the left lower lung during peak of systole. Results from patients 1, 3, 7, and 8 do not show good contrast between the lungs and heart regions, which indicates smaller blood volume changes occurring in the lungs than in the heart. Since the PVS disease causes one or more pulmonary veins to get narrower or be completely occluded, this increases the pulmonary pressure but also reduces the amount of blood circulating in the lungs.

The conductivity images from PVS patients 4 and 5 show better blood distribution homogeneity in the lungs as well as contrast with the heart region. The perfusion susceptivity images from the PVS patients look better when compared to their ventilation susceptivity images. In addition, perfusion susceptivity images from the controls show better blood distribution homogeneity when

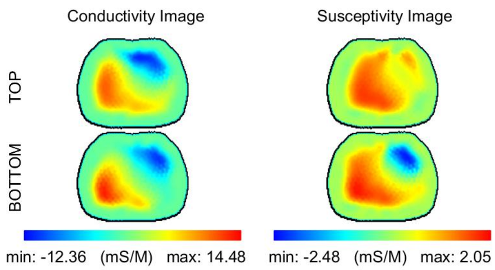

(**a**) Control 1.

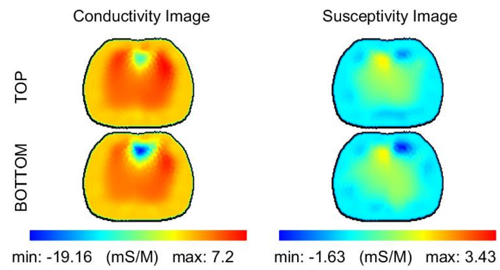

(**b**) PVS patient 1.

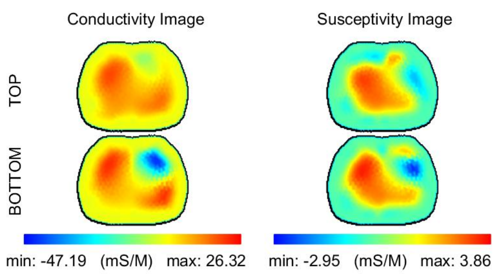

(**c**) Control 2.

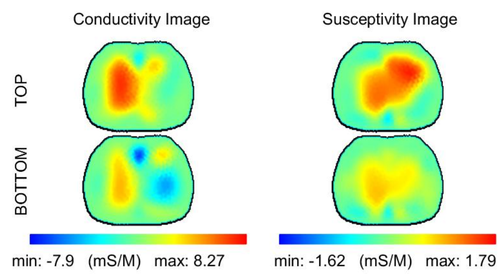

(**d**) PVS patient 2.

Figure 4.64: EIT Perfusion Reconstructions on Controls 1 and 2, and PVS patients 1 and 2. (Left) Controls (Right) PVS patients.

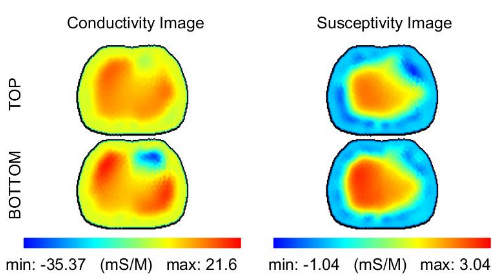

(**a**) Control 3.

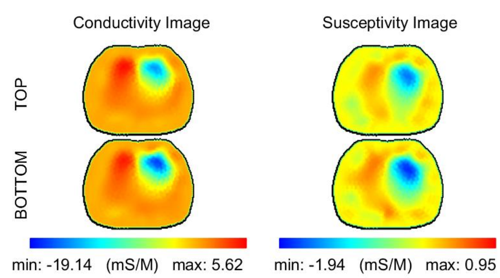

(**b**) PVS patient 3.

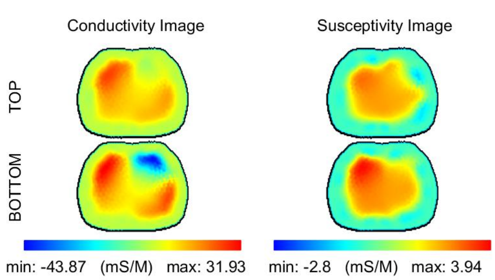

(**c**) Control 4.

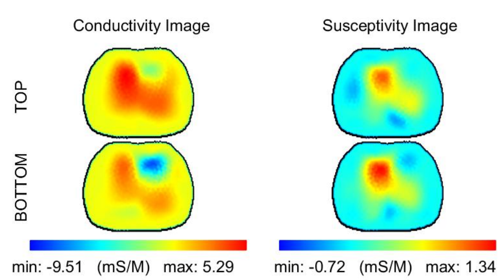

(**d**) PVS patient 4.

Figure 4.65: EIT Perfusion Reconstructions on Controls 3 and 4, and PVS patients 3 and 4. (Left) Controls (Right) PVS patients.

compared to the PVS patients. However, due to the high variability between ventilation and perfusion susceptivity images, further analysis and tests need to be done for better understanding of the susceptivity images.

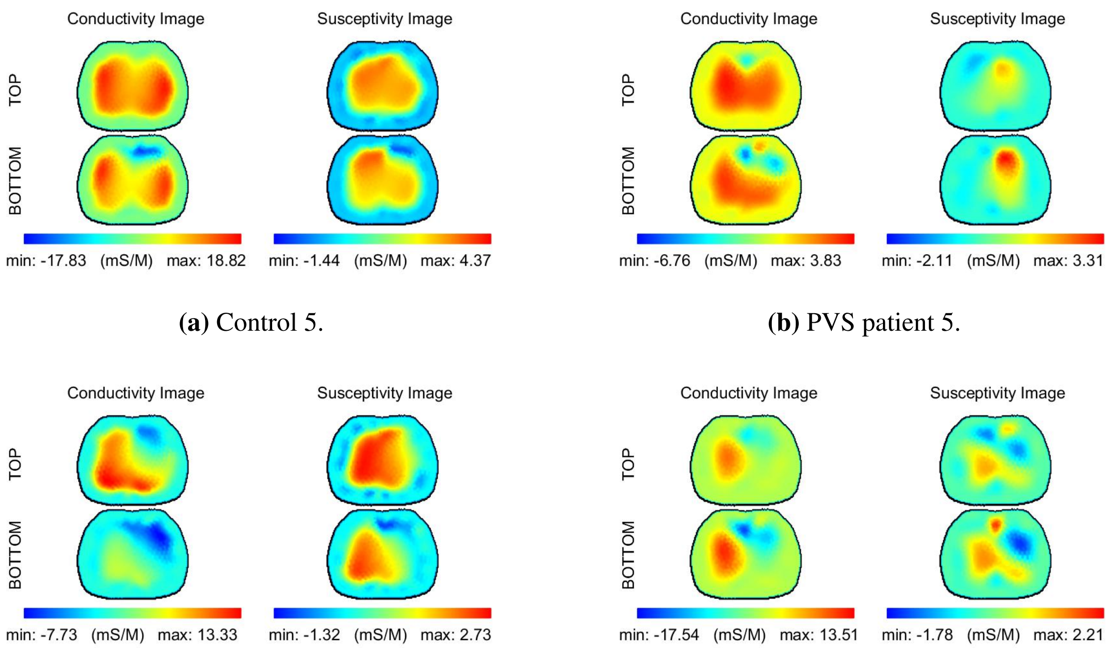

(a) Control 5.

(b) PVS patient 5.

(c) Control 6.

(d) PVS patient 6.

Figure 4.66: EIT Perfusion Reconstructions on Controls 5 and 6, and PVS patients 5 and 6. (Left) Controls (Right) PVS patients.

Overall, the perfusion conductivity images show regional lung changes and differences between PVS patients and controls, which could be a good indicator for blood volume changes in the lungs in PVS patients.

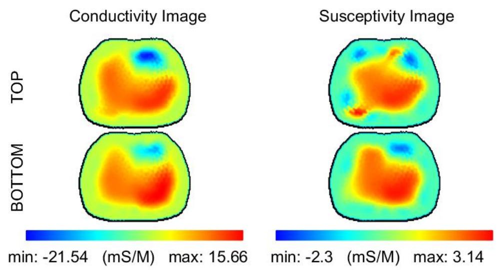

(a) Control 7.

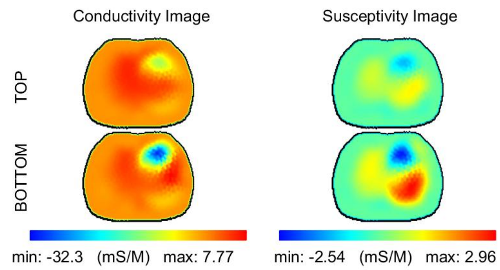

(b) PVS patient 7.

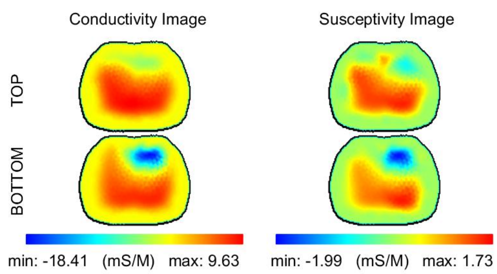

(c) Control 8.

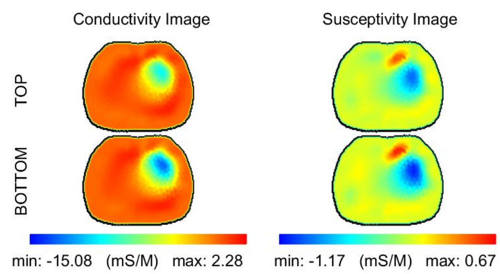

(d) PVS patient 8.

Figure 4.67: EIT Perfusion Reconstructions on Controls 7 and 8, and PVS patients 7 and 8. (Left) Controls (Right) PVS patients.

4.7.2 Pre/Post Cardiac Intervention Reconstructions

16 patients were enrolled to be imaged with the ACT5 system pre and post catheterization to insert a balloon stent [89]. Data were collected immediately before and after the procedure while the patients were still being mechanically ventilated. To evaluate the results and effects of the cardiac procedure, both ventilation and pulsatile perfusion data reconstructions were performed.

Figures 4.68-4.71 show the ventilation reconstructions pre and post cardiac intervention displayed on the same scale. Looking at the conductivity images of ventilation, we can see some small changes between pre and post cardiac intervention, which would be expected since the pulmonary veins are being intervened and it should not have a direct effect on the patient's lung aeration. The susceptivity images also show small changes, but these reconstructions still need more improvement for better interpretation.

Figure 4.72 shows the histograms of the global and regional conductivity distribution in the lungs for ventilation. The conductivity from each voxel for a given region was summed and then normalized by the global sum of conductivity values during pre cardiac procedure so that the normalized global conductivity is always one during pre cardiac procedure. The histograms helps identifying the relative changes between pre and post cardiac intervention. Moreover, the blue box in the right-upper corner shows which vein was intervened, including upper left vein (UL), lower left vein (LL), upper right vein (UR), middle right vein (MR), and lower right vein (LR).

The histograms for pre and post cardiac intervention also show small relative changes and ventilation as seen in the ventilation reconstructions. PVS patients 3 and 8 show higher relative changes compared to other patients with both global changes increasing after the cardiac intervention. Both patients had at least 3 veins intervened.

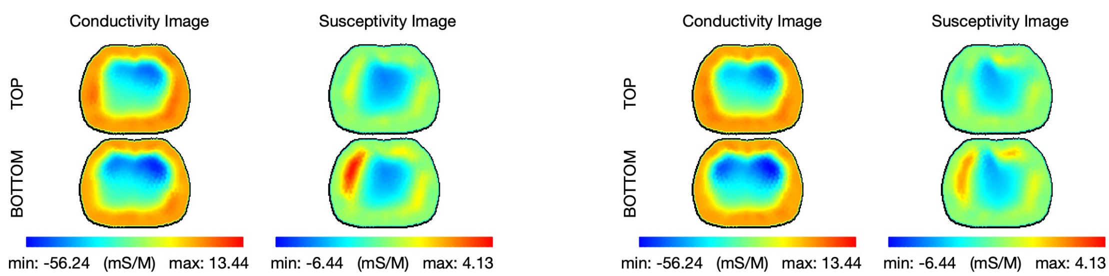

(a) PVS patient 1.

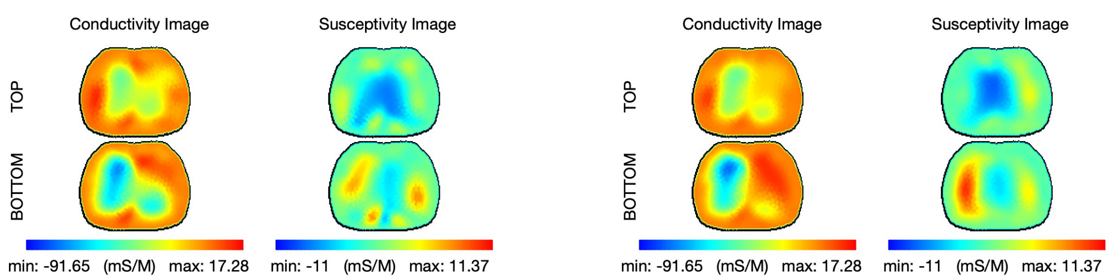

(b) PVS patient 2.

Figure 4.68: EIT Ventilation Reconstructions of PVS patients 1 and 2. (Left) pre and (Right) post cardiac intervention.

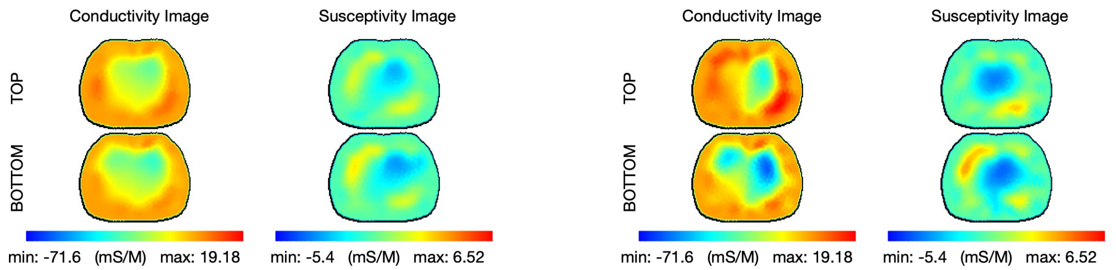

(a) PVS patient 3.

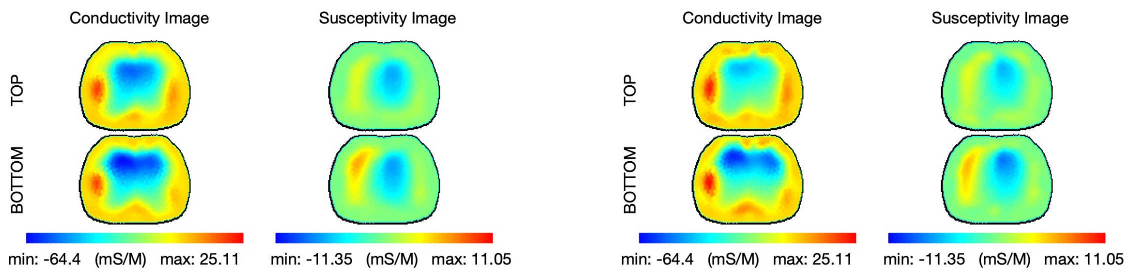

(b) PVS patient 4.

Figure 4.69: EIT Ventilation Reconstructions of PVS patients 3 and 4. (Left) pre and (Right) post cardiac intervention.

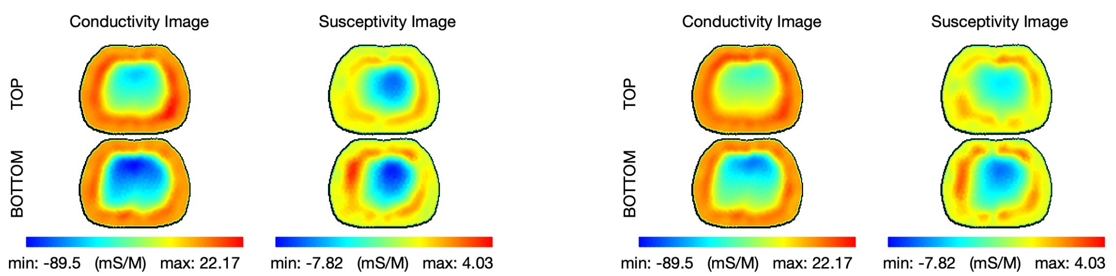

(a) PVS patient 5.

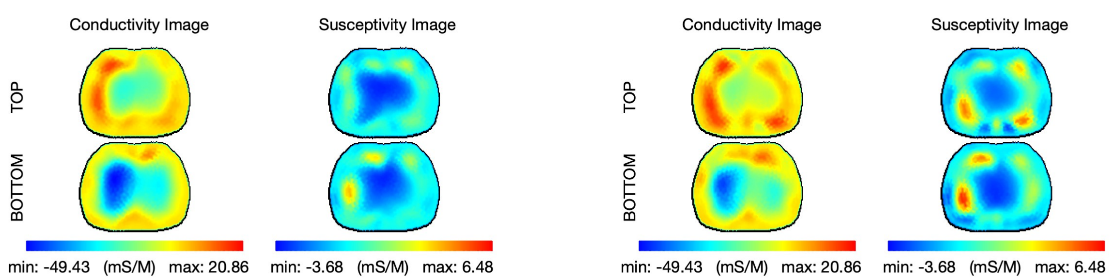

(b) PVS patient 6.

Figure 4.70: EIT Ventilation Reconstructions of PVS patients 5 and 6. (Left) pre and (Right) post cardiac intervention.

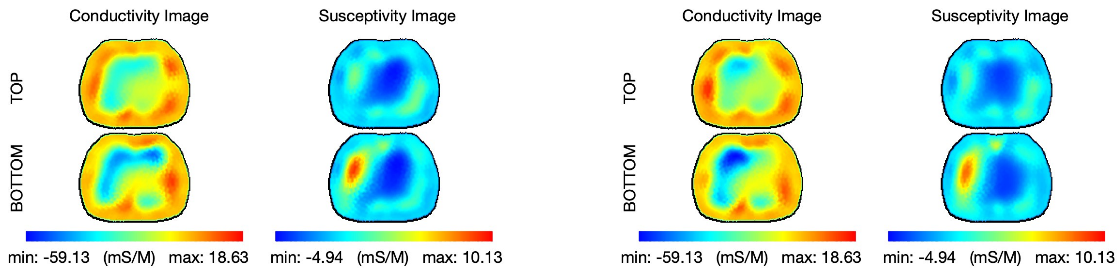

(a) PVS patient 7.

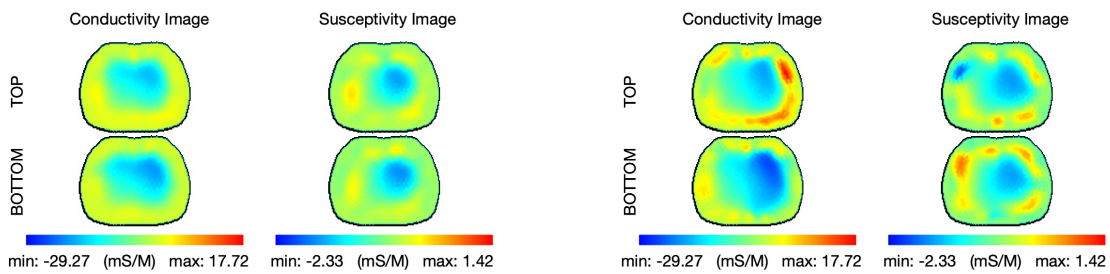

(b) PVS patient 8.

Figure 4.71: EIT Ventilation Reconstructions of PVS patients 7 and 8. (Left) pre and (Right) post cardiac intervention.

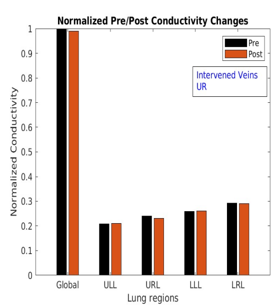

(a) PVS patient 1.

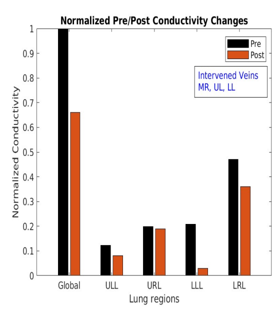

(b) PVS patient 2.

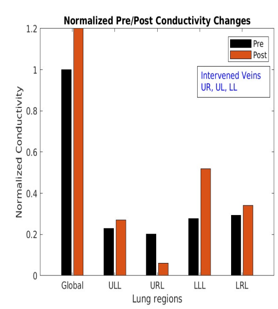

(c) PVS patient 3.

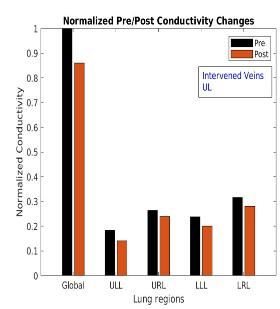

(d) PVS patient 4.

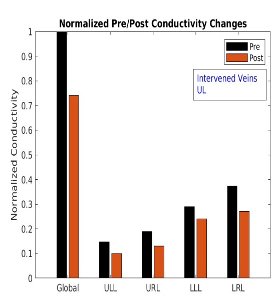

(e) PVS patient 5.

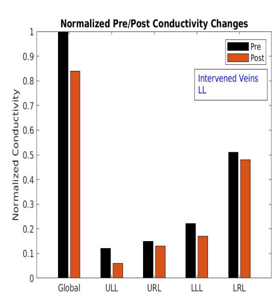

(f) PVS patient 6.

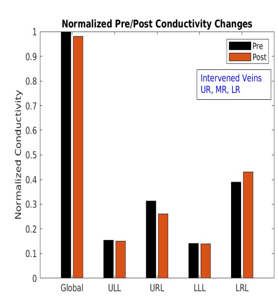

(g) PVS patient 7.

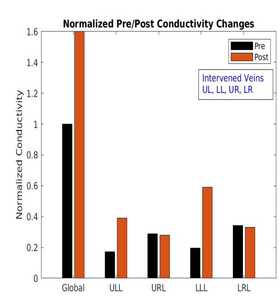

(h) PVS patient 8.

Figure 4.72: Histograms of ventilation distribution for pre and post cardiac intervention.

Figures 4.73-4.75 show the pulsatile perfusion reconstruction during pre and post cardiac intervention displayed on the same scale. The pulsatile perfusion reconstructions also show small changes between pre and post cardiac intervention as seen in the ventilation reconstructions. The changes in the bottom reconstructions are more noticeable than in the top reconstructions, and it could be a result of the top row of electrode placement. Moreover, the susceptivity images also show small changes when comparing pre and post cardiac intervention.

Figure 4.77 shows the histograms of the global and regional conductivity distribution in the lungs at peak of systole. Overall, there are small changes between pre and post cardiac intervention for all patients, except for PVS patients 2 and 7. For both patients, we can see that LLL region contributions negatively to the global volume of blood at peak of systole during post cardiac intervention. This means that the blood flow in the LLL region is in phase with the heart blood flow so that when the ventricles are filling, the blood is moving to the LLL region as well. This is the opposite of what is expected during pulmonary perfusion where the blood volume in the lungs decreases during diastole (ventricle filling) and increases during systole (ventricle emptying). This could relate to the patient's condition related to the effects of PVS in the lungs.

Figures 4.78-4.79 shows the correlation plots of all voxels with a voxel chosen manually from the heart region in the reconstructions from pre and post cardiac intervention. These plots help visualize which voxels are in or out of phase with the heart voxels. During pulmonary perfusion, the voxels from lung regions should be out of phase from the heart voxels because of the blood flow moving in and out of heart and lungs. We can see that for patients 2 and 7, there are more regions towards the LLL that are in phase with the heart voxels. This confirms the out-of-phase effects seen in the histograms from both patients.

Overall, the pulsatile perfusion EIT reconstructions can provide regional information about the blood distribution in the lungs during the cardiac cycle. Moreover, changes in conductivity can be detected in the histogram plots as well as in the correlation plots.

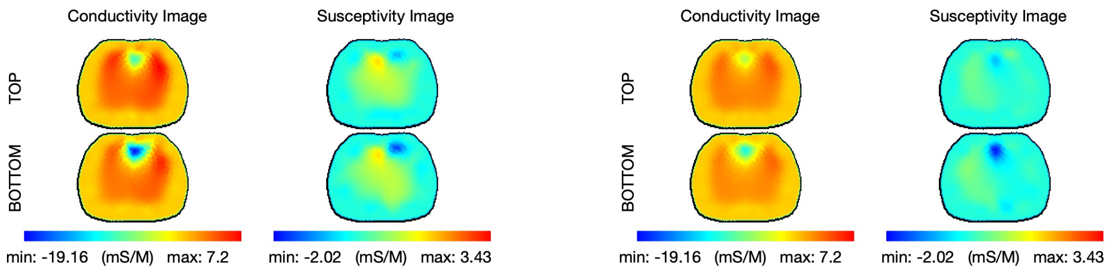

(a) PVS patient 1.

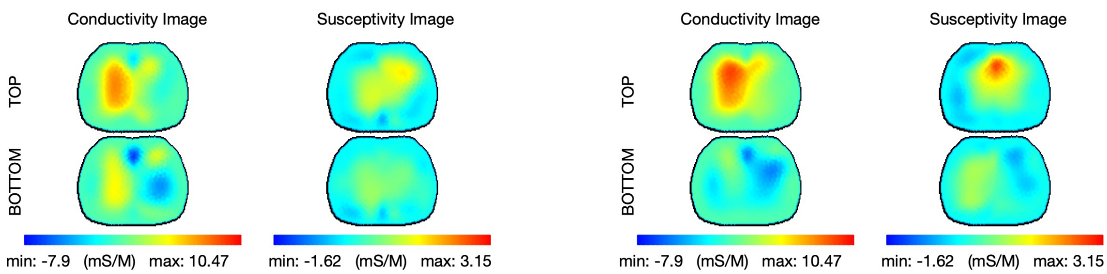

(b) PVS patient 2.

Figure 4.73: EIT Perfusion Reconstructions of PVS patients 1 and 2. (Left) pre and (Right) post cardiac intervention.

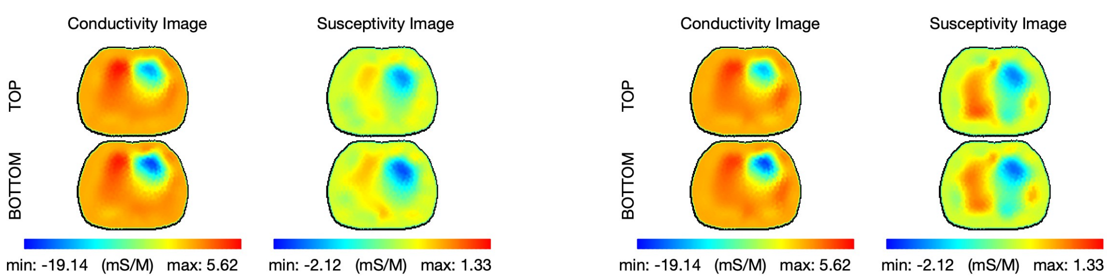

(a) PVS patient 3.

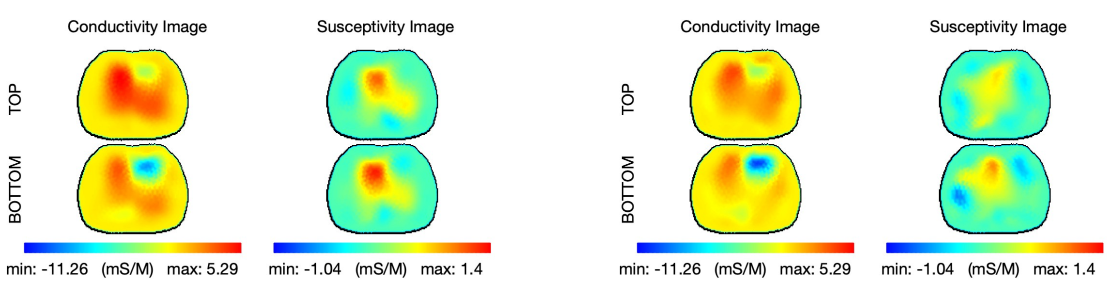

(b) PVS patient 4.

Figure 4.74: EIT Perfusion Reconstructions of PVS patients 3 and 4. (Left) pre and (Right) post cardiac intervention.

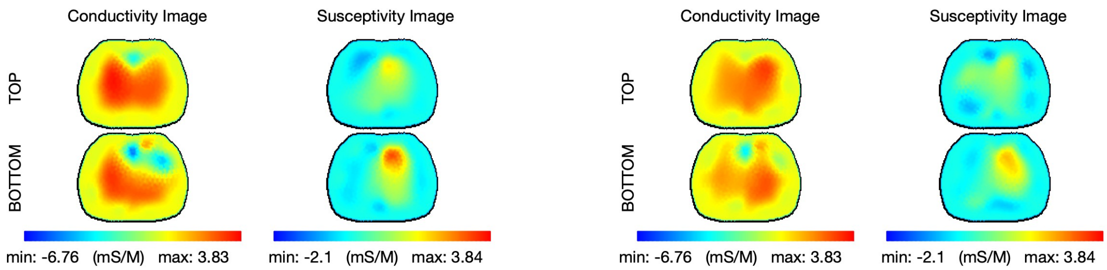

(a) PVS patient 5.

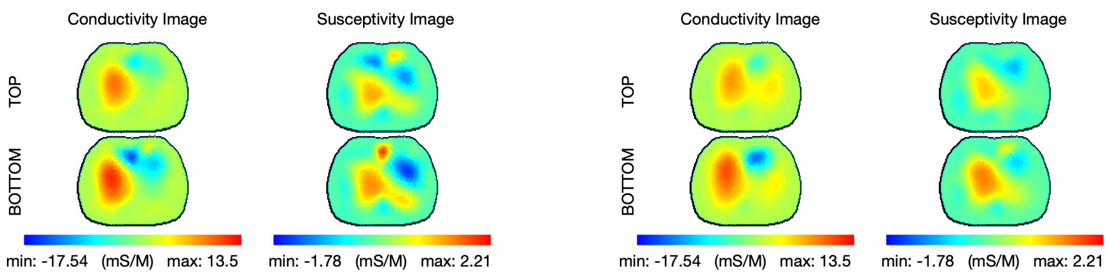

(b) PVS patient 6.

Figure 4.75: EIT Perfusion Reconstructions of PVS patients 5 and 6. (Left) pre and (Right) post cardiac intervention.

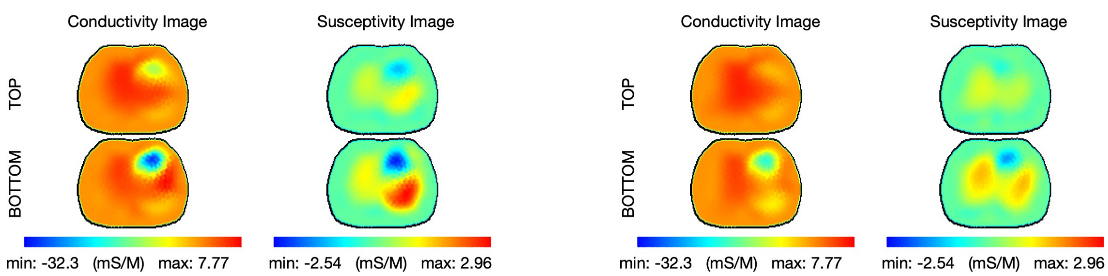

(a) PVS patient 7.

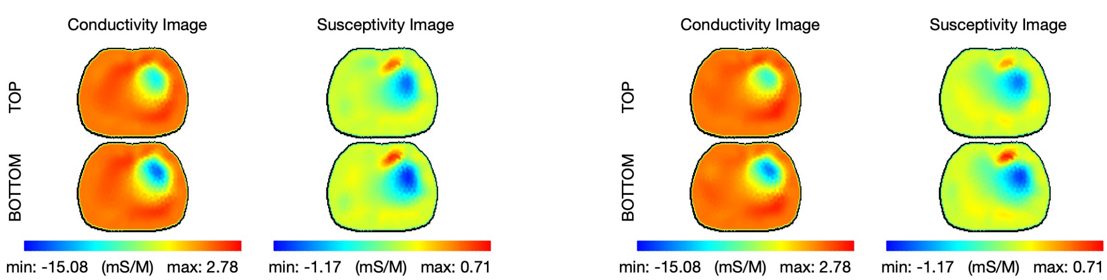

(b) PVS patient 8.

Figure 4.76: EIT Perfusion Reconstructions of PVS patients 7 and 8. (Left) pre and (Right) post cardiac intervention.

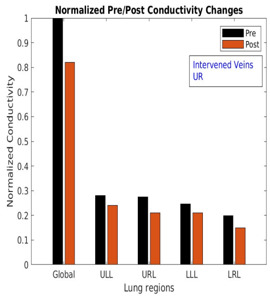

(a) PVS patient 1.

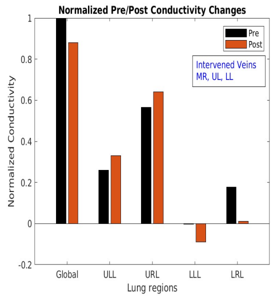

(b) PVS patient 2.

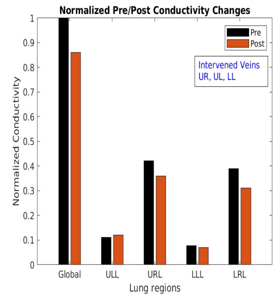

(c) PVS patient 3.

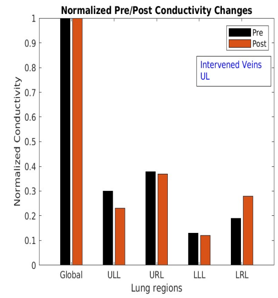

(d) PVS patient 4.

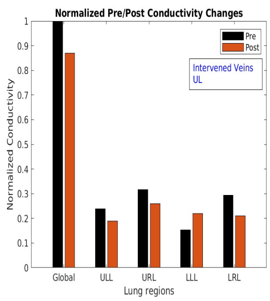

(e) PVS patient 5.

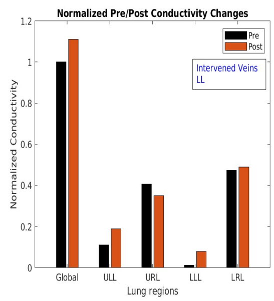

(f) PVS patient 6.

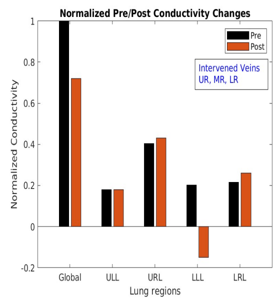

(g) PVS patient 7.

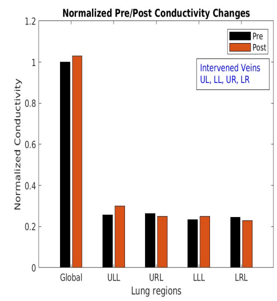

(h) PVS patient 8.

Figure 4.77: Histograms of perfusion distribution for pre and post cardiac intervention.

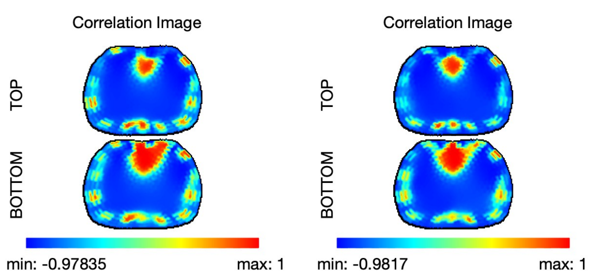

(a) PVS patient 1.

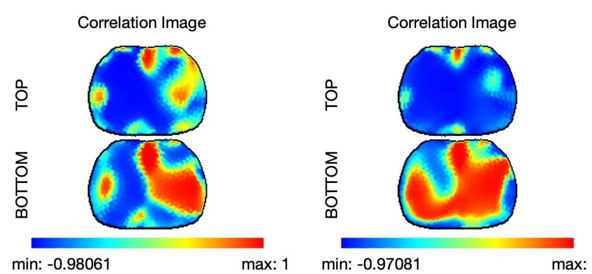

(b) PVS patient 2.

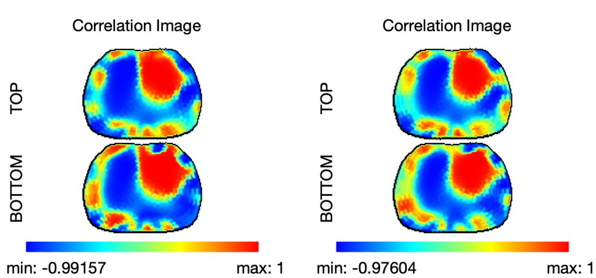

(c) PVS patient 3.

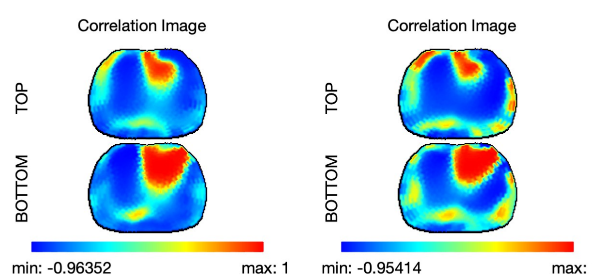

(d) PVS patient 4.

Figure 4.78: Correlation plots for perfusion reconstruction of PVS patients 1, 2, 3, and 4.

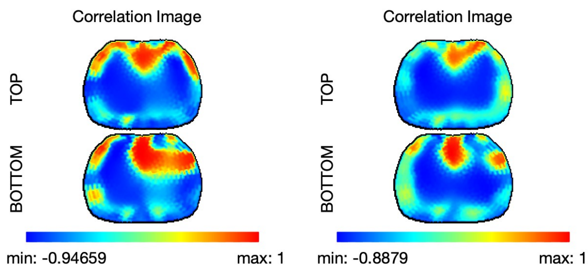

(a) PVS patient 5.

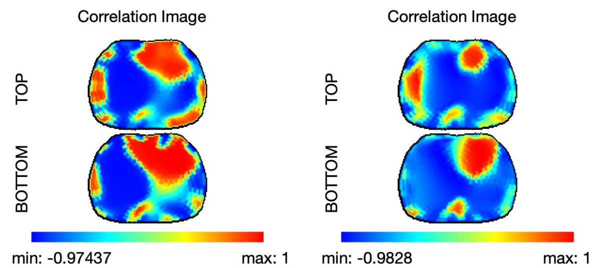

(b) PVS patient 6.

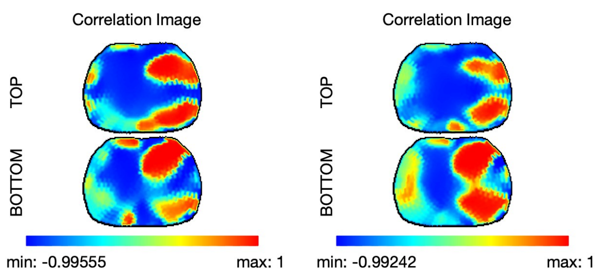

(c) PVS patient 7.

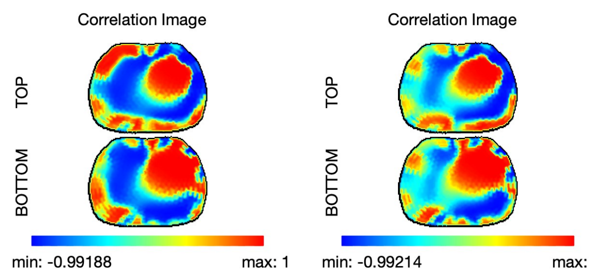

(d) PVS patient 8.

Figure 4.79: Correlation plots for perfusion reconstruction of PVS patients 5, 6, 7, and 8.

Chapter 5

Conclusion

This dissertation has introduced the design of a user-friendly clinical interface along with the real-time implementations of NOSER and ToDLeR reconstruction algorithms for the ACT5 system, which is a highly flexible EIT system for monitoring cardiac and lung function. Additionally, the digital filters provide the ability to simultaneously filter and display the ECG and EIT signals, which is novel in the field of EIT, with detailed timing information for interpreting the cardiac portion of the EIT signal and the pulsatile perfusion reconstructions.

Both NOSER and ToDLeR algorithms were tested with EIT data collected on 2D and 3D tanks. The NOSER and ToDLeR reconstruction from tank data showed similar results for both conductivity and susceptivity images. Moreover, the 2D ToDLeR forward solution was able to better estimate the conductivity of the saline solution than the NOSER forward solution when the saline volume exceeded the electrode height. The 2D ToDLeR conductivity reconstructions also show better spatial resolution when compared with the NOSER conductivity reconstructions using the same human subject data sets. The susceptivity reconstructions did not provide good reconstructions for some cases, and it is hypothesized that these may need different regularization strategies.

The ventilation and pulsatile perfusion conductivity reconstructions show the differences in the lung structures and function with the 3D EIT reconstructions providing more information about the region of interest using the same number of electrodes as in the 2D EIT reconstructions. In addition, EIT conductivity reconstructions show good agreement with radiology reports, X-ray and CT scans, as well as differences in ventilation and pulsatile perfusion images between healthy controls and patients.

Statistical results did not show difference between patients with ARDS prior to and on a spontaneous breathing test. However, this could be related to the small number of patients. On the other hand, GI values were significantly higher to patients with BPD when compared to healthy babies. This shows that EIT-derived measures may provide insights to the patient's conditions.

EIT reconstructions of longitudinal studies were performed for the CF and BPD studies. Differences in ventilation and pulsatile perfusion reconstructions were observed in both studies in patients with different disease progression. EIT reconstructions may provide more information about the patient's condition without exposure to radiation from X-ray and CT scans.

Patients with PVS were imaged pre and post catheterization. The EIT reconstructions showed differences in lung perfusion in patients with PVS when compared to healthy subjects. In addition, differences in the distributions of perfusion in the lungs were also noticed in the EIT reconstructions. EIT may provide more information to doctors as to when another catheterization should be performed.

5.1 Future Work

5.1.1 Belt Development

One of the critical parts when collecting EIT data is the placement of the electrodes. Bad electrode attachment can cause artifacts in reconstruction images. In addition, placing 32 electrodes takes between 10 to 15 minutes, or even more depending on if the patient is being imaged in the intensive care unit. A belt for the ACT5 system would decrease the time for electrode placement, and improve the electrode attachment to the patient.

5.1.2 Machine Learning Models

Machine learning has been used in EIT applications to improve EIT reconstructions. Machine learning models can be used create *a priori* information from other imaging techniques such as CT and MRI. Including machine learning strategies in the forward and inverse problem solutions may improve static EIT reconstructions generated by iterative EIT methods.

5.1.3 Inverse Problem Algorithms

This dissertation showed two EIT reconstruction algorithms, NOSER and ToDLeR. There are other algorithms that can also be implemented to run in real-time such as Gauss-Newton, Kaczmarz, and D-bar. Using different algorithms to reconstruct the ACT5 datasets may provide more insight about the EIT reconstructions as well as improvements to model the EIT problem.

5.1.4 NOSER and ToDLeR Mesh Modifications

NOSER and ToDLeR algorithms use the Joshua tree mesh to solve the forward and inverse EIT problems. However, the Joshua tree mesh has been used to discretize circular and cylindrical domains. Although it has been shown as a good approximation to reconstruct datasets collected on human subjects, the EIT inverse problem is more ill-posed when reconstructing data from human subjects using circular and cylindrical domains. Modifying the NOSER and ToDLeR algorithms to use meshes created from a human chest shape may provide better images.

5.1.5 ECG inverse problem

The ACT5 system can measure ECG simultaneously while collecting EIT data. The ECG collected on all electrodes can be used to solve the ECG inverse problem. This can provide information about where the heart is located, which can be used to improve EIT image segmentation. Better EIT segmentation can lead to more consistent EIT-derived measure computations because segmenting the lung regions is a challenge in EIT.

5.2 Contributions

List of contributions during the doctoral research:

- Optimized the reconstruction algorithms to run in real-time.
- Implemented the conformal map technique for chest-shaped reconstruction display when using the NOSER and ToDLeR algorithms.
- Developed the clinical user interface for the ACT5 system that runs on Windows and macOS.

- Implemented the digital filters to separate the ECG and EIT signals.
- Provided training and assistance to the teams at the University of Colorado Anschutz Medical Campus and Children's Hospital Colorado.
- Provided maintenance to the ACT5 system and GE GENESIS system.
- Participated in the data collection on premature babies and PVS patients for almost all visits.

List of the publications related to the doctoral research:

[1] N. Barbosa da Rosa Junior, J. Mueller, A. V. Pigatto, T.-J. Kao, N. Stoffel, C. Bromirski, D. Davenport, P. Offner, and E. Burnham. Ventilation Volume of Mechanically Ventilated Patients from EIT Data on a Novel Electrode Solution : A Case Study. *International Journal of Bioelectromagnetism*, 24:311, 2022.

[2] N. Barbosa da Rosa Junior, A. V. Pigatto, T.-J. Kao, N. Stoffel, C. Bromirski, D. Davenport, P. Offner, E. Burnham, and J. L. Mueller. EIT-derived measures of pulmonary health from 3-D reconstructions in mechanically ventilated ARDS patients. *AIP Conf. Proc.*, 2947(1), 2023.

[3] N. B. D. Rosa, J. Brinton, A. V. Pigatto, T.-J. Kao, P. Offner, J. Mueller, and E. Burnham. Assessment of Ventilatory Heterogeneity by Measures Derived From 3D Functional Electrical Impedance Imaging of Patients With Acute Respiratory Distress Syndrome and Healthy Controls: A Pilot Study (abstract). *Am J Respir Crit Care Med*, 207:A4719, 2023.

[4] O. R. Shishvan, A. Abdelwahab, N. B. da Rosa, G. J. Saulnier, J. L. Mueller, J. C. Newell, and D. Isaacson. ACT5 Electrical Impedance Tomography System. *IEEE Transactions on Biomedical Engineering*, 71(1):227–236, 2024.

[5] K. Shin, S. Ahmad, T. B. R. Santos, N. B. da Rosa Junior, and J. L. Mueller. Comparison of Two Linearization-Based Methods for 3-D EIT Reconstructions on a Simulated Chest. *J Math Imaging Vis*, 66:185–197, 2024.

[6] N. B. D. R. Junior, C. Vargas-Acevedo, O. R. Shishvan, G. Saulnier, J. Newell, D. Isaacson, J. Mueller, and J. Zablah. Evaluation of Blood Volume Changes in the Lung Using EIT Pre and Post Catheterization in Pediatric Patients With Pulmonary Vein Stenosis (abstract). *Am J Respir Crit Care Med*, 209:A6026, 2024.

[7] N. B. D. R. Junior, O. R. Shishvan, G. Saulnier, J. Newell, D. Isaacson, A. Keck, E. DeBoer, J. Hoppe, and J. Mueller. EIT Images of Ventilation and Perfusion Correlate With Spirometry in Patients With Cystic Fibrosis and Healthy Controls (abstract). *Am J Respir Crit Care Med*, 209:A6464, 2024.

[8] K. Enzer, N. B. D. R. Junior, A. Keck, E. Hagopian, J. Brinton, O. R. Shishvan, G. Saulnier, J. Newell, D. Isaacson, J. Mueller, and C. Baker. Longitudinal Characterization of Ventilation and Perfusion in Infants With Bronchopulmonary Dysplasia Using Electrical Impedance Tomography (abstract). *Am J Respir Crit Care Med*, 209:A5161, 2024.

[9] G. J. Saulnier, A. Abdelwahab, O. R. Shishvan, and N. B. da Rosa Junior. (Pending Patent Application) Simultaneous Acquisition of EIT and ECG Signals with the ACT 5 System. Serial Number: 63/667,278. July 2024.

[10] A. Abdelwahab, N. B. da Rosa, C. Wilcox, O. R. Shishvan, D. Isaacson, J. C. Newell, J. L. Mueller, and G. J. Saulnier. Simultaneous Acquisition of EIT and ECG Signals on Active EIT Electrodes. *IEEE Transactions on Biomedical Engineering*:1–11, 2024.

[11] K. Howard, C. Rocheleau, T. Overton, J. B. Nava, M. Faldet, K. Moen, S. Soller, T. Stephens, E. van de Lagemaat, N. Wijesinghe, K. W. Dolloff, N. B. da Rosa, and J. L. Mueller. A comparison of techniques to improve pulmonary EIT image resolution using a database of simulated EIT images. *Journal of Computational and Applied Mathematics*:116415, 2024. ISSN: 0377-0427.

[12] N. Barbosa da Rosa Junior, T.-J. Kao, J. Briton, P. Offner, E. Burnham, and J. L. Mueller. Three-dimensional electrical impedance imaging during spontaneous breathing trials in pa-

tients with acute hypoxic respiratory failure: A pilot study. *Critical care explorations*, 7(1): e1198, 2025.

[13] J. E. Zablah, C. Vargas-Acevedo, N. B. da Rosa Jr, O. R. Shishvan, G. Saulnier, D. Isaacson, G. J. Morgan, and J. L. Mueller. Feasibility of Electric Impedance Tomography in the Assessment of Lung Perfusion and Ventilation in Congenital Pulmonary Vein Stenosis (Accepted). *Pediatric Cardiology*, 2025.

Bibliography

[1] S. Mansouri, Y. Alharbi, F. Haddad, S. Chabcoub, A. Alshrouf, and A. Abd-Elghany. Electrical Impedance tomography - recent applications and developments. *J Electr Bioimp*, 12(50-62), 2021.

[2] K. Y. Aristovich, B. C. Packham, H. Koo, G. S. dos Santos, A. McEvoy, and D. S. Holder. Imaging fast electrical activity in the brain with electrical impedance tomography. *NeuroImage*, 124:204–213, 2016. ISSN: 1053-8119.

[3] C. Putensen, B. Hentze, S. Muenster, and T. Muders. Electrical Impedance Tomography for Cardio-Pulmonary Monitoring. *Journal of Clinical Medicine*, 8(8), 2019. ISSN: 2077-0383.

[4] Z. Zhao, K. Möller, D. Steinmann, I. Frerichs, and J. Guttmann. Evaluation of an electrical impedance tomography-based global inhomogeneity index for pulmonary ventilation distribution. *Intensive Care Medicine*, 35:1900–1906, 2009.

[5] M. C. Bachmann, C. Morais, G. Bugedo, A. Bruhn, J. B. B. Arturo Morales, E. Costa, and J. Retamal. Electrical impedance tomography in acute respiratory distress syndrome. *Critical Care*, 22(263), 2018.

[6] Y. Zou and Z. Guo. A review of electrical impedance techniques for breast cancer detection. *Medical Engineering and Physics*, 25(2):79–90, 2003. ISSN: 1350-4533.

[7] Z. R. Gatabi, M. Mirhoseini, N. Khajeali, I. R. Gatabi, M. Dabbaghianamiri, and S. Dorri. The Accuracy of Electrical Impedance Tomography for Breast Cancer Detection: A Systematic Review and Meta-Analysis. *The Breast Journal*, 2022.

[8] R. S. Blue. Teal-Time Three-Dimentional Electrical Impedance Tomography. PhD thesis. Department of Biomedical Engineering, Rensselaer Polytechnic Institute, Troy, NY, 1997.

[9] V. Tomicic and R. Cornejo. Lung monitoring with electrical impedance tomography: technical considerations and clinical applications. *J Thorac Dis*:11(7):3122–3135, 2019.

[10] J. L. Mueller, D. Isaacson, and J. C. Newell. Reconstruction of conductivity changes due to ventilation and perfusion from EIT data collected on a rectangular electrode array. *Physiological Measurement*, 22(1):97, 2001.

[11] M. M. Mellenthin, J. L. Mueller, E. D. L. B. de Camargo, F. S. de Moura, T. B. R. Santos, R. G. Lima, S. J. Hamilton, P. A. Muller, and M. Alsaker. The ACE1 Electrical Impedance Tomography System for Thoracic Imaging. *IEEE Transactions on Instrumentation and Measurement*, 68(9):3137–3150, 2019.

[12] E. Eisenhuber, C. M. Schaefer-Prokop, H. Prosch, and W. Schima. Bedside Chest Radiography. *Respiratory Care*:57(3) 427–443, 2012.

[13] E. Teschner, M. Imhoff, and S. Leonhardt. *Electrical Impedance Tomography: The realisation of regional ventilation monitoring*. https://www.draeger.com/Content/Documents/Content/rsp-eit-booklet-9066788-en.pdf. Accessed: 2024-07-07. Lubeck, Germany.

[14] O. R. Shishvan, A. Abdelwahab, N. B. da Rosa, G. J. Saulnier, J. L. Mueller, J. C. Newell, and D. Isaacson. ACT5 Electrical Impedance Tomography System. *IEEE Transactions on Biomedical Engineering*, 71(1):227–236, 2024.

[15] Sentec. *LuMon™ System – Adults / Children configuration (LMS-A)*. https://www.sentec.com/fileadmin/documents/_EIT_documents/LMS-A_Specification_Sheet_English.pdf. Accessed: 2024-07-07.

[16] Timpel. *ENLIGHT 2100 INDIVIDUALIZATION OF RESPIRATORY CARE BY CONTINUOUS REGIONAL MONITORING*. https://www.linet.com/-/media/Global/Images/Components/Brochures-and-Documents/New-Timpel-Brochure.pdf. Accessed: 2024-07-07.

[17] R. Cook, G. Saulnier, D. Gisser, J. Goble, J. Newell, and D. Isaacson. ACT3: a high-speed, high-precision electrical impedance tomograph. *IEEE Trans Biomed Eng*:41(8):713–22, 1994.

[18] J. Ashe, D. Shoudy, G. Boverman, J. Sabatini, T.-J. Kao, and B. Amm. A High Precision Parallel Current Drive Experimental EIT System. *15th International Conference on Biomedical Applications of Electrical Impedance Tomography*, 2014.

[19] D. C. Barber and B. H. Brown. Applied potential tomography. *J. Phys. E: Sci. Instrum*, 17(9):723, 2012.

[20] P. J. Vauhkonen. Image Reconstruction in Three-Dimensional Electrical Impedance Tomography. PhD thesis. Department of Applied Physics, University of Kuopio, Kuopio, Finland, 2004.

[21] M. Cheney, D. Isaacson, J. C. Newell, S. Simske, and J. Goble. NOSER: An Algorithm for Solving the Inverse Conductivity Problem. International journal of imaging systems and technology. *International journal of imaging systems and technology*:2(2), 66–75, 1990.

[22] A. Adler and R. Guardo. A neural network image reconstruction technique for electrical impedance tomography. *IEEE transactions on medical imaging*, 13(4):594–600, 1994.

[23] T. B. R. Santos, R. M. Nakanishi, T. M. M. Olegário, R. G. Lima, and J. L. Mueller. Resolution improvement and algorithmic dependence of machine learning for post-processing respiratory EIT images. *Applied Mathematics for Modern Challenges*, 1(1):21–38, 2023.

[24] J. Kaipio, V. Kolehmainen, E. Somersalo, and M. Vauhkonen. Statistical inversion and Monte Carlo sampling methods in electrical impedance tomography. *Inverse Problems*, 16(5):1487–1522, 2000. ISSN: 1361-6420.

[25] M. M. Dunlop and A. M. Stuart. The Bayesian formulation of EIT: Analysis and algorithms. *Inverse Problems and Imaging*, 10(4):1007–1036, 2016. ISSN: 1930-8337.

[26] T. de Castro Martins, A. K. Sato, F. S. de Moura, E. D. L. B. de Camargo, O. L. Silva, T. B. R. Santos, Z. Zhao, K. Möeller, M. B. P. Amato, J. L. Mueller, R. G. Lima, and M. de Sales Guerra Tsuzuki. A review of electrical impedance tomography in lung applications: Theory and algorithms for absolute images. *Annual Reviews in Control*, 48:442–471, 2019. ISSN: 1367-5788.

[27] J. L. Mueller and S. Siltanen. *Linear and Nonlinear Inverse Problems with Practical Applications*. Society for Industrial and Applied Mathematics, 2012.

[28] J. Mueller and S. Siltanen. The D-bar method for electrical impedance tomography-demystified. *Inverse Probl*:36(9):093001, 2020.

[29] J. C. Goble. The Three-Dimensional Inverse Problem In ELectric Current Computed Tomography. PhD thesis. Computer Science, Rensselaer Polytechnic Institute, Troy, NY, 1990.

[30] A. V. Pigatto, T. J. Kao, J. L. Mueller, C. D. Baker, E. M. DeBoer, and O. Kupfer. lectrical impedance tomography detects changes in ventilation after airway clearance in spinal muscular atrophy type I. *Respiratory physiology and neurobiology*:294:103773, 2021.

[31] N. Barbosa da Rosa Junior, A. V. Pigatto, T.-J. Kao, N. Stoffel, C. Bromirski, D. Davenport, P. Offner, E. Burnham, and J. L. Muelle. EIT-derived measures of pulmonary health from 3-D reconstructions in mechanically ventilated ARDS patients. *AIP Conf. Proc.*, 2947(1), 2023.

[32] O. R. Shishvan. ACT5 EIT SYSTEM: A Multiple-Source Electrical Impedance Tomography System. PhD thesis. Department of Electrical and Computer Engineering, University at Albany, Albany, NY, 2022.

[33] S. C. FitzSimmons. The changing epidemiology of cystic fibrosis. *The Journal of Pediatrics*:122(1):1–9, 1993.

[34] R. Kalikkot Thekkeveedu, M. C. Guaman, and B. Shivanna. Bronchopulmonary dysplasia: A review of pathogenesis and pathophysiology. *Respiratory medicine*:132, 170–177, 2017.

[35] L. A. Latson and L. R. Prieto. Congenital and Acquired Pulmonary Vein Stenosis. *Circulation*, 115(1):103–108, 2007.

[36] M. A. Matthay, Y. Arabi, A. C. Arroliga, G. Bernard, A. D. Bersten, L. J. Brochard, C. S. Calfee, A. Combes, B. M. Daniel, N. D. Ferguson, M. N. Gong, J. E. Gotts, M. S. Herridge, J. G. Laffey, K. D. Liu, F. R. Machado, T. R. Martin, D. F. McAuley, A. Mercat, M. Moss, R. A. Mularski, A. Pesenti, H. Qiu, N. Ramakrishnan, V. M. Ranieri, E. D. Riviello, E.

Rubin, A. S. Slutsky, B. T. Thompson, T. Twagirumugabe, L. B. Ware, and K. D. Wick. A New Global Definition of Acute Respiratory Distress Syndrome. *Am J Respir Crit Care Med*:209(1):37–47, 2024.

[37] M. A. Matthay, R. L. Zemans, G. A. Zimmerman, Y. M. Arabi, J. R. Beitler, A. Mercat, M. Herridge, A. G. Randolph, and C. S. Calfee. Acute respiratory distress syndrome. *Nat Rev Dis Primers*:5(1):18, 2019.

[38] K. W. Hendrickson, I. D. Peltan, and S. M. Brown. The Epidemiology of Acute Respiratory Distress Syndrome Before and After Coronavirus Disease 2019. *Crit Care Clin*:37(4):703–716, 2021.

[39] H. Banavasi, P. Nguyen, H. Osman, and A. O. Soubani. Management of ARDS – What Works and What Does Not. *Am J Med Sci*:362(1): 13–23, 2021.

[40] J.-M. Boles, J. Bion, A. Connors, M. Herridge, B. Marsh, C. Melot, R. Pearl, H. Silverman, M. Stanchina, A. Vieillard-Baron, and T. Welte. Weaning from mechanical ventilation. *European Respiratory Journal*:29(5):1033–1056, 2007.

[41] F. van Haren, T. Pham, L. Brochard, G. Bellani, J. Laffey, M. Dres, E. Fan, E. Goligher, L. Heunks, J. Lynch, H. Wrigge, and D. McAuley. Spontaneous Breathing in Early Acute Respiratory Distress Syndrome: Insights From the Large Observational Study to UNderstand the Global Impact of Severe Acute Respiratory FailurE Study*. *Critical Care Medicine*:47(2): 229–238, 2019.

[42] T. Yoshida, Y. Fujino, M. B. P. Amato, and B. P. Kavanagh. Spontaneous Breathing during Mechanical Ventilation. Risks, Mechanisms, and Management. *American Journal of Respiratory and Critical Care Medicine*:195(8):985–992, 2017.

[43] R. SC, H. GL, S. PD, S. SM, and D. TA. Early lung disease in infants and preschool children with cystic fibrosis. What have we learned and what should we do about it? *Am J Respir Crit Care Med*:195(12):1567–1575, 2017.

[44] P. D. Sly, C. L. Gangell, L. Chen, R. S. Ware, S. Ranganathan, L. S. Mott, C. P. Murray, and S. M. Stick. Risk factors for bronchiectasis in children with cystic fibrosis. *New England Journal of Medicine*:368(21):1963–1970, 2013.

[45] P. D. Sly and C. E. Wainwright. Preserving lung function: the holy grail in managing cystic fibrosis. *Annals of American Thoracic Society*:14(6):833–835, 2017.

[46] G. E. Stanford, K. Dave, and N. J. Simmonds. Pulmonary Exacerbations in Adults With Cystic Fibrosis: A Grown-up Issue in a Changing Cystic Fibrosis Landscape. *Chest*:159(1):93–102, 2021.

[47] Cystic Fibrosis Foundation. *2013 Annual Data Report to the Center Directors*. 2014.

[48] O. O'Connell, S. McWilliams, A. McGarrigle, O. O'Connor, F. Shanahan, D. Mullane, J. Eustace, M. Maher, and B. Plant. Radiologic imaging in cystic fibrosis: cumulative effective dose and changing trends over 2 decades. *Chest*:141(6):1575–83, 2012.

[49] D. Brenner and E. Hall. Computed tomography - an increasing source of radiation exposure. *N Engl J Med*:357:2277–84, 2007.

[50] M. Johannesson, J. Askling, S. Montgomery, A. Ekbom, and S. Bahmanyar. Cancer risk among patients with cystic fibrosis and their first-degree relatives. *Int. J. Cancer*, 125(12):2953–2956, 2009.

[51] L. F. Donnelly, J. R. MacFall, H. P. McAdams, J. M. Majure, J. Smith, D. P. Frush, P. Bogonad, H. C. Charles, and C. E. Ravin. Cystic fibrosis: Combined hyperpolarized 3he-enhanced and conventional proton mr imaging in the lung-preliminary observations. *Radiology*:212(3):885–889, 1999.

[52] P. Koumellis, E. J. van Beek, N. Woodhouse, S. Fichele, A. J. Swift, M. N. Paley, C. Hill, C. J. Taylor, and J. M. Wild. Quantitative analysis of regional airways obstruction using dynamic hyperpolarized 3he MRI-preliminary results in children with cystic fibrosis. *Journal of Magnetic Resonance Imaging*:22(3):420–426, 2005.

[53] K. et al. Mentore. Hyperpolarized HHe 3 MRI of the lung in cystic fibrosis. *Academic Radiology*:12(11):1423–1429, 2005.

[54] P. M. Jakob, T. Wang, G. Schultz, H. Hebestreit, A. Hebestreit, and D. Hahn. Assessment of human pulmonary function using oxygen-enhanced t1 imaging in patients with cystic fibrosis. *Magnetic Resonance in Medicine*:51(5):1009–1016, 2004.

[55] M. Eichinger, M. Puderbach, C. Fink, J. Gahr, S. Ley, C. Plathow, S. Tuengerthal, I. Zuna, F.-M. Muller, and H.-U. Kauczor. Contrast-enhanced 3d mri of lung perfusion in children with cystic fibrosis - initial results. *European Radiology*:16(10):2147–2152, 2006.

[56] N. Kanhere, M. J. Couch, K. Kowalik, B. Zanette, J. H. Rayment, D. Manson, P. Subbarao, F. Ratjen, and G. Santyr. Correlation of lung clearance index with hyperpolarized 129xe magnetic resonance imaging in pediatric subjects with cystic fibrosis. *American Journal of Respiratory and Critical Care Medicine*:196(8):1073–1075, 2017.

[57] H. Marshall, A. Horsley, C. J. Taylor, L. Smith, D. Hughes, F. C. Horn, A. J. Swift, J. Parra-Robles, P. J. Hughes, G. Norquay, N. J. Stewart, G. J. Collier, D. Teare, S. Cunningham, I. Aldag, and J. M. Wild. Detection of early subclinical lung disease in children with cystic fibrosis by lung ventilation imaging with hyperpolarised gas MRI. *Thorax*:72(8):760–762, 2017.

[58] R. P. Thomen, L. L. Walkup, D. J. Roach, Z. I. Cleveland, J. P. Clancy, and J. C. Woods. Hyperpolarized 129xe for investigation of mild cystic fibrosis lung disease in pediatric patients. *Journal of Cystic Fibrosis*:16(2):275–282, 2017.

[59] S. K. Nagle, M. Puderbach, M. Eichinger, and T. A. Altes. *Magnetic Resonance Imaging of the Lung: Cystic Fibrosis*. Springer Berlin Heidelberg, Berlin, Heidelberg, 2017.

[60] E. L. V. Costa, J. B. Borges, A. Melo, F. Suarez-Sipmann, C. Toufen, S. H. Bohm, and M. B. P. Amato. Bedside estimation of recruitable alveolar collapse and hyper-distension by electrical impedance tomography. *Intensive Care Medicine*:35(6):1132–1137, 2009.

[61] B. Vogt, Z. Zhao, P. Zabel, N. Weiler, and I. Frerichs. Regional lung response to bronchodilator reversibility testing determined by electrical impedance tomography in chronic obstructive pulmonary disease. *American Journal of Physiology - Lung Cellular and Molecular Physiology*:311(1):L8–L19, 2016.

[62] E. O. Ohuma, A. B. Moller, E. Bradley, S. Chakwera, L. Hussain-Alkhateeb, A. Lewin, Y. B. Okwaraji, W. R. Mahanani, E. W. Johansson, T. Lavin, D. E. Fernandez, G. G. Domínguez, A. de Costa, J. A. Cresswell, J. Krasevec, J. E. Lawn, H. Blencowe, J. Requejo, and A. C. Moran. National, regional, and global estimates of preterm birth in 2020, with trends from 2010: a systematic analysis. *Lancet (London, England)*:402(10409), 1261–1271, 2023.

[63] J. Perin, A. Mulick, D. Yeung, F. Villavicencio, G. Lopez, K. L. Strong, D. Prieto-Merino, S. Cousens, R. E. Black, and L. Liu. Global, regional, and national causes of under-5 mortality in 2000-19: an updated systematic analysis with implications for the Sustainable Development Goals. *The Lancet. Child and adolescent health*:46(2), 106–115, 2022.

[64] L. Bonadies, P. Zaramella, A. Porzionato, G. Perilongo, M. Muraca, and E. Baraldi. Present and Future of Bronchopulmonary Dysplasia. *Journal of Clinical Medicine*, 9(5), 2020.

[65] E. G. Shepherd, B. J. Clouse, K. A. Hasenstab, S. Sitaram, D. T. Malleske, L. D. Nelin, and S. R. Jadcherla. Infant Pulmonary Function Testing and Phenotypes in Severe Bronchopulmonary Dysplasia. *Pediatrics*:141(5), 2018.

[66] L. D. Nelin, M. J. Kielt, M. Jebbia, S. Jadcherla, and E. G. Shepherd. Bronchodilator responsiveness and dysanapsis in bronchopulmonary dysplasia. *ERJ open research*:8(3), 2022.

[67] T. D. Homan and R. P. Nayak. Short- and Long-Term Complications of Bronchopulmonary Dysplasia. *Respiratory care*:66(10), 1618–1629, 2021.

[68] B. Thebaud, K. N. Goss, M. Laughon, J. A. Whitsett, S. H. Abman, R. H. Steinhorn, J. L. Aschner, P. G. Davis, S. A. McGrath-Morrow, R. F. Soll, and A. H. Jobe. Bronchopulmonary dysplasia. *Nat Rev Dis Primers*, 5:78, 2019.

[69] C. H. Backes, E. Nealon, A. K. Armstrong, C. L. Cua, C. Mitchell, U. Krishnan, R. D. Vanderlaan, M. K. Song, N. Viola, C. V. Smith, P. I. McConnell, B. K. Rivera, and J. Bridge. Pulmonary Vein Stenosis in Infants: A Systematic Review, Meta-Analysis, and Meta-Regression. *The Journal of Pediatrics*:198, 36–45, 2018.

[70] S. Vyas-Read, N. P. Varghese, D. Suthar, C. Backes, S. Lakshminrusimha, C. J. Petit, and P. T. Levy. Prematurity and Pulmonary Vein Stenosis: The Role of Parenchymal Lung Disease and Pulmonary Vascular Disease. *Children (Basel)*:12, 9(5):713, 2022.

[71] R. D. Vanderlaan, J. Rome, R. Hirsch, D. Ivy, and C. A. Caldarone. Pulmonary vein stenosis: Treatment and challenges. *The Journal of thoracic and cardiovascular surgery*:161(6), 2169–2176, 2021.

[72] P. Pazos-López, C. García-Rodríguez, A. Guitián-González, E. Paredes-Galán, M. Á. Álvarez-Moure, M. Rodríguez-Álvarez, J. A. Baz-Alonso, E. Teijeira-Fernández, F. Calvo-Iglesias, and A. Iñiguez-Romo. Pulmonary vein stenosis: Etiology, diagnosis and management. *World J Cardiol*:26, 8(1):81–8, 2016.

[73] D. G. Gisser, D. Isaacson, and J. C. Newell. Electric Current Computed Tomography and Eigenvalues. *SIAM Journal on Applied Mathematics*, 50(6):1623–1634, 1990.

[74] D. Isaacson. Distinguishability of conductivities by electric current computed tomography. *IEEE Trans Med Imaging*, 5(2):91–95, 1986.

[75] T.-J. Kao. A 3-D Reconstruction Algorithm for Electrical Impedance Tomography Using Planar Electrode Arrays. PhD thesis. Department of Biomedical Engineering, Rensselaer Polytechnic Institute, Troy, NY, 2005.

[76] E. Jakubikova. The NOSER Algorithm. PhD thesis. Department of Mathematics, Colorado State University, Fort Collins, CO, 2005.

[77] T.-J. Kao, B. Amm, D. Isaacson, J. Newell, G. Saulnier, and J. L. Mueller. A 3D Reconstruction Algorithm for Real-time Simultaneous Multi-Source EIT Imaging for Lung Function Monitoring. *bioRxiv*, 2020.

[78] A. Abdelwahab, N. B. da Rosa, C. Wilcox, O. R. Shishvan, D. Isaacson, J. C. Newell, J. L. Mueller, and G. J. Saulnier. Simultaneous Acquisition of EIT and ECG Signals with the ACT 5 System (Submitted). *IEEE Transactions on Biomedical Engineering*, 2024.

[79] S. Haykin. *Adaptive Filter Theory*. 5th. International Edition. Pearson Education Limited, 2014. ISBN: 9780273764083.

[80] J. Glover. Adaptive noise canceling applied to sinusoidal interferences. *IEEE Transactions on Acoustics, Speech, and Signal Processing*, 25(6):484–491, 1977.

[81] A. Singh. *Adaptive Noise Cancellation*. Netaji Subhas Institute of Technology, Delhi, India, 2001.

[82] T. M. Inc. *MATLAB Version: 9.9.0.1718557 (R2020b) Update 6*. Natick, Massachusetts, United States, 2020.

[83] G. J. Saulnier, A. Abdelwahab, and O. Rajabi Shishvan. DSP-based current source for electrical impedance tomography. *Physiological measurement*, 41(6):064002, 2020.

[84] K. Howard, C. Rocheleau, T. Overton, J. B. Nava, M. Faldet, K. Moen, S. Soller, T. Stephens, E. van de Lagemaat, N. Wijesinghe, K. W. Dolloff, N. B. da Rosa, and J. L. Mueller. A comparison of techniques to improve pulmonary EIT image resolution using a database of simulated EIT images. *Journal of Computational and Applied Mathematics*:116415, 2024. ISSN: 0377-0427.

[85] J. L. Mueller, P. Muller, M. Mellenthin, R. Murthy, M. Capps, M. Alsaker, R. Deterding, S. D. Sagel, and E. DeBoer. Estimating regions of air trapping from electrical impedance tomography data. *Physiol Meas*, 39(5):05NT01, 2018.

[86] K. S. Cheng, D. Isaacson, J. C. Newell, and D. G. Gisser. Electrode models for electric current computed tomography. *IEEE transactions on bio-medical engineering*, 36(9):918–924, 1989.

[87] R. K. Albert and R. D. Hubmayr. The Prone Position Eliminates Compression of the Lungs by the Heart. *American Journal of Respiratory and Critical Care Medicine*, 161(5), 2000.

[88] N. Barbosa da Rosa Junior, T.-J. Kao, J. Briton, P. Offner, E. Burnham, and J. L. Mueller. Three-dimensional electrical impedance imaging during spontaneous breathing trials in patients with acute hypoxic respiratory failure: A pilot study. *Critical care explorations*, 7(1):e1198, 2025.

[89] J. E. Zablah, C. Vargas-Acevedo, N. B. da Rosa Jr, O. R. Shishvan, G. Saulnier, D. Isaacson, G. J. Morgan, and J. L. Mueller. Feasibility of Electric Impedance Tomography in the Assessment of Lung Perfusion and Ventilation in Congenital Pulmonary Vein Stenosis (Accepted). *Pediatric Cardiology*, 2025.

[90] D. Armstrong, K. Grimwood, K. Carlin, R. Carzino, J. Gutiarrez, J. Hull, A. Olinsky, E. Phelan, C. Robertson, and P. Phelan. Lower airway inflammation in infants and young children with cystic fibrosis. *American Journal of Respiratory and Critical Care Medicine*:156(4):1197–1204, 1997.

[91] J. E. Hoppe and E. T. Zemanick. Lessons from the lower airway microbiome in early CF. *Thorax*:72(12):1063–1064, 2017.

[92] W. W. Fox, M. A. Bureau, L. A. Taussig, R. R. Martin, and P. H. Beaudry. Helium low-volume curves in the detection of early small airway disease. *Pediatrics*:54:293–299, 1974.

[93] A. Lamarre, B. Reilly, A. Bryan, and H. Levison. Early detection of pulmonary function abnormalities in cystic fibrosis. *Pediatrics*:50:291–298, 1972.

[94] P. Macklem and J. Mead. Resistance of central and peripheral airways measured by a retrograde catheter. *J. App Physiol*:50:291–298, 1972.

[95] M. Paiva and L. Engel. The anatomical basis for the sloping n2 plateau. *Respiration Physiology*:44(3):325–337, 1981.

[96] S. Verbank, D. Schuermans, A. VanAcmuylem, C. Melot, M. Noppen, W. Vincken, and M. Paiva. Conductive and acinar lung-zone contributions to ventilation inhomogeneity in copd. *American Journal of Respiratory and Critical Care Medicine*:157(5):1573–1577, 1998.

[97] M. Estenne, A. V. Muylem, C. Knoop, and M. Antoine. Detection of obliterative bronchiolitis after lung transplantation by indexes of ventilation distribution. *Am J Respir Crit Care Med*:162(3 Pt 1):1047–5, 2000.

[98] B. O'Callaghan, J. E. Zablah, J. P. Weinman, E. K. Englund, G. J. Morgan, D. D. Ivy, B. S. Frank, D. A. Mong, L. J. Malone, and L. P. Browne. Computed tomographic parenchymal lung findings in premature infants with pulmonary vein stenosis. *Pediatric radiology*:53(9), 1874–1884. 2023.

Appendix A

Computing the A matrix parameters for the ToDLeR algorithm

The $A_n^{k1,k2}$ definition is

$$\begin{aligned}A_n^{k1,k2} = &\sum_{n_F=1}^{N_F}\sum_{n_F=1^{`}}^{N_F}[FR_{11}FZ_{11}(F\Theta_{11}+F\Theta_{21})]+\\
&\sum_{n_F=1}^{N_F}\sum_{m^{`}_F=1}^{N_F}\sum_{n^{`}_F=0}^{N_F}[FR_{121}FZ_{12}F\Theta_{12}+FR_{122}FZ_{12}(F\Theta_{12}+F\Theta_{22})]+\\
&\sum_{n^{`}_F=1}^{N_F}\sum_{m_F=1}^{N_F}\sum_{n_F=0}^{N_F}[FR_{131}FZ_{13}F\Theta_{13}+FR_{132}FZ_{13}(F\Theta_{13}+F\Theta_{23})]+\\
&\sum_{m_F=1}^{N_F}\sum_{n_F=0}^{N_F}\sum_{m^{`}_F=1}^{N_F}\sum_{n^{`}_F=0}^{N_F}[FR_{14}FZ_{14}F\Theta_{14}+FR_{144}FZ_{14}F\Theta_{24}+FR_3FZ_3F\Theta_{14}] \qquad \text{(A.1)}\end{aligned}$$

where

$$\begin{aligned}FR_{11}(r_n,n_F,n^{`}_F) &= n_Fn^{`}_F\int_{r_i}^{r_{i+1}} r^{n_F+n^{`}_F-1}dr\\
FR_{121}(r_n,n_F,m^{`}_F,n^{`}_F) &= \frac{n_Fm^{`}_F\pi}{h}\int_{r_i}^{r_{i+1}} r^{n_F}B_{n^{`}_F+1}(\frac{m^{`}_F\pi r}{h})dr\\
FR_{122}(r_n,n_F,m^{`}_F,n^{`}_F) &= n_Fn^{`}_F\int_{r_i}^{r_{i+1}} r^{n_F-1}B_{n^{`}_F}(\frac{m^{`}_F\pi r}{h})dr\\
FR_{131} &= FR_{121}(r_n,n^{`}_F,m_F,n_F)\\
FR_{132} &= FR_{122}(r_n,n^{`}_F,m_F,n_F)\end{aligned}$$

$$
\begin{aligned}
FR_{14}(r_n, m_F, n_F, m_F^{`}, n_F^{`}) = {} & \frac{m m_F^{`}\pi^2}{h^2}\int_{r_n}^{r_{n+1}} rB_{n_F+1}(\frac{m_F\pi r}{h})B_{n_F^{`}+1}(\frac{m_F^{`}\pi r}{h})dr + \\
& \frac{m_F n_F^{`}\pi}{h}\int_{r_n}^{r_{n+1}} B_{n_F+1}(\frac{m_F\pi r}{h})B_{n_F^{`}+1}(\frac{m_F^{`}\pi r}{h})dr + \\
& \frac{m_F^{`} n_F\pi}{h}\int_{r_n}^{r_{n+1}} B_{n_F^{`}+1}(\frac{m_F^{`}\pi r}{h})B_{n_F+1}(\frac{m_F\pi r}{h})dr + \\
& n_F n_F^{`}\int_{r_n}^{r_{n+1}} \frac{1}{r}B_{n_F}(\frac{m_F\pi r}{h})B_{n_F^{`}}(\frac{m_F^{`}\pi r}{h})dr \\
FR_{144}(r_n, m_F, n_F, m_F^{`}, n_F^{`}) = {} & n_F n_F^{`}\int_{r_n}^{r_{n+1}} B_{n_F}(\frac{m_F\pi r}{h})B_{n_F^{`}}(\frac{m_F^{`}\pi r}{h})dr \\
FR_{144}(r_n, m_F, n_F, m_F^{`}, n_F^{`}) = {} & \frac{m_F m_F^{`}\pi^2}{h^2} = \int_{r_n}^{r_{n+1}} rB_{n_F}(\frac{m_F\pi r}{h})B_{n_F^{`}}(\frac{m_F^{`}\pi r}{h})dr
\end{aligned}
\tag{A.2}
$$

$$
\begin{aligned}
F\Theta_{11}(k1, k2, \theta_n, n_F, n_F^{`}) = {} & a_{n_F}^{k1}a_{n_F^{`}}^{k2}\Theta_1 + b_{n_F}^{k1}b_{n_F^{`}}^{k2}\Theta_2 + a_{n_F}^{k1}b_{n_F^{`}}^{k2}\Theta_3 + b_{n_F}^{k1}a_{n_F^{`}}^{k2}\Theta_4 \\
F\Theta_{12}(k1, k2, \theta_n, n_F, m_F^{`}, n_F^{`}) = {} & a_{n_F}^{k1}c_{n_F^{`},m_F^{`}}^{k2}\Theta_1 + b_{n_F}^{k1}d_{n_F^{`},m_F^{`}}^{k2}\Theta_2 + \\
& a_{n_F}^{k1}d_{n_F^{`},m_F^{`}}^{k2}\Theta_3 + b_{n_F}^{k1}c_{n_F^{`},m_F^{`}}^{k2}\Theta_4 \\
F\Theta_{13}(k1, k2, \theta_n, n_F^{`}, m_F, n_F) = {} & c_{n_F,m_F}^{k1}a_{n_F^{`}}^{k2}\Theta_1 + d_{n_F,m_F}^{k1}b_{n_F^{`}}^{k2}\Theta_2 + \\
& c_{n_F,m_F}^{k1}b_{n_F^{`}}^{k2}\Theta_3 + d_{n_F,m_F}^{k1}a_{n_F^{`}}^{k2}\Theta_4 \\
F\Theta_{14}(k1, k2, \theta_n, m_F, N_F, m_F^{`}, n_F^{`}) = {} & c_{n_F,m_F}^{k1}c_{n_F^{`},m_F^{`}}^{k2}\Theta_1 + d_{n_F,m_F}^{k1}d_{n_F^{`},m_F^{`}}^{k2}\Theta_2 + \\
& c_{n_F,m_F}^{k1}d_{n_F^{`},m_F^{`}}^{k2}\Theta_3 + d_{n_F,m_F}^{k1}c_{n_F^{`},m_F^{`}}^{k2}\Theta_4
\end{aligned}
$$

$$
\begin{aligned}
F\Theta_{21}(k1,k2,\theta_n,n_F,n^{`}_F) &= b^{k1}_{n_F} b^{k2}_{n^{`}_F}\Theta_1 + a^{k1}_{n_F} a^{k2}_{n^{`}_F}\Theta_2 - b^{k1}_{n_F} a^{k2}_{n^{`}_F}\Theta_3 - a^{k1}_{n_F} b^{k2}_{n^{`}_F}\Theta_4 \\
F\Theta_{22}(k1,k2,\theta_n,n_F,m^{`}_F,n^{`}_F) &= b^{k1}_{n_F} d^{k2}_{n^{`}_F,m^{`}_F}\Theta_1 + a^{k1}_{n_F} c^{k2}_{n^{`}_F,m^{`}_F}\Theta_2 - \\
& \quad b^{k1}_{n_F} c^{k2}_{n^{`}_F,m^{`}_F}\Theta_3 - a^{k1}_{n_F} d^{k2}_{n^{`}_F,m^{`}_F}\Theta_4 \\
F\Theta_{23}(k1,k2,\theta_n,n^{`}_F,m_F,n_F) &= d^{k1}_{n_F,m_F} b^{k2}_{n^{`}_F}\Theta_1 + c^{k1}_{n_F,m_F} a^{k2}_{n^{`}_F}\Theta_2 - \\
& \quad d^{k1}_{n_F,m_F} a^{k2}_{n^{`}_F}\Theta_3 - c^{k1}_{n_F,m_F} b^{k2}_{n^{`}_F}\Theta_4 \\
F\Theta_{24}(k1,k2,\theta_n,m_F,N_F,m^{`}_F,n^{`}_F) &= d^{k1}_{n_F,m_F} d^{k2}_{n^{`}_F,m^{`}_F}\Theta_1 + c^{k1}_{n_F,m_F} c^{k2}_{n^{`}_F,m^{`}_F}\Theta_2 - \\
& \quad d^{k1}_{n_F,m_F} c^{k2}_{n^{`}_F,m^{`}_F}\Theta_3 - c^{k1}_{n_F,m_F} d^{k2}_{n^{`}_F,m^{`}_F}\Theta_4
\end{aligned}
\tag{A.3}
$$

$$
\begin{aligned}
\Theta_1(\theta_n,n_F,n^{`}_F) &= \int_{\theta_n}^{\theta_{n+1}} \cos(n_F\theta)\cos(n^{`}_F\theta)d\theta \\
\Theta_2(\theta_n,n_F,n^{`}_F) &= \int_{\theta_n}^{\theta_{n+1}} \sin(n_F\theta)\sin(n^{`}_F\theta)d\theta \\
\Theta_3(\theta_n,n_F,n^{`}_F) &= \int_{\theta_n}^{\theta_{n+1}} \cos(n_F\theta)\sin(n^{`}_F\theta)d\theta \\
\Theta_4(\theta_n,n_F,n^{`}_F) &= \Theta_3(\theta_n,n^{`}_F,n_F)
\end{aligned}
\tag{A.4}
$$

$$
\begin{aligned}
FZ_{11}(Z_n) &= z_{n+1} - z_n \\
FZ_{12}(Z_n,n_F,m^{`}_F,n^{`}_F) &= \frac{h}{m^{`}_F\pi}[\sin(\frac{m^{`}_F\pi z_{n+1}}{h}) - \sin(\frac{m^{`}_F\pi z_n}{h})] \\
FZ_{13}(Z_n,n^{`}_F,m_F,n_F) &= \frac{h}{m_F\pi}[\sin(\frac{m_F\pi z_{n+1}}{h}) - \sin(\frac{m_F\pi z_n}{h})] \\
FZ_{14}(Z_n,m_F,n_F,m^{`}_F,n^{`}_F) &= \int_{z_n}^{z_{n+1}} \cos(\frac{m_F\pi z}{h})\cos(\frac{m^{`}_F\pi z}{h})dz \\
FZ_3(Z_n,m_F,n_F,m^{`}_F,n^{`}_F) &= \int_{z_n}^{z_{n+1}} \sin(\frac{m_F\pi z}{h})\sin(\frac{m^{`}_F\pi z}{h})dz
\end{aligned}
\tag{A.5}
$$